ADDIS ABABA UNIVERSITY

COLLAGE OF NATURAL AND COMPUTATIONAL SCIENCES

SCHOOL OF EARTH SCIENCE

DETECTION OF GEOTHERMAL ANOMALIES AND EVALUATING LAND SURFACE TEMPERATURE IN NORTHERN ABAYA GEOTHERMAL FIELD, MAIN ETHIOPIAN RIFT

By
Tsion Taye

(GSR/2889/11)

Addis Ababa University

September, 2020

ADDIS ABABA UNIVERSITY

COLLAGE OF NATURAL AND COMPUTATIONAL SCIENCES

SCHOOL OF EARTH SCIENCE

DETECTION OF GEOTHERMAL ANOMALIES AND EVALUATING LAND SURFACE TEMPERATURE IN NORTHERN ABAYA GEOTHERMAL FIELD, MAIN ETHIOPIAN RIFT

A Thesis Submitted to

the School of Graduate Studies of Addis Ababa University, in Partial Fulfillment of the Requirements for the Degree of Master of Science in Remote Sensing and Geo-informatics.

By
Tsion Taye
(GSR/2889/11)

Advisor
Binyam Tesfaw (PhD)
Co-Advisor
Ameha Muluneh (PhD)

Addis Ababa University

September, 2020

Addis Ababa University

School of Graduate Studies

This is to certify that this thesis prepared by **Tsion Taye Weldeyohannes** entitled: "**DETECTION OF GEOTHERMAL ANOMALIES AND EVALUATING LAND SURFACE TEMPERATURE IN NORTHERN ABAYA GEOTHERMAL FIELD, MAIN ETHIOPIA RIFT** " and submitted in partial fulfillment of the requirements for the Degree of Master of Science (Remote Sensing and Geo-informatics) compiles with the regulations of the University and meets the accepted standards with respect to originality and quality.

Approved by board of examiners:

Dr. Bayissa Regassa	_____	_____
Chairman	Signature	Date
Dr. Binyam Tesfaw	_____	October 02, 2020
Advisor	Signature	Date
Dr. Ameha Atnafu	_____	_____
Co-advisor	Signature	Date
Dr. Dagnachew Legesse	_____	_____
Examiner	Signature	Date
Prof. Gezahegn Yirgu	_____	_____
Examiner	Signature	Date

Declaration

I, the undersigned, declare that this thesis entitled "DETECTION OF GEOTHERMAL ANOMALIES AND EVALUATING LAND SURFACE TEMPERATURE IN NORTHERN ABAYA GEOTHERMAL FIELD, MAIN ETHIOPIAN RIFT" is my original work and has not been presented for a degree in any other university and that all sources of materials used for this thesis have been interestingly acknowledged.

Tsion Taye Weldeyohannes

Signature _____

Date _____

Addis Ababa University

Addis Ababa

September, 2020.

Table of Contents

Table of Figures

Page

List of Tables

List of Acronyms

ASTER Advanced Thermal Emission and Reflection Radiometer

BT Brightness Temperature

CSA Central Statistics Agency

DEM Digital Elevation Model

EARS East African Rift System

ETM+ Enhanced Thematic Mapper

GIS Geographical Information System

GSE Geological Survey of Ethiopia

LSE Land Surface Emissivity

LST Land Surface Temperature

MER Main Ethiopian Rift

MODIS Moderate Resolution Imaging Spectro radiometer

NDVI Normalized Difference Vegetation Index

NMA National Meteorological Agency

NOAA National Oceanic and Atmospheric Administration

OLI Operational Land Imager

PV Proportion of vegetation

RMSE Root Mean Square Error

RS Remote Sensing

SC Single Channel

SRTM Shuttle Radar Topographic Mission

SW Split Window

TIR Thermal Infrared

TM Thematic Mapper

TOA Top of the Atmospheric

USGS United State Geological Survey

WFB Wonji Fault Belt

Acknowledgement

First and foremost, my deepest gratitude goes to the Almighty God for helping me throughout the thesis.

I would like to express my appreciation to my thesis advisors Dr. Binyam Tesfaw and Dr. Ameha Atenafu for giving me the opportunity to do this research, for their valuable feedback and for going above and beyond to make this possible. I could not have accomplished the completion of this thesis without their tireless support. It was a great honor to work and study under their extraordinary guidance.

I am extremely grateful to Addis Ababa University for offering me the scholarship opportunity. I would like to extend my heartfelt gratitude to the School of Earth Science instructors for sharing their immense knowledge. I would like to thank the National Meteorological Agency, Ethiopian Geological Survey and Central Statistical Agency for providing me with the essential data to do the research.

I cannot express enough thanks to my parents for their countless sacrifices. I would also like to thank my family and friends for their prayers, constant support, patience and encouragement. I appreciate everything you did for me. My special thanks go to my mother for the sleepless nights before deadlines, to Bereket Tesfaye for his generosity, to Eyob Mengesha, Yared Mola and to Simon Assegid. Finally, I want to acknowledge and thank everyone who has helped me to complete the thesis work directly or indirectly.

Abstract

Land Surface Temperature (LST), which is a radiative skin temperature of a given area, depends on several factors and physical parameters indicating that a onetime satellite image analysis will not be enough to identify areas with geothermal potential. Given the difficulty associated with surface temperature over wider areas, its characterization, distribution and temporal evolution, therefore, necessitates measurements with thorough spatial and temporal samplings. In the present thesis, a multi temporal Thermal infrared (TIR) remote sensing data (2000-2019 in two years interval) from the Advanced Space-borne Thermal Emission and Reflection Radiometer (ASTER) and Landsat has been used to detect geothermal areas and evaluate the LST of the northern Lake Abaya geothermal prospect of the southern Main Ethiopian Rift (MER). The study uses the single channel algorithm to derive LSTs and compare the result with borehole data from different literatures.

The result shows that the mean LST is highest in 2003 (320.1 K) and lowest in 2019 (303.1 K). The change in mean LST was between –9 K to 13 K. This LST results from ASTER images were validated with ASTER LST products and show more than 70% correlations. The derived LSTs from the nine images were compared with the borehole data. LSTs of the year 2003 have been much closer to the actual temperature value from borehole data. The geothermal anomaly areas were validated with the existed field data (19 sites). Fifteen sites fall in the identified geothermal anomaly areas, which is 79 % of the total. The result of correlation between time and LST values in known geothermal activity sites shows no correlation (less than 0.5) except one site, which is Boramitta (0.54). This shows that the LST is time invariant which goes well with the fact that there shouldn't be any significant change of LST in geothermal anomalous areas.

Key Words: Land Surface Temperature (LST), Geothermal Anomaly, Main Ethiopian Rift (MER), Thermal Infrared (TIR).

1. Chapter One

Introduction

1.1. Background

Geothermal energy is the energy of the 'Earths Heat', an essential backbone for the world's sustainable energy sources and important component of green energy in the globe. Its development has been increasingly important to diminish the greenhouse emission. (Aliyu et al., 2017, Chan et al., 2018, Muhammed R, 2019).The exhaustibility of fossil fuels, their unreliability and environmental implications has resulted in the search for alternative sources of energy. Over the last century the burning of fossil fuels like coal and oil has increased the concentration of atmospheric carbon dioxide (CO_2). To minimize the effect, various nations have been developing renewable energy source with low carbon emissions. The alternative energy resources are clean, environmental friendly and include geothermal, hydroelectric, wind and solar energy as well (Yosef Mengistu et al., 2019).

Geothermal Energy occurs in regions of anomalously high crustal heat flow that may be related to the presence of young igneous bodies or hot rocks located deeper in the crust (Ronald, 2005). This elevated geothermal heat is normally transferred to the surface by the convection of ground waters that forms hydrothermal systems: surface waters circulate to depth where they are heated and rise to the surface via a subterranean 'plumbing system' of closely spaced fractures or other zones of permeable rock. If rising hot waters reach the surface then characteristic geothermal features such as hot springs, fumaroles, geysers, and mud pools may form (Heasler et al., 2009). The geologic and tectonic setting of an area preferred by an adequate subsurface fluid flow determines the productivity of a geothermal field (Moeck, 2014).

The East African Rift System (EARS) is one of the few volcano-tectonically active regions in the world where heat energy from the Earth's interior escapes to the surface in the form of volcanic

eruptions and geothermal surface manifestations. The existence of shallow heat sources, intense faulting and abundant circulation of water with high geothermal gradient signify the presence of high-temperature geothermal systems in the rift valley. (Abiye, 2003; Teklemariam, M., 2008; Omenda, P., and Teklemariam,M. 2010; Pürschel,M., 2013).

Ethiopia has started a long-term geothermal exploration since 1970.Over the years a good inventory of areas with geothermal potential has been built up and a number of more important sites have been explored in the Ethiopian Rift (Figure 1). Currently, there are about 22 geothermal prospects and only 7.2 MW energy is generating from the Aluto - Langano geothermal power plant (Omenda and Teklemariam, M., 2010; JICA, 2015; Solomon Kebede, 2015).Other geothermal prospect areas are at various stages of exploration that vary from reconnaissance to detailed geo-scientific studies including drilling of temperature gradient (TG) wells. (Solomon Kebede, 2015). These include:

i. Tulu-Moye and Corbetti (Detailed geo-scientific including drilling of TG wells)
ii. Abaya, Dofan and Fantale (Detailed geo-scientific studies)
iii. Teo, Danab, Kone and others (Reconnaissance investigations)

Even though, there is a large geothermal potential along the rift, a detailed survey was conducted only on Aluto-Langano, Corbetti and Tendaho-Dubti geothermal sites. In other areas, investigations are mainly on the initial stages. One of those areas is the Abaya geothermal site. The northern Lake Abaya area is located in the southern part of Main Ethiopian Rift (MER) 500km away from the capital Addis Ababa. The main hydrothermal manifestations in the region are hot springs; fumaroles, bubbling and boiling pools. A study conducted by JICA (2015) classified 22 geothermal sites into the five priority groups, i.e. Priority-S, A, B, C and D on the basis of the multi-criteria analysis conducted. The Abaya prospect is in priority B, which has a potential of producing 2800 MW of electricity.

Investigating geothermal anomalies usually require a very large amount of resources if one uses geophysical methods and ground surveys. However, integrating these methods with remote sensing and geospatial data analysis is currently giving a robust result since, information about

the general geologic structures, locations of thermal anomalies and their manifestations can be yielded using remote sensing (Van der Meer et al., 2014).

Thermal Infrared (TIR) remote sensing has been used in geothermal exploration to identify hot springs and near-surface geothermal anomalies with TIR scanning techniques (Qin et al., 2011; Claudia and Stefan, 2013; Heasler and Jaworowski, 2018). LST which is a radiative skin temperature of the land surface can be derived from satellite information or direct measurements (Dar et al., 2019).It is an important parameter in land surface processes that helps to understand the energy exchange balance between the Earth and the atmosphere on a regional as well as global scale (Karnieli et al., 2010; Feizizadeh et al., 2013; Wu et al., 2013, 2015).

Albedo, slope, soil compaction, rock coherence, amount of solar insolation reaching the surface and time are among the physical parameters affecting LST analysis using satellite imageries (Calvin et al., 2005; Dar et al., 2019). The impact of time on the analysis can relate to the type of images used, whether they are a night or day time images. LST values of an area estimated by a day time image definitely varies from values estimated using a night one that is because images taken on the day time are subjected to a high probability of being biased by solar radiation (Coolbaugh et al., 2007). Night time images have an ability to identify and map localized hot springs and fumaroles for investigating geothermal anomalies. (Hesow R., 2019).Varying LST values of an area over time might also occur. Areas with high level of urbanization might have larger LST values and mislead the analyst to consider them as geothermal areas. (Yosef Mengistu et al., 2019).

Given the difficulty associated with surface temperature over wider areas its characterization, distribution and its temporal evolution, therefore, necessitates measurements with thorough spatial and temporal sampling. Remote sensing has drastically enhanced our capability for resource exploration and mapping, and monitoring of the earth's environment on local as well as global scales. (Van der Meer et al., 2014; Dar I. et al., 2019)

1.2. Geothermal System

According to Hochstein (1990), a geothermal system can be described schematically as 'convecting water in the upper crust of the Earth, which, in a confined space, transfers heat from a heat source to a heat sink, usually the free surface'. A geothermal system is made up of four main elements: **A heat source**, **a reservoir, a fluid and geological structures**,

- **The heat source**: - this can be a very high temperature (> 600 °C) magmatic intrusion that has reached relatively shallow depths (5-10 km), decaying radioactive elements or heat from overburdened pressures. In most cases high temperature geothermal areas show a close connection with eruptive centers that have produced silicic lava (Hochisten, 1990; Moeck, 2014).
- **The reservoir**: -It refers to a volume of hot permeable rocks from which the circulating fluids extract heat. The reservoir is generally overlain by a cover of impermeable rocks and connected to a surficial recharge area through which the meteoric waters can replace or partly replace the fluids that escape from the reservoir through springs or are extracted by boreholes. (Hochisten, 1990) It may be produced by self-sealing due to deposition of minerals from the solution mainly silica or by hydrothermal alteration of rocks to clays and/or zeolites.
- **The geothermal fluid**: -It is water, in the majority of cases meteoric water, in the liquid or vapor phase, depending on its temperature and pressure (Dickson and Fanelli, 2004). It is the carrier that transfers the heat. The amount of water in a geothermal system relies on the amount of recharge, structure and geology of the surroundings.
- **Geological Structures: -** refers to the geological faults and fractures related to geothermal systems. They serve as a path way for the geothermal fluids to come close to the surface. Structures are a principal indicator of geothermal potential because they create a secondary permeability for the circulation of geothermal fluids.

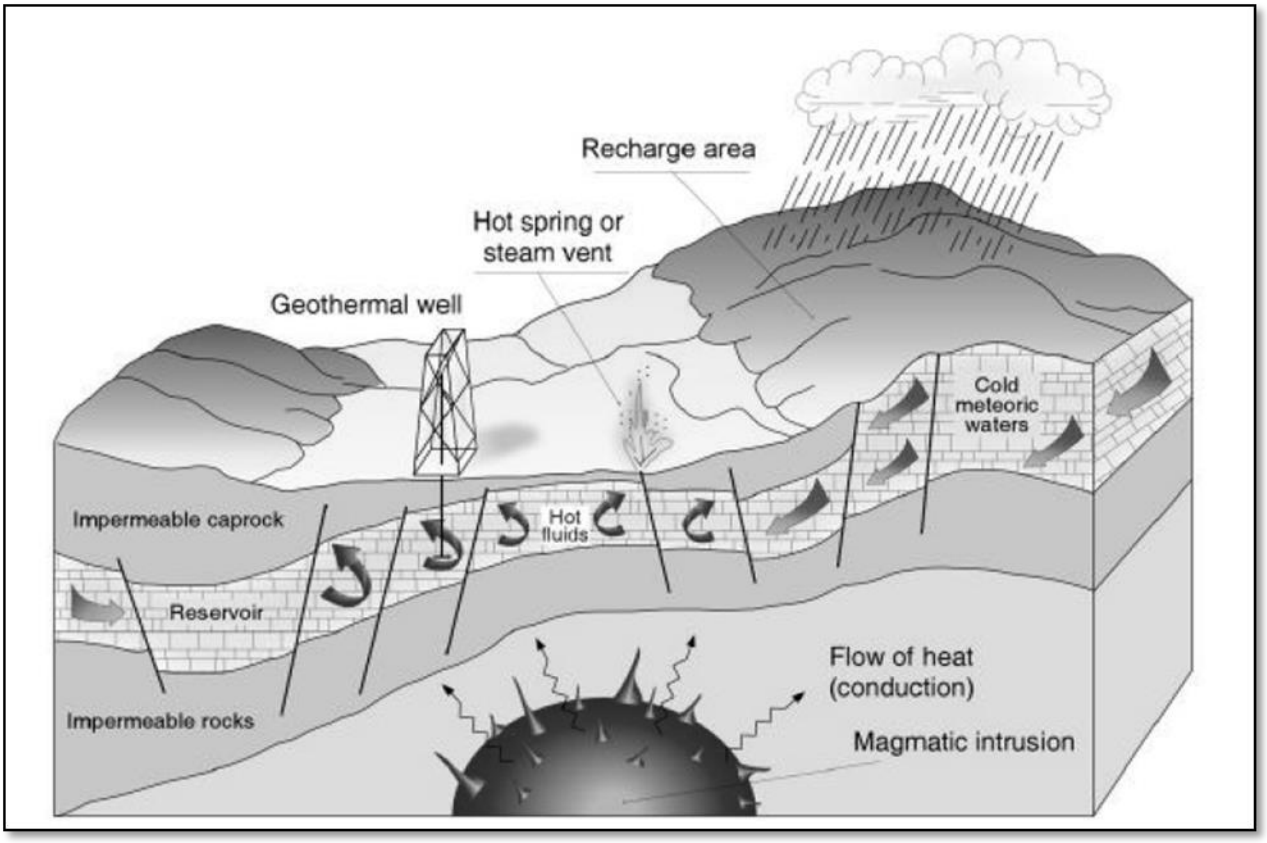

Figure 1 1 *Schematic representation of an ideal geothermal system. (From Dickson and Fanelli, 2004)*

Based on remote sensing analysis and site survey interpretation, JICA project team (2015) classified the geothermal reservoir and target sites of Ethiopia in to three. These are:-

- **Volcano type** is assumed to have a geothermal reservoir with a maximum plane area equivalent to the area coverage of young volcanic body identified in Dallol, Boina, Damali, Meteka (Ayelu and Amoissa), Dofan, Tulu Moye, Aluto (Langano, Finkilo, Bobesa), Abaya , Fantale and Boset geothermal areas.
- **Caldera type** is assumed to have a geothermal reservoir equivalent to the inner area of caldera embracing Gedemsa, Kone, Nazareth, and Corbetti areas;
- **Graben type** has a geothermal reservoir equivalent to the area of geothermal manifestations in graben structure including area in Tendaho (i.e, Allalobeda, Ayrobeda,

Dubti), Teo, Danab, Meteka, Arabi and Butajira geothermal areas. Characteristics of existing detailed information of Aluto-Langano, Tendaho Dubti and Corbetti areas were used as reference for the classification.

1.3. Statement of Problem

Unlike the three major geothermal prospect areas in the Main Ethiopian Rift (MER) (Pürschel et al., 2013), the Abaya geothermal prospect is not well studied though it was a recommended site as one of the geothermal fields in Ethiopia by the UNDP (1973).

There exist several methods for detecting geothermal anomalies and most require a very large amount of resources (time, budget and expertise) if one uses geophysical methods and ground surveys. However, remote sensing and geospatial method give a robust and quick result about the general geologic structures, location of thermal anomalies and their manifestations. (Van der Meer et al., 2014).

LST anomaly is a key indicator of geothermal areas in TIR remotely sensed imagery. However, it can be affected by many other factors besides geothermal resources, such as solar radiation, landforms and earthquakes (Qin et al., 2011). Therefore, geothermal detection using TIR remote sensing is a challenging yet interesting topic, and the mechanism of geothermal anomaly deserves further exploration to improve the accuracy of geothermal detection. Although a one-time satellite image analysis can be used to identify promising geothermal sites like Qin et al., 2011(Tengchong ,China), Yosef Darge et al., 2019 (Tulu Moye, Ethiopia) and Wang et al., 2019 (Dandong, China), a multi-temporal image analysis could give a better result on geothermal anomaly detection.

Since LST of a given area depends on several parameters such as the infrared wavelength used, spectral dependence of the emissivity, angle at which the measurement is made, state of the surface, height of the sensor above and the like (Calvin et al., 2005; Dar et al., 2019), a multi temporal satellite image analysis will help in the elimination of false anomalies and could give a

better result for detecting anomalous areas with geothermal potential. This means if an analyst identifies one place as a geothermal anomaly area in a year x, that place should be anomalous consistently throughout the given time frame to be verified as geothermal area, otherwise the estimated anomaly might be a false one resulting from other factors.

Moreover a multi temporal analysis will also give a privilege to map and monitor changes (if any) observed on the surface heat manifestations (Braddock M. et al., 2017; Dar I. et al., 2019). In the present study, a multi-temporal satellite image analysis from the year 2000 onwards(in two years interval except for some cases) has been conducted on Lake Abaya geothermal prospect of SNNP region, Ethiopia using multi-sensor thermal remote sensing data to detect anomalous areas and evaluate land surface temperature of the area over the years.

1.4. Objective of the study

1.4.1 General Objective

The main objective of this research is to conduct a multi temporal satellite image and geospatial data analysis to investigate geothermal anomalies and evaluate Land Surface Temperature (LST) of the Lake Abaya geothermal prospect.

1.4.2 Specific Objective

The following are the specific objectives

- To retrieve Land Surface Temperature from ASTER and Landsat images and validate the LST.
- Detection of geothermal anomalies.
- To evaluate LST of the study area for the last 20 years and compare it with temperatures from previous studies.

1.4.3 Research Question

- What is the role of satellite imageries in detection of geothermal anomalies?
- Does LST value of an area vary depending on the time factor?

1.5. Significance of the Study

The outcome generated from this research is believed to provide detail information on how to use a cost effective and reliable tool to explore large areas of geothermal potential for the scientific community, concerned governmental body and other individuals interested on geothermal resources.

1.6. Scope of the Study

The scope of the study is to detect geothermal Land surface temperature anomaly using different datasets and comparing it with previous geological and land surface temperature data in the Northern Lake Abaya.

2. Chapter Two

Literature Review

This chapter presents literature reviews related to application of remote sensing in geothermal exploration, estimation of LST and its components. European Space Agency (ESA) defines LST as the radiative skin temperature of the land derived from solar radiation. It can simply be referred as how hot the "surface" of the Earth would feel to the touch in a particular location. From a satellite view "surface" refers to whatever it sees when it looks through the atmosphere to the ground. The quantification of the Earth's surface temperature helps in different environmental studies. This includes study of global warming, deduction of the health status of agricultural crop, evaluation of severity of forest fires, state of dryness of forest, estimating evapo-transpiration of vegetated areas and assessing potential of geothermal areas(the like. (Julien, Y. et al.,2006; Marcos, E. et al.,2018; Maffei, C et al.,2018; Mia, M.B. et al.,2018; Yosef Mengistu et al.,2019 cited in Aparicho et al., 2020)

2.1 Remote Sensing for Geothermal Exploration

2.1.1 Previous Studies

Remote sensing has been recognized as a viable tool for geothermal exploration. It has primary advantages in minimizing the cost and effort of ground-based surveys. It can give valuable information such as surface temperature anomalies and structural control of the earth surfaces that could lead to the findings of geothermal surface expressions and ultimately to locate new geothermal prospect areas.

Several studies have been carried out for geothermal exploration using satellite imageries. The first application can be dated back to the middle of 20th century. In 1961, the US Army Cold Regions Research and Engineering Laboratory together with the University of Michigan conducted a geothermal survey on Yellowstone National Park in the USA with thermal infrared

scanning technique and successfully detected the sign of hot springs and other near-surface geothermal anomalies (Zhou, 1998 cited in Qin et al., 2011). Subsequently, Lee (1978) discovered the geothermal anomalies in Lordsburg District of New Mexico, USA with TIR remote sensing.

In the late 80s of 20th century, the thermal infrared bands of the National Oceanic and Atmospheric Administration (NOAA) satellite were used in geothermal surveys in the eastern part of the Fujian Province in China. The researchers reported that the distributions of medium and low temperature areas in eastern Fujian were related to the regional deep faults caused by the intense geothermal activities in Mesozoic and Cenozoic eras (Ge, 1999 cited in Qin et al., 2011). Prakash et al. (1995) proposed that thermal infrared data of different times could be used to estimate the depth of buried thermal source for the same anomaly area. Hellman and Ramsey (2004) investigated the geothermal hot springs of Yellowstone National Park using the thermal infrared data of the Advanced Thermal Emission and Reflection Radiometer (ASTER) and Airborne Visible/Infrared Imaging Spectrometer (AVIRIS). Vaughan et al. (2005) and Coolbaugh et al. (2007) studied the geothermal hot springs in Nevada of the United States with TIR remote sensing. Fred et al. (2008) provided a first quantitative representation of the surficial geothermal activities in Yellowstone National Park using the ETM+ thermal infrared data.

In recent years, Hecker et al. (2017) examined the use of multi-source satellite remote sensing such as Advanced Space-borne Thermal Emission and Reflection Radiometer (ASTER) and Shuttle Radar Topography Mission (SRTM) for targeting the geothermal anomaly in Flores Island. This research inferred that the low spatial resolution has been a prominent limitation of satellite imageries because most of the geothermal anomalies are relatively small as compared to the image pixel size.

On the other hand, a very high spatial resolution data could be acquired using UAV platform. For example, UAV has been used for monitoring geothermal heat flux and detecting temperature anomalies of a geothermal field in New Zealand (Harvey et al., 2016). Throughout these studies, UAV has the advantage to provide a very high spatial (less than 10 cm) and temporal resolution

images (possibly in order of the day). However, UAV platforms are still limited to small survey areas due to the limitation with power and maximum flight distance.

The intermediate platform like airborne remote sensing is the most appropriate tool for a large but detail geothermal prospection. The airborne-based images provide a sub-meter spatial resolution that is suitable for the detection of geothermal manifestations with small size (Haselwimmer and Prakash, 2013).

2.1.2. Measurable indicators by remote sensing

Temperature anomalies and geological structures at the surface are good indicators of geothermal potential in the subsurface. According to Van der Meer et al. (2014), these indicators could be retrieved through remote sensing instruments as indirect evidence to geothermal activity underneath the earth's surface. Besides, surface temperature anomalies and structures are essential as the analog of the geothermal reservoir condition and geothermal fluid pathways (Curewitz and Karson, 1997; Haselwimmer and Prakash, 2013). However, the link between the surface indicators to the subsurface features requires further geologic interpretation in particular coupling the remote sensing data with the subsurface geophysics (Van der Meer et al., 2014).

Geothermal temperature anomalies have been described as heat anomalies associated with the occurrence of geothermal manifestation such as fumaroles, geysers, and hot springs (Varghese, 2016). These anomalies are manifests of the elevated geothermal heat which transferred to the earth's surface through the convection of ground waters in the permeable rocks or structures. Moreover, there are also manifestations that occurred due to the conductive heat loss such as steaming grounds (Haselwimmer and Prakash, 2013). The temperature of geothermal fluids has a considerable range depending on the type of geothermal systems. (Stober and Bucher, 2013)

2.2. Mechanism of Geothermal Anomaly

LST is mainly generated from solar radiation which accounts for a throughout heating of land surface and the Earth's interior heat which is responsible for a localized temperature increase. The understanding of surface energy balance and underground heat transfer will contribute to the identification of geothermal areas caused by Earth's interior heat. At land surface, temperature is the result of balanced surface energy radiation (Zhang 1999 cited in Qin et al., 2011). In general, the surface energy balance can be simply expressed Monteith (1973).

$$Qd = H + \lambda E + G \qquad (1)$$

Where Q_d is the net radiation received by land surface; H denotes the sensible heat flux between the land surface and the lower atmosphere; λE stands for the latent heat flux in the phase transition of water between the underlying surface and the atmosphere; G is the soil heat flux characterizing the thermal exchanges among different depths of soil. For local area the sensible heat flux H and latent heat flux λE can be assumed unchanged, then soil heat flux (G) is a major factor affecting the balance of surface energy (Guo 2002 cited in Qin et al.,2011) . In the lithosphere, the heat is mainly transferred in thermal conduction (Rudnick et al., 1998). This process can be described by the following equation:

$$\nabla(K\nabla T) = -A \qquad (2)$$

Where T stands for temperature, K denotes the rock thermal conductivity, and A is the radiogenic heat production of rocks. For local area, heat flow is dominated by rock thermal conductivity K, which is mainly affected by rock's physical and chemical properties Li (1992) such as the mineral components, the rock porosity and the fracture filler. Thermal Convection is another important form of underground heat transfer. It exists in the upwelling of underground thermal materials, such as hot water, heated gases, even the up-surging magma along the rock cracks.

In conclusion, the inner heat is transferred to land surface through thermal conduction and convection, during which process the changes of soil heat flux break the balance of surface

energy and cause geothermal anomalies. Therefore, underground heat source and available thermal channels are two critical factors to determine geothermal areas.

2.3. Land Surface Temperature (LST) Estimation Algorithms.

Several algorithms have been developed to enable the extraction of LST from Visible, Near Infrared (VNIR) and TIR imagery acquired from different sensors (Jimenez et al., 2006). The difference between them lays on the amount and type of data used by the algorithms, especially on whether the algorithm includes the computation of the surface emissivity parameter or if it is introduced as a measured parameter. In order to calculate LST, land surface emissivity (LSE) can be known or unknown.

If the LSE is known, the existing methods differ on the number of thermal infrared bands used and can be subdivided in to: The single Channel (SC) method which is based on a single thermal channel, the split window algorithm (SWA) that uses more than two thermal channels, and the multi- angle method that requires imagery acquired at different viewing angles

2.4 Materials and Method

2.4.1. Description of study area

Location and accessibility

The study area extends from latitude 6°35′45″N to 6°58′27″ N and 37°50′51″ to 38°09′26″E longitude in the southern part of the Main Ethiopian Rift (MER) and northern Lake Abaya area. It is within the Southern Nations and Nationalities Region (SNNPR) and about 500 km south of Addis Ababa (Figure 2.1). It is accessible by the Asphalt-weather Addis Ababa – Arba Minch road. Secondary road such as the Humbo – Abela Fericho – Bilate farms road provide reasonable access within the study area with many other secondary roads in the intensely cultivated parts along the escarpments. It has a total area of 1435km^2 and a part of the Abaya geothermal prospect, which is the southernmost known high temperature prospect area. It is located on the

north side of Lake Abaya, adjacent to the western escarpment of the Wenji Fault Belt (WFB). (Tadiwos Chernet, 2011)

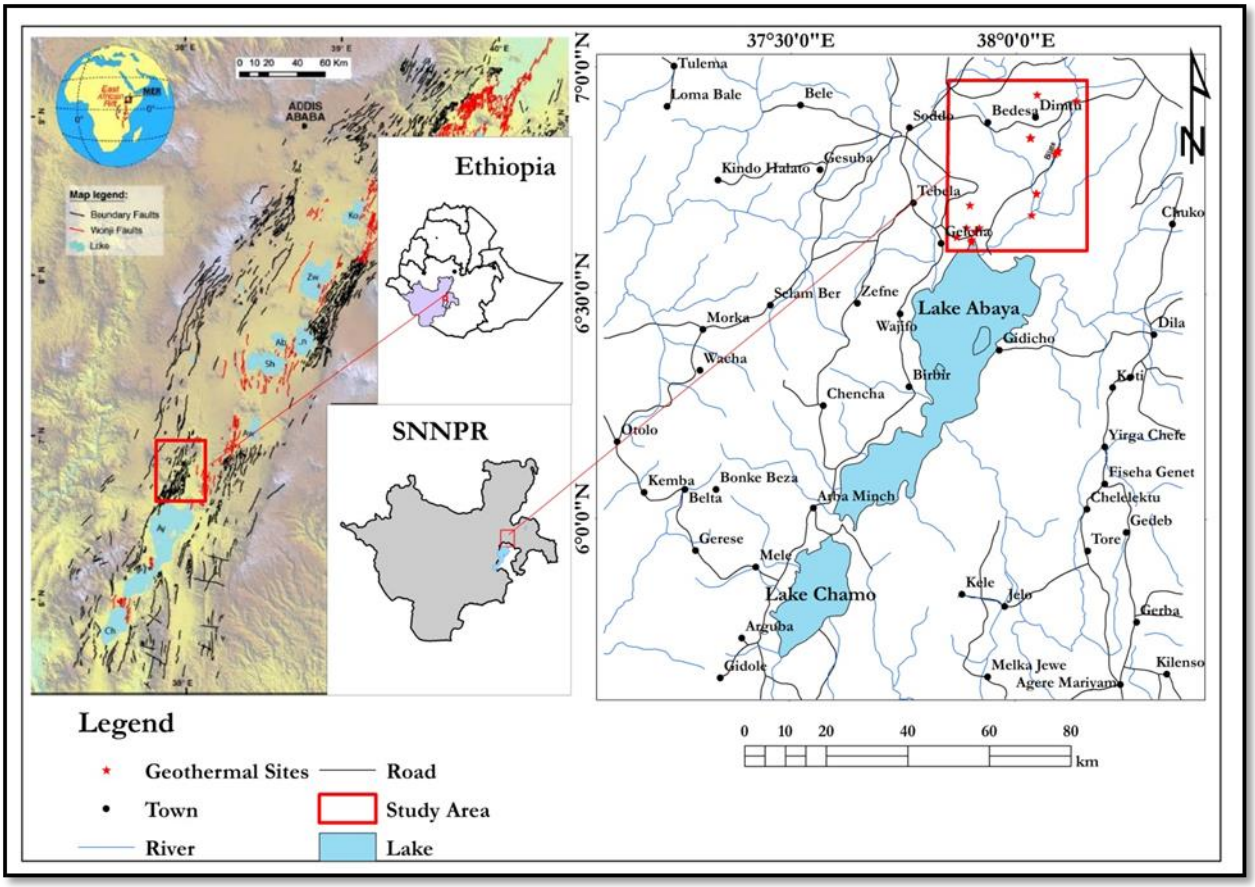

Figure 2. 1*Location Map of the study area.*

2.4.2. Physiography

The western part of the study area makes the escarpment of the southern part of the MER. It has a series of normal faults and slopes down from an average elevation of between 2251 and1161 m a.s.l. The Pliocene Damota trachytic volcano which rises to 2950 m a.s.l. and Saloko ridge west of Humbo town form major volcanic landforms on the rift escarpments. The rift floor comprises of flat volcano sedimentary plains at an average altitude of 1300 m a.s.l and is characterized by a series of sub-parallel normal faults with predominantly NNE-SSW trend forming horsts and graben structures within the rift. The plains are cut at places by steep sided river valleys. This belt of intense faulting and Quaternary volcanism represent the southern sector of the Wonji

Fault Belt (WFB) which is the active axis of extension in the MER. (Corti, 2009). Similar to other parts of the MER, this active belt of tectonism hosts several complex rhyolitic volcanic centers. The Duguna Fango rising over 1000m above the rift floor is the most prominent one with a base diameter of over 10 km and rises to an elevation of 2240 m a.s.l. Other smaller rhyolitic centers rising about 500m above the general rift floor level include Chericha, SalwaDore, Hako, Donga (Simbura), Obicha and Werencha (Meseret Teklemariam and Solomon Kebede, 2002).

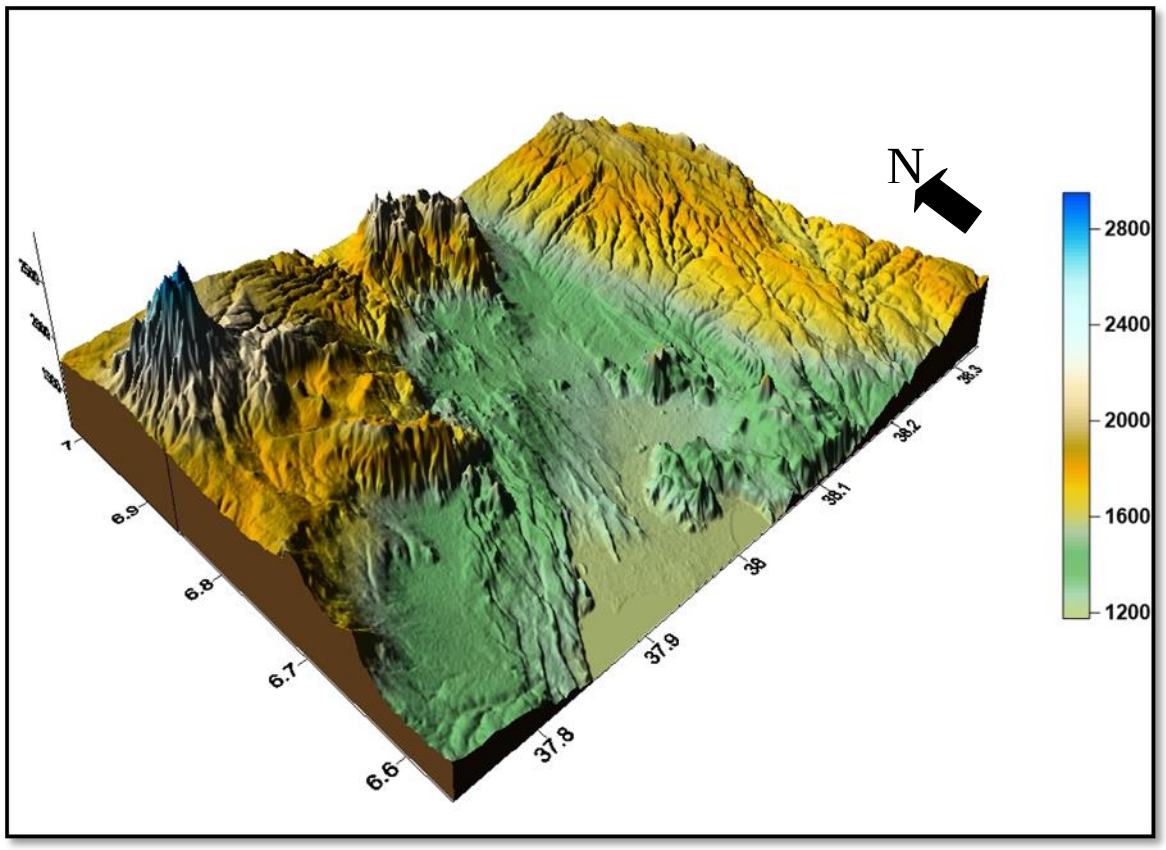

Figure 2. 2 ***Physiographic Map of the study area.***

2.4.3 Drainage Pattern

The study area is part of a closed drainage system within the southern MER with all rivers and streams draining into Lake Abaya (Figure 2.1). The Hamesa River and its tributaries drain the western part whereas the central and northern part of the study area is drained by Bilate River and its tributaries such as Bisare and Derba which form a delta at its confluence into the northern

shore of Lake Abaya. The other important river draining the Eastern escarpment and Southeastern part of the study area is Gidabo.

2.4.4. Climate and vegetation

Part of the study area, being on the western escarpment, belongs to the *Weyna Dega* agro ecological zone whereas the study area in the rift floor belongs to the *Kola* zone. A warm and humid climate is typical of the *Weyna Dega* zone, having a mean annual temperature ranging between 17°C and 20°C and with annual precipitation as high as 1500 mm. The *Kola* zone has a mean annual temperature between 20°C and 25°C with daily maximum temperatures as high as 35°C during the dry season. With regard to precipitation the area on the escarpment can be considered as part of the humid zones in the country with a mean annual rainfall ranging between 1200 mm and 1500 mm. The June-September rainfall (*Kiremt*) ranges between 400 and 700 mm and the February-May rainfall *(Belg)* commonly range between 400 and 600 mm with about 200 mm of rain distributed in the rest of the year. The Kola zone in the rift floor, which is in the rain shadow of the escarpments, generally gets half this quantity of rain predominantly in the Kiremet season.

Generally, the region has good agricultural soil and the quantity of precipitation determines the type of crops cultivated. The Weyna Dega zone is intensely cultivated and has a high population density (over 300 p/km^2) with a farming and pastoral system of the Enset Culture. The quantity of precipitation make the Weyna Dega zone a low crop risk zone and enable to produce cash crops such as coffee, enset, maize and a variety of legumes which provide the stapple food. In the Kolla zone cotton makes the cash crop and maize and legumes make the staple food crops for subsistance farmers. The development of suitable irrigation systems has enabled to cultivate cotton, tobacco and fruits in the mechanized state farm in the rift floor. The natural vegetation where preserved is an open bush land and wooded grass land with particularly acacia trees in the Kolla zone in the rift floor and forest in the weyna Dega Zone**.** Most of the study area along the escarpments is mantled by a thick red lateritic soil. The area in the rift floor has a thick soil cover derived from the volcanogenic lacustrine and alluvial sediments, and less extensive dark brown

soils has developed from the older basic volcanics. Soil erosion is a significant problem in the area and it is noticeable that an effort has been made to preserve the soil by extensive terracing and afforestation.

2.5. Materials

2.5.1. Primary Data Source

Remote sensing is a powerful tool in the collection, analysis, and modeling of environmental data (Oguz H., 2014). Advancement of the science in the last few decades enabled scientists to study the physical, chemical and biological processes of the earth and its interaction with the atmospheric component. Satellite images are the primary sources of information in remote sensing science, thus remotely sensed images have been comprehensively used in this thesis.

For the computation of LST of the northern lake Abaya area, thermal infrared (TIR) remote sensing data from Landsat 7ETM+ (acquired on 12 February 2000, and 27 January 2006), Landsat 8 OLI/TIRS (acquired on 25 January 2014) and Terra ASTER (acquired on 08 March 2003, 01 January 2008, 12 January 2012, 24 December 2016, 28 January 2018, and 01 December 2019) are used. A Landsat image for the study area is identified as path 169 and row 055. In addition ASTER Level 2 Surface Kinetic Temperature data product (AST_08) acquired on the same date as the AST_L1T, and MODIS (MOD11A2) version6 products, an average 8 day per pixel Land Surface Temperature and Emissivity (LST/E) with a 1 kilometer (km) spatial resolution in 1,200 by 1,200 grids are used to validate the derived LSTs using AST_L1T and Landsat images respectively. Availability and less cloud cover of the scene are the criteria's to select those dates.

ASTER Level 1T Precision Terrain Corrected Registered at-Sensor Radiance (AST_L1T) data contains calibrated at-sensor radiance, which corresponds with the ASTER Level 1B (AST_1B) https://doi.org/10.5067/ASTER/AST_L1B.003 that has been geometrically corrected, and rotated to a north-up UTM projection. The AST_L1T is created from a single re-sampling of the

corresponding ASTER L1A (AST_L1A) (https://doi.org/10.5067/ASTER/AST_L1A.003) product.

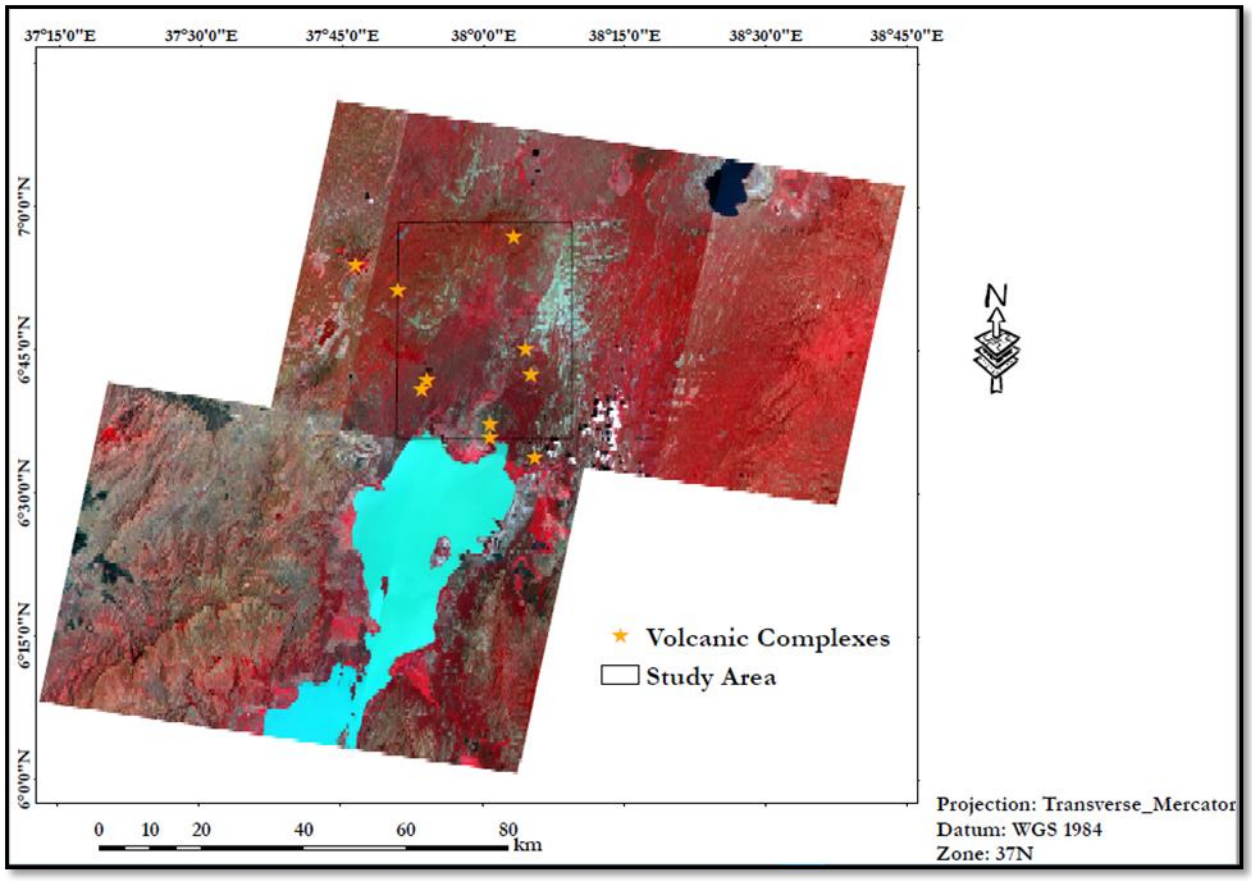

Figure 2. 3 ***ASTER Level 1T (AST_L1T) False color composite (FCC) (Bands3, 2, 1) of the study area (box) and surroundings. Volcanic complexes are shown with in the study area.***

The Landsat images are downloaded from the United States Geological Survey (USGS) whereas AST_L1T and AST_08 were retrieved from the online Data Pool, courtesy of the NASA Land Processes Distributed Active Archive Center (LP DAAC), USGS/Earth Resources Observation and Science (EROS) Center, Sioux Falls, South Dakota, using Earth Explorer (https://search.earthdata.nasa.gov/search). We use ALOSPALSAR Digital Elevation Model (DEM) (http://search.asap.alaska.edu) with a resolution of 12.5m it is used for slope and other structural analysis. The higher resolution of the DEM also allows for a better determination of geological structures.

2.5.2. Secondary Data

Secondary data such as existing geological maps are collected from Geological Survey of Ethiopia (GSE). Geological map of Chericho, Keliso, Tebela and Sodo map sheets at scale of 1:50,000/1:20,000 are used for mapping geological and hydrothermal manifestation in the study area. Rainfall and temperature data of the year 2000-2019 in two years interval from the National Meteorological Agency (NMA).Soil data is collected from the Ministry of Agriculture (MoA). Borehole temperature measurements from published data are used to validate the result of this thesis work. Generally, summary of materials used in this study are indicated in Table 2.

Table 2: Types of Materials and Software used

S/N	Type	Description	Source
1	Map	Geological Map to the scale of 1:50,000	GSE
		Geological Map to the scale of 1:20,000	GSE
		Hydrothermal Manifestation Area	GSE
		Digital Soil Map	MoA
		Study area, towns and Woreda shape files	CSA
2	Images	ASTER Level 1T	https://search.earthdata.nasa.gov/search
		Landsat 8OLI/TIRS	
		Landsat ETM+	USGS
		MOD11A2	
		ALSOSPALSAR DEM	https://lpdaac.usgs.gov/
		ASTER L2 Surface Kinetic Temperature	https://search.asap.alaska.edu
			https://search.earthdata.nasa.gov/search

3	Software	ArcGIS 10.4	ESRI
		ERDAS Imagine 2015	Hexagon Geospatial
		QGIS 3.10.1	www.qgis.org

2.6. Method

ASTER's five band thermal infrared is the major remotely sensed data used in the study. It is a high spatial resolution, 14 bands multispectral imager on the Terra satellite launched in December 1999. It provides TIR images with a 90-m spatial resolution in five channels over 8–12 μm (ASTER user guide, 2003).In addition, ASTER has two other subsystems that operate in the visible, near infrared (VNIR) and the shortwave infrared (SWIR) bands having a 15m and 30m spatial resolution respectively.

The only major ASTER instrument related problem to date deals with the SWIR sensor, which suffered a setback due to its anomalously high detector temperatures. Even if scenes from April 2008 onward lack the SWIR band (ASTER User guide, 2015), ASTER still has great potential for estimating LSTs because of its multiple TIR channels. It has a potential to map the presence of hot springs, fumaroles and heated ground surfaces. Utilizing ASTER for this study also had the benefits of choosing up to 8 years combined optical VNIR-SWIR and 18 years TIR emission archived imagery, available at no cost.

ASTER's Level 2 Surface Kinetic Temperature product (AST_08) is also easily accessible and well validated (Abrams, 2000; Abrams et al., 2015). The (AST_08) is generated using the five thermal infrared (TIR) bands (acquired either during the day or night time) between 8μm and 12μm spectral range. It contains surface kinetic temperatures at 90m spatial resolution for the land areas only. Surface kinetic Temperature provides a vital input to studies of volcanism, thermal inertia and high-resolution fire mapping. It is derived using the same algorithm as the ASTER Surface Emissivity AST_05 product. The (AST_08) data product is only available through NASA's Earth data Search.

Thermal bands of the Landsat 7ETM+ and 8OLI/TIRS are also used, particularly to the years that an ASTER scene of the area were not available. Band 13 of ASTERs TIR, since it has the lowest uncertainty on emissivity (Ee=0.01) and it provides a good statistical fit, with the lowest standard error of estimation (σ=0.6K) and high correlation (γ=0.98) (Jimenez M., 2007), Band 6 (high gain) of ETM+ since its applicable on LST estimation of Land (non desert, non ice) cover type of the Earth (USGS,Landsat7 Handbook) and Band 10 of OLI/TIRS (since band 11 has a stray light effect on LST estimation and it is recommended not to be used by the provider USGS (USGS, 2015) are selected for the study. The spectral bandwidth of the thermal bands for ETM+ and OLI/TIRS is 10.4–12.5 μm and 10.6–12.5 μm respectively (Table 2.1).

Table 2.1 ASTER and Landsat Sensor Characteristics (ASTER User guide, 2015)

Instrument	Band Number	Wavelength range (μm)	Spatial Resolution (m)	Radiometric Resolution (bit)
ASTER VNIR	Band 1	0.52 - 0.60	15	8
	Band 2	0.63 - 0.69		
	Band 3	0.76 - 0.86		
ASTER SWIR	Band 4	1.600 - 1.700	30	8
	Band5	2.145 - 2.185		
	Band 6	2.185 - 2.225		
	Band 7	2.235 - 2.285		
	Band 8	2.295 - 2.365		
	Band 9	2.360 - 2.430		
ASTER TIR	Band 10	8.125 - 8.475	90	12
	Band 11	8.475 - 8.825		
	Band 12	8.925 - 9.275		
	Band 13	10.25 - 10.95		
	Band 14	10.95 - 11.65		
Landsat ETM+	Band 6	10.40 - 12.50	60	8

Landsat8 OLI/TIRS	Band 10	10.60 - 11.19	100	12
	Band 11	11.50 – 12.51	100	12

Table 2.2: Detailed information of the Data sets used

Type of Sensor	Acquisition Date	Julian Date	Band	Band Width (mm)
ASTER L1T	08 March 2003 01 January 2008 12 January 2012 24 December 2016 28 January 2018 01 December 2019	215 01 12 359 28 335	Band 13	10.25 - 10.95
Landsat ETM+	12 February 2000 27 January 2006	43 27	Band 6	10.40 - 12.50
Landsat OLI/TIRS	25 January 2014	25	Band 10	10.60 - 11.19
AST_08	Same as the AST L1T			
MOD11A2			31 and 32	10.78-11.28 11.77-12.27

The study is carried out in five stages (Fig. 2.3). First, remote sensing data is preprocessed to correct for atmospheric and radiometric effects, and geospatial data (geologic maps) are digitized and geo-referenced. ASTER L1T, Landsat ETM+ and Landsat 8 OLI/TIRS visible, near infrared, and thermal infrared images (2000-2019 in two years interval (except for some years)) are radio-metrically calibrated, spectral radiances are converted to Top of Atmosphere (TOA) reflectance (for optical sensors) and TOA brightness temperatures for the thermal bands.

In the second stage, the images are processed using emissivity and brightness temperature calculations to determine the LST of the area. In the third stage, MODIS LST, ASTER L2 (AST_08) products are used to validate the derived LSTs. In order to convert the MODIS LST

and ASTER level 2 data products to a degree of Kelvin the data were multiplied by their respective scaling factor 0.02 and 0.01 respectively, as recommended by the providers USGS and LP DAAC. Fourth stage is geothermal anomaly detection using the preprocessed, medium-resolution satellite imagery. Finally, LST values for the last 20 years in 2 years interval is evaluated and a geothermal anomaly map is produced.

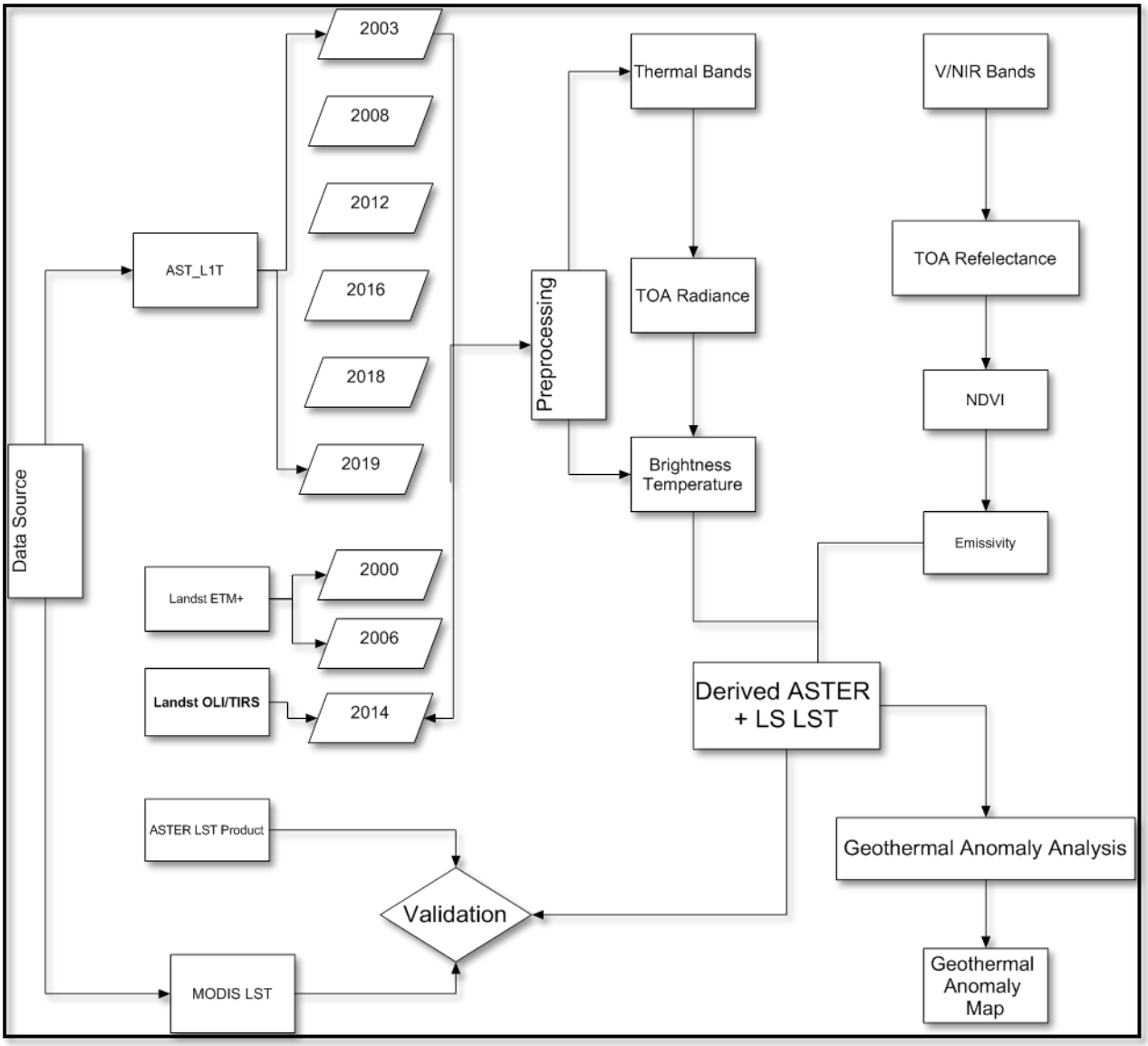

Figure 2. 4 ***Flow Chart***

2.6.1. Pre-Processing

Satellite images are subjected to distortion, they may have either radiometric, geometric or both type of distortion. A pre processing also referred as image restoration and rectification, attempts to minimize these effects to the extent desired for a particular application. It intended to correct for sensor and platform specific radiometric and geometric distortions of data. Normally it should be carried out prior to the main data analysis and extraction of information. The preprocessing steps can significantly impact analysis results (Sundaresan et al., 2007) and have a general order in which they should be performed

Atmospheric correction and radiometric calibration were made for the red, near infrared and thermal infrared bands of both the Landsat and ASTER images using Dark Object Subtraction (DOS) algorithm.DOS is the simplest and mostly used algorithm especially for atmospheric correction, it assumes that reflectance from dark objects includes substantial component of atmospheric scattering. DOS searches each band for the darkest pixel value. The scattering is removed by subtracting this value from every pixel (Landsat data processing in ENVI). The satellite images used are ortho rectified (Terrain corrected) by the provider (https://search.earthdata.nasa.gov/search).

2.6.2 Radiometric correction

It's an act of correcting image data for sensor irregularities and sensor or atmospheric noises by converting the data so that they can accurately represent the reflected or emitted radiation measured by the sensor. At-sensor radiances measured in wavelength region is converted to Digital Numbers (DNs) using a quantification system for the sake of storage and data transfer convenience. DN values have no unit and any physical connotation, therefore, need to be converted to radiance, then to at-sensor (top-of-atmosphere) reflectance/temperature and, further, to surface reflectance and LST in order to draw quantitative analysis from remote sensing data (Ghulam,2009; USGS 2014).

2.6.3. Conversion of Digital Number (DN) to spectral radiance.

The at sensor radiance values at different wavelengths are stored as digital numbers (DN) for convenience during data storage and transfer (Table 2.3). The DN values of the thermal band 13 and visible to near infrared bands of 2 and 3 for ASTER stored as DN values were converted into spectral radiance values using equation 1. The *UCC* value for each band represents the gain setting used during image acquisition, which can be known from the header file associated with AST_ L1T.

$$Lrad, x = UCCx * (DNx - 1) \quad (3)$$

Where, Lrad = the spectral radiance of band x, UCCx = the unit conversion coefficient of band x.

The DN values of the thermal band 6 of Landsat ETM+ and band 10 of Lndsat8 TIRS and visible to near infrared bands of 3and 4 for ETM+ and 4 and 5 of Landsat OLI data's stored as DN values were initially converted to spectral radiance values using equation 2. Constants are provided by USGS from header file associated with the Landsat product (Table 2.4).

$$L\lambda = ML * Qcal + AL \quad (4)$$

Where, Lλ = Spectral radiance ((W/ (m^2 * sr * μm)); ML= Radiance multiplicative scaling factor for the band (RADIANCE_MULT_BAND_n from the metadata); AL = Radiance additive scaling factor for the band (RADIANCE_ADD_BAND_n from the metadata); Qcal = Level 1 pixel value in DN.

Table 2.3: ASTER unit conversion coefficients (UCC) (ASTER User handbook,)

	Unit Conversion Coefficients (UCC) (W m^{-2} sr^{-1} μm^{-1})			
Band	High gain	Normal	Low gain 1	Low gain 2

1	0.676	1.688	2.25	
2	0.708	1.415	1.89	NA
3N	0.423	0.862	1.15	
3B	0.423	0.862	1.15	
4	0.1087	0.2174	0.2900	0.2900
5	0.0348	0.0696	0.0925	0.4090
6	0.0313	0.0625	0.0830	0.390
7	0.0299	0.0597	0.0795	0.332
8	0.0209	0.0417	0.0556	0.245
9	0. 0159	0.0318	0.0424	0.265
10		0.006822		
11		0.006780		
12	NA	0.006590	NA	NA
13		0.005693		
14		0.005225		

Table 2.4: LANDSAT Radiance Scale Factors

Scaling Factors			
Sensor	**Band Number**	**ML**	**AL**
Landsat ETM+	Band 3	0.62165	-5.62165
	Band 4	0.9693	-6.06929
	Band 6	0.037205	3.16280
Landsat OLI/TIRS	Band 4	0.010308	-51.56856
	Band 5	0.0063078	-31.53903
	Band 10	0.0003342	0.1
	Band 11	0.0003342	0.1

2.6.4 Solar Correction

After calculating at sensor radiances, planetary reflectance for ASTER bands (2 and 3N only) are computed using the Equation 3 (Ghulam 2009):

$$\rho TOA = \pi * Lrad * \frac{d^2}{Esun} * \cos(\theta) \qquad (5)$$

Where; ρTOA is unit less planetary reflectance; *Lrad* is at sensor radiance; *d* is Earth-Sun distance in astronomical units (from Table2.5); *E*SUN is mean solar exo-atmospheric irradiances (Table 6), and θ is Solar zenith angle in degrees (zenith angle = 90– solar elevation angle), which is found in the ASTER header file. The calculation of $\mathbf{E_{SUN}}$ is the same for whatever sensor we are using (Ghulam, 2009). NDVI values can be computed easily after planetary reflectance values are calculated for NIR and red bands of a given sensor.

Table 2.5: Earth-Sun Distance in Astronomical Units (Ghulam, 2009)

Earth-Sun distance in astronomical distance									
DOY	***Distance***	***DOY***	***Distance***	***DOY***	***Distance***	***DOY***	***Distance***	***DOY***	***Distance***
1	0.98331	74	0.99446	152	1.01403	227	1.01281	305	0.99253
15	0.98365	91	0.99926	166	1.01577	242	1.00969	319	0.98916
32	0.98536	106	1.00353	182	1.01667	258	1.00566	335	0.98608
46	0.98774	121	1.00756	196	1.01646	274	1.00119	349	0.98426
60	0.99084	135	1.01087	213	1.01497	288	0.99718	365	0.98333

Table 2.6: ASTER mean solar exo-atmospheric irradiances (Ghulam 2009)

Band	***Smith: ESUN***	***Thome et al (A): ESUN***	***Thome et al (B): ESUN***
1	1845.99	1847	1848
2	1555.74	1553	1549

3N	1119.47	1118	1114
3B	NA	NA	NA
4	231.25	232.5	225.4
5	79.81	80.32	86.63
6	74.99	74.92	81.85
7	68.66	69.20	74.85
8	59.74	59.82	66.49
9	56.92	57.32	59.85

2.7. Algorithm and Parameter Calculations

McMillin(1975), proposed that Split Window Algorithm (SWA) using the differences in the atmospheric absorbance of two adjacent Long wave infrared (LWIR) bands can be used to accurately retrieve the sea surface temperature (SST) (Rozenstein O.2014). It is an algorithm for observing the ocean surface temperature based on AVHRR thermal infrared data. The principle is that two adjacent thermal infrared bands have different absorption characteristics; the attenuation information of the atmosphere on the thermal radiation can be obtained by the difference between the brightness temperatures of the two TIR bands. The SWA is widely used due to the fact that it has less dependence on atmospheric parameters and is simple to operate.

2.7.1 Retrieval of Normalized Difference Vegetation Index (NDVI)

Normalized difference vegetation index (NDVI) is calculated using the near infrared (NIR) and RED bands. These bands corresponds to band 2 (RED) and 3N (NIR) for ASTER, band 3and 4 for Landsat 7ETM+ and band 4 and 5 for Landsat OLI/TIRS using equation 4. This NDVI value is used as an input to calculate emissivity values.

$$NDVI = \frac{\rho NIR - \rho RED}{\rho NIR + \rho RED} \qquad (6)$$

Where ρNIR is the spectral reflectance of near infrared band and *ρRED* is the spectral reflectance of red band.

Table 2.7: List of bands used to calculate Normalized Difference Vegetation Index (NDVI)

Sensor	**RED**	**Near Infrared**	**Wavelength(μm)**	
			RED	NIR
Landsat ETM+	Band 3	Band 4	0.63-0.69	0.77-0.9
Landsat OLI/TIRS	Band 4	Band 5	0.64 - 0.67	0.85 - 0.88
ASTER	Band 2	Band 3	0.63-0.69	0.76-0.86

2.7.2 Emissivity retrieval using NDVI

The Land Surface Emissivity (LSE (ε)) must be known in order to estimate LST; it is the relative ability of a surface material to emit energy by radiation. All bodies emit radiation naturally and a body emitting the maximum possible amount of radiation at a given temperature over a unit surface area is called a black body and its emissivity is set equal to unity. Thus, emissivity of a given object is the ratio between the energy emitted by the surface in question and the energy emitted by a black body held at the same temperature. Emissivity is a significant factor determining LST extracted from the Thermal Infrared satellite images; it is the efficiency of transmitting thermal energy across the surface into the atmosphere (Jimenez Munoz et al., 2006).

In this study, Jimenez-Munoz et al (2006) approach has been adopted to retrieve land surface emissivity using NDVI values since this method has been tested against in situ measurements by different authors. The results indicated that this method gave root mean square errors (RMSE) <0.005 over vegetated areas. This approach is based on the following simplified equation

$$\varepsilon i = \varepsilon vi + Pv + \varepsilon si(1 - Pv) \qquad (7)$$

Where ε_V and ε_s are the vegetation and soil emissivity, respectively and PV is proportion of vegetation.

*P*V is calculated using equation 6. A method for calculating *P*V suggests using the NDVI values for vegetation (NDVI v) and soil (NDVI s) to apply in global conditions (Sobrino A et al., 2004).

$$PV = \frac{NDVI - NDVIs}{(NDVIv - NDVIs)^2} \quad (8)$$

Surface emissivity for ASTER thermal bands can be computed as shown in equation 9-13 (Jimenez-Munoz et al 2006)

$$\varepsilon 10 = 0.946 + 0.044PV \quad (9)$$

$$\varepsilon 11 = 0.949 + 0.041Pv \quad (10)$$

$$\varepsilon 12 = 0.941 + 0.049Pv \quad (11)$$

$$\varepsilon 13 = 0.968 + 0.022Pv \quad (12)$$

$$\varepsilon 14 = 0.970 + 0.020Pv \quad (13)$$

For the Landsat thermal bands can be computed as

$$\varepsilon = 0.004Pv + 0.986 \quad (14)$$

2.7.3 At-sensor Brightness temperature (BT) estimation

The other step in estimating LST using TIR images is: converting spectral radiance to at-sensor Brightness Temperature (BT). Band 13 of the ASTER TIR (10.25 to 10.95 μm) among the five TIR bands (Band 10 to 14), band 6 of Landsat 7(10.40 to 12.50μm) and band 10 of Landsat 8(10.60 to 11.19μm) are used to compute the LST since they are found in more or less similar wavelength ranges.

The thermal bands are converted from at-sensor spectral radiance to at-sensor BT, assuming that the Earth's surface is a black body (i.e., spectral emissivity equals 1) and atmospheric effects (absorption and emission along the path) have been taken into account (Chander *et al.*, 2009 cited in Nithiyanandam Y. and Nichol E., 2016). The conversion formula for estimating at-sensor BT from at-sensor spectral radiance is:

$$BT = \frac{K2}{\ln\left(\frac{K1}{L\lambda} + 1\right)} \qquad (15)$$

Where BT is at-sensor Brightness Temperature (K), Lλ is corrected at-sensor radiance, and K_1 and K_2 are the prelaunch calibration constants (ASTER) and thermal constants (Landsat) TIR bands.

Table 2.8: Radiation and thermal constants of thermal bands

Sensor	Band	wavelength(μm)	K_1(W/m^{2}srμm)	K_2(K)
ASTER	10	8.125 -8.475	3047.47	1736.18
	11	8.475-8.825	2480.93	1666.21
	12	8.925-9.275	1930	1584.72
	13	10.25-10.95	866	1350.07
	14	10.95-11.65	649.6	1274.49
Landsat 7ETM+	6	10.40-12.50	666.09	1282.71
Landsat 8 TIRS	10	10.6 - 11.19	774.89	1321.08
	11	11.50 - 12.51	480.88	1201.14

The final step is to calculate LST using brightness temperature (BT) of thermal bands and Land Surface Emissivity (LSE) derived from NDVI. LST can be retrieved using equation 9. LST was calculated by applying a structured mathematical algorithm using QGIS 3.10 raster calculator tool.

$$Ts = \frac{Tsensor}{1 + \left(\lambda * \frac{T\ Sensor}{\rho}\right) ln\varepsilon} \qquad (16)$$

Where Ts is the LST in Kelvin (K), BT is at-sensor BT (K), λ is the wavelength of emitted radiance (for which the peak response and the average of the limiting wavelength), ε is the emissivity calculated in (7), and$\rho = h\frac{c}{\sigma}$ which is equal to1.438x10^{-2} mK,

Where σ is the Boltzmann constant (1.38 × 10^{-23} J/K), h is Planck's constant (6.626 × 10^{-34} J s), and c is the velocity of light (2.998 × 10^{8} m/s) (Weng et al., 2004). Here we use the above method to estimate the land surface temperature in the Abaya geothermal site at the southern MER.

2.8. Software Packages

Most of the pre-processing work was done using QGIS 3.10 and Erdas Imagine 2015, which includes the execution of atmospheric corrections and temperature estimation models. Arc GIS 10.4.1 was mainly used to prepare layouts of the results obtained as well as for the derivation of pixel values for temperature images.

3. Chapter Three

Regional Geology and Tectonics

3.1 Main Ethiopian Rift (MER)

3.1.1 Tectonic Setting

The East African Rift System (EARS) is one of the few seismically and volcanically active continental rifts in the world. It extends for about 6,500 km from the Dead Sea Rift in the north to Mozambique in the south.

The EARS is a 50-60 km wide geographic phenomenon bounded by opposed and steeply dipping normal faults. It is divided into eastern and western branches, and is composed of several interacting segments. It is relatively young rifting which started approximately 20-30 Ma ago when the African continental plate split into two separate plates: the Nubian plate to the west and the Somalian plate to the east (Ebinger et al., 1993) Within the EARS, the Main Ethiopian Rift (MER) is of special interest because it connects immature continental rifting to the south to incipient seafloor spreading in the Afar depression to the north.

The MER is divided into three subsectors (Northern, Central and Southern) based on pattern, time of faulting and lithospheric characteristics. (Bonini et al. 2005).These sectors of the MER are characterized by the occurrence of a typical bimodal magmatic activity and two distinct systems of extensional structures: a system of NE-SW to N-S trending border faults and NNE-SSW to N-S trending Wonji Fault Belt (WFB), obliquely affecting the rift floor. (Figure 3.1) These faults developed in response to Miocene-recent motion between Nubian and Somalia

plates; and rift obliquity is believed to have played a major role in the rift evolution (Mohr, 1962, Gibson, 1969; Corti, 2008).

The most recent volcano-tectonic activity within the MER began in the Pleistocene and continues to present day and is related to the axial extensional zone denoted as the Wonji Fault Belt (WFB) (Philippon et al, 2014). The rift records polyphase extension reflecting the narrowing and focusing of the tectonic and volcanic activity toward the rift axis with time (Boccaletti et al., 1998). In particular the evolution of the rift is characterized by (1) the Miocene development of large border faults, accommodating extension and defining a subsiding rift valley and (2) a Pliocene to Quaternary migration of the volcano-tectonic activity toward the rift floor itself. This rift evolution is well expressed at the northern termination of the MER, where rifting is believed to be in a mature stage, whereas to the south rifting becomes less evolved and axial deformation less pronounced. Moreover, extensional structures in south Ethiopia become more complex, as they reflect the interaction between the MER and the Kenya rift that overlap in a 300-km-wide system of extensional basins. Timing, style and kinematics of the volcano-tectonic activity is well documented in the northern part and central part of the MER, but detailed geological-structural data are still relatively sparse in the southern MER and the BRZ of southern Ethiopia (Hayward and Ebinger, 1996; Ebinger et al., 2000 Wolfenden et al., 2004; Agostini et al. 2011 cited in Philippon et al, 2014).

3.1.2. Segments of MER

The Northern MER extends from the Afar depression up to the Lake Koka region. (Wolfenden et al., 2004)The Boru Toru Structural high separates the NMER from the Central MER (Bonini et al., 2005). It's a magma dominated sector of the MER (Keranen et al. 2004). In the NMER, the boundary faults are oriented ~N40°E started to develop at around 11 Ma. This sector is marked by Arboye and Sire border faults in the east faults and the major western Ankober border fault system which in turn characterized by the structurally complex 'corner' between the NE-trending MER and the N–S trending Red Sea rift (Wolfenden et al., 2004).

The Central MER contains most of the Lakes Region, up to the Lake Hawassa area. The central MER is assumed to develop at 8 Ma (Tsegaye Abebe et al. 2010). This sector of the MER is bounded by the Yerer-Tullu-Wellel volcano tectonic lineament to the north and the Goba–Bonga lineament to the south and by the fault escarpments such as Munesa and Guraghe rift margins to the east and west, respectively (WoldeGabriel et al., 1999; Tsegaye Abebe et al., 2010).

The Southern MER , which is the main focus of this study, is fault- dominated, less pronounced axial deformation, more limited (or absent) magmatic modification of the crust and lithosphere. The activity of the border faults, point to a less evolved rifting stage (Hayward and Ebinger, 1996). Wolfenden et al. 2004 argue that rifting in the southern MER started at around 18 Myr. The SMER lacks a major rift escarpment as might be expected from a rift margin setting, and instead the topographic transition is gentle between the rift floor and highland plateau (Minissale et al., 2017). The sector have trend from N0°E to ~N20°E located within the major fault escarpments of Chencha which is marked by a curvilinear boundary fault having an orientation between N–S and N40°E and Agere Selam eastern margin have linear fault system and is characterized by NNE–SSW trend **(**Boccaletti et al., 1998; Bonini et al., 2005**).**

3.2.2. Magmatism in the MER

Magmatic activity in Ethiopia started with the eruption of Oligocene (~30-35 Ma) voluminous flood basalts followed by a complex shield volcano activity. According to Corti et al., (2010) and references there in, the distribution of volcanic activity in the MER, similar to the rift evolution is characterized by two different phases: an early phase (Miocene-Pliocene) of widespread volcanism encompassing the whole rift and some activity on the shoulders giving rise to off-axis volcanism, followed by a Quaternary phase of volcanic activity localized within the rift along the en-echelon Wonji fault segments, well expressed in the Northern MER.

In the first phase of widespread volcanism, volcanic centers were mainly localized along boundary fault systems pre-existing fabrics both parallel and transverse to the rift axis. These

fabrics most probably controlled the localization of magmatic activity at major transfer zones, as it is observed in the Western Branch of the EARS and other rift zones worldwide (Ebinger *et al.*,1989; Corti *et alii* 2003a, b, 2004 cited in Corti et al., 2010). During the Miocene-Pliocene phases of rifting, a puzzling characteristic of the volcanic activity is the development of off-axis volcanoes on the plateaus surrounding the rift (Bonini et al., 2001).

The second phase of volcanic activity in the MER occurred at the end of the Pliocene (~2.5 Ma) and was characterized by a substantial change in the distribution of volcanism that was concomitant with the activation of the Wonji fault belt. Quaternary volcanism became indeed focused within the rift depression and strongly localised along the Wonji faults, with only minor activity outside the en-echelon deformation belt. Each segment of the WFB hosts at least one major felsic central volcanic complex of Quaternary age, which has a deep seated magma chambers serving as heat source for the widespread hydrothermal activity in the region (Minissale et al., 2017). Intense magmatic and volcanic activities occurred during the formation of WFB. These magmatic activities were mainly dominated by basaltic lava flows together with aligned scoria and spatter cones (Mohr, 1967).

Two main phases of volcanic episodes are experienced in the Southern MER. The pre-rift flood-basalt event is dated at about 45 Ma confirming that the Tertiary volcanic activity in the Southern MER started earlier than in the other MER sectors. (Mohr and Zanettin 1988, Ebinger et al.,1993, Gezahegn Yirgu et al., 2006; Kieffer et al., 2004 cited in Corti et al., 2010). The volcanic activity in and around the Abaya geothermal field is typically marked by bimodal activities (Minissale et al., 2017).

According to a study by Tadiwos Chernet (2011), the first volcanic activity is constituted by rhyolitic centers characterized by the emission of large volumes of per alkaline lava flows, domes and pyroclastic deposits. These volcanic centers are common along the western rift margin at Hobitcha and Doguna volcanoes, although some acidic volcanoes (e.g., Chericha volcnao) are observed at the rift axis (Figure 3.1). Very recent obsidian and pitchstone flows are located near the southern edge of the Hobitcha caldera, at Salewa-Dore and Hako volcanic

centers. These latter centers represent the youngest rhyolitic activity in the area and are characterized by ongoing steam vents and steaming ground activity. These are considered to host a shallow magma chamber that serve as the heat source for geothermal resource in the area. The second stage of volcanic activity is characterized by basaltic lava flows, scoria cones and phreatomagmatic deposits. The basalts are associated with the recent faults located in the western part of the rift valley.

3.3. Geology of the Study Area

The Northern Lake Abaya area is one of the Lake District geothermal prospects, which is located in the western half of the southern part of the Main Ethiopian Rift (MER). Similar to other places along the EARS, the area shows significant recent and ongoing volcano-tectonic activity. It also hosts a variety of surface heat manifestations as springs and fumaroles that indicate the existence of economically exploitable geothermal resources (Tadiwos Chernet, 2011; Corti et al., 2013; Philippon et al., 2014; Minissale et al., 2017).

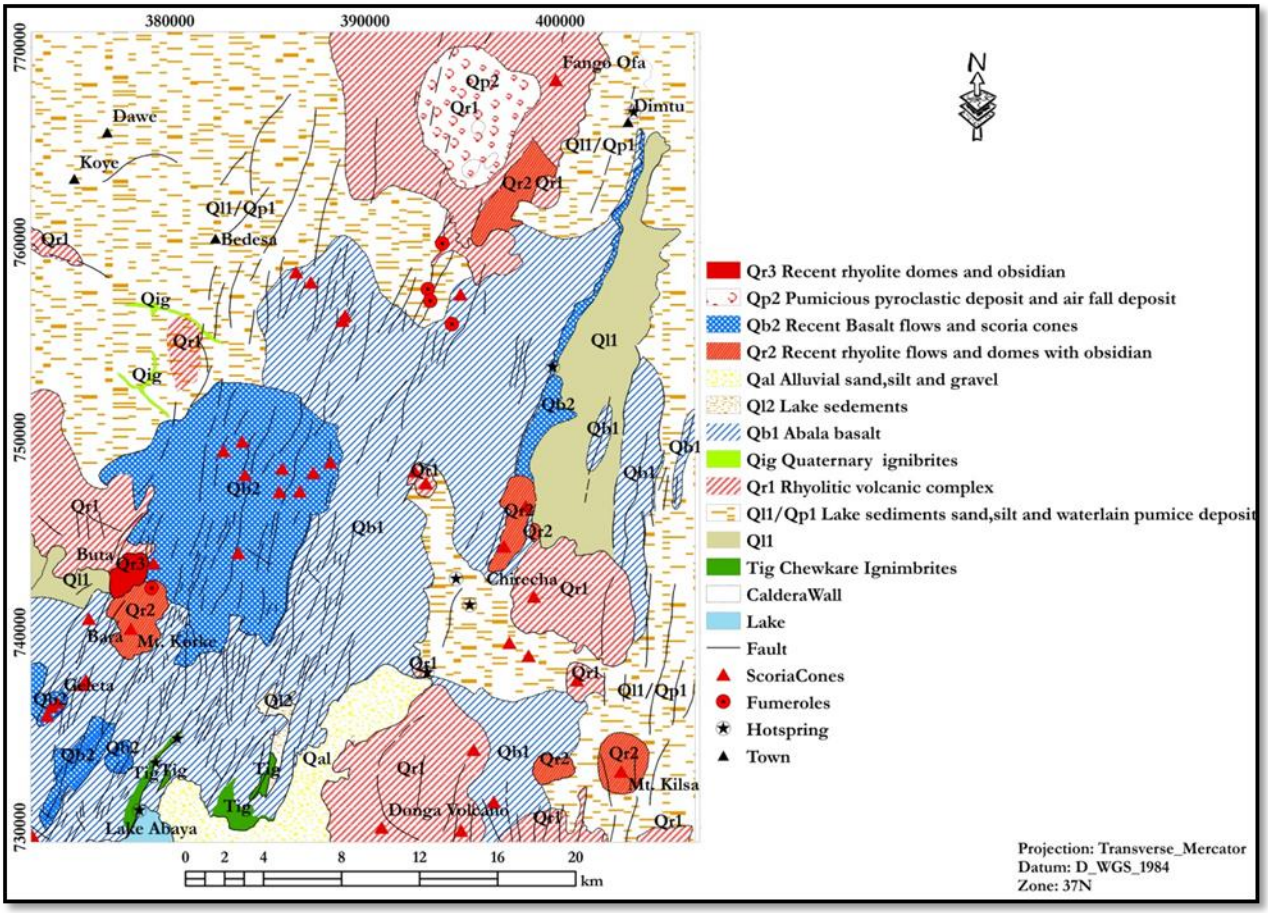

Figure 3. 1 Geological Map of the study area adopted from Tadiwos Chernet, 2011.

3.3.1 Stratigraphy

Most of the rift floor is covered by post-rift volcanic and volcano-sedimentary units with pre-rift rocks cropping out only along the western escarpment and plateau. The geology of the study area is summarized based on the work of Tadiwos Cherenet (2011). Here we describe the units from the oldest to the youngest units.

Pre-rift basalts (Tb1)

Intensely jointed, hydro thermally altered and spheriodally weathered basalt outcrops on the southwestern part of the study area on the series of faults forming the western escarps of the graben where Lake Abaya is situated.

Chewkare Ignimbrites (Ti)

Crystal rich, colored, (brownish and grayish green) ignimbrites exposed on the western Abaya fault forming the Western margin of an approximately 10km wide graben (Chewkare) at the northern tip of Lake Abaya. The outcrop has an exposed thickness of about 100 m and is overlain by lacustrine sediments (Ql1) which is intervened by Quaternary basalts. It is estimated that the geological unit aged around 4.4Ma (EIGSGEP, 1981) which makes it correlable with the Tertiary Nazret Group Ignimbrites of the northern and central MER.

Damota trachyte (Tt2)

Exposures of Damota trachytes are light greenish gray, porphritic (anorthoclase) trachyte with cooling joints that are more weathered near the flanks of the shield than near the summit. No absolute isotopic age determination exists for Damota lavas, but it has been generally accepted that Damota is correlable to genetically similar centers of the MER and hence its Pliocene age, however its more youthful features suggest that activity might have continued into the Quaternary.

Quaternary Ignimbrites (Qi)

Brown, lithic rich, weakly welded Ignimbrites traced in the western part of the study area, the units are found in the west and south west of the Obicha caldera. The units appear interstratified with Quaternary basalts in river valleys forming tributaries to Hamesa River, indicating that the lacustrine sediments are younger. The fact that the ignimbrites are exposed in river valleys in an area mantled by Quaternary volcanoclastic sediments indicates that the ignimbrites for the most part are older than the lacustrine sediments.

Quaternary basalts (Qb1 and Qb2)

Geological units covering most part of the study area are two Quaternary basalt members (Qb1 and Qb2).The NNE trending fault swarm along the axis of the rift floor has been a conduit for basaltic eruptions with lines of scoria cones making fault traces. Degree of preservation of volcanic structures and intensity of post- emplacement tectonic movement of flows are the criteria's to distinguish between the two basaltic units. These Quaternary basalts in some exposures are interstratified with the earlier succession of the lake sediments (Ql1).

A broad area between Lake Abaya and Duguna Fango is covered by Basaltic effusion (Qb1) the Abela basalts, fissural basalt flow which is commonly vesicular. It is exposed all along the Bilate River bed and banks for most of its course in the study area. The younger episode of basaltic eruptions, recent basalt flows and scoria cones crops out near the northwest Abaya hydrothermal field.

Rhyolitic volcanic centers (Qr1, Qr2 and Qr3)

Quaternary rhyolitic volcanic centers which astride along the active volcano-tectonic axis of the rift have produced large volumes of peralkaline lava flows (Qr1, Qr2 and Qr3) and pyroclastic deposits (Qp). Hobitcha rhyolitic center with a horse shoe shaped caldera structure with a diameter of 10 km is situated off the active axis of the rift adjacent to Damota volcano.

Duguna Fango volcanic complex is the most prominent of the Quaternary volcanic centers with a summit caldera which produced pumice and ash fall deposits (Qp).The Salwa Dore – Hako rhyolitic center have produced very recent obsidian and pitchstone flows probably representing the youngest rhyolitic activity (Qr3) in the study area.

Lacustrine sediments (Ql1, and Ql2)

Two major lacustrine sedimentary units (Ql1, and Ql2) were characterized. The earlier unit (Ql1) is generally yellowish - grey colored, horizontally bedded and poorly sorted with fragments of rhyolite, obsidian and basalt in a matrix of fine tuffaceous ash related to the pluvial periods of the

Pleistocene. The second phase of lacustrine sedimentary unit (Ql2) is related to fluctuations of the present Lake Abaya level during the Holocene and is restricted to the vicinity of the lake. These lacustrine sediments form an important cap-rock for the hydrothermal system in the study area.

Alluvium (Qal)

The lower courses of two major rivers (Bilate and Gidabo) which drain most of the study area into Lake Abaya are covered by fluvial deposits along the gentler courses. As regional studies has indicated the Tertiary volcanic succession down faulted in the rift is the reservoir rock for the prevailing hydrothermal system with graben filling lacustrine sediments providing a cap-rock (Lloyd, 1977).

3.3.2 Hydrothermal Activity.

Most hydrothermal features in the study area are concentrated along the NNE-SSW trending fault system on the western part of the Chewkare graben. Here we describe some of the major hot springs and fumaroles in the study area.(Figure 3.2)

1. **Northwest Abaya Fault hot springs and fumaroles: -**These springs and fumaroles emerge at the base of the western boundary fault of the Cherwkare Graben and discharge near the shores of the lake. The maximum temperature of the springs is 95°C (Solomon Kebede.2015).

2. **Salwa Dore and Hako domes (Qr3):-** are located in a NNE-SSW trending graben about 3 km wide and 5 km long (Salwa Dore–Hako Graben). (Tadiwos chernet,2011) At the summit of Salwa Dore numerous weak steam vents from within the blocky glassy bare rocks discharge steam at about 90°C.Hydrothermal alteration is minor and restricted to the vicinity of the vents. Similarly at the summit of Hako from a deep joint within the recent pitchstone weak steam vents discharge steam at a temperature of about 42°C.

3. **Bolocho – Metincho hot springs: -** These springs are located close to Bilate River and Chericho volcano.

   The Bolocho Area:- group of springs has forming a number of pools which fill depressions on top of sinter and travertine cones which rise about 3 m high from the surrounding plain and have a base diameter of about 200 m. The springs have a pH of 8-8.5 and temperature ranging from 48 to 91°C.

   The Metincho Area: - High discharge hot springs (>100 l/s) in this area drain to the nearby Bilate river. Most discharge points are surrounded by a swampy and algal overgrowth with a thin film of $NaHCO_3$ formed on the drier grounds. Temperature of the springs ranges between 45 ℃ and 55 ℃ and average pH of about 7.5.

4. **Bilbo active fumarolic and fossil hotspring areas** are located on the southern flanks of Duguna Fango volcanic complex. The Anka Bilbo fumaroles are situated along the Wadu stream, where hot ground and weak fumarolic vents with a temperature as high as 89 ℃ emerge from a country rock consisting of rhyolitic glass. Hydrothermal alteration along the fault scarp is brick-red and yellowish clay around the vents and minor travertine and sinter deposition.

5. **Tobacco Plantation hot springs** emerge from vesicular basalt flow unit (Qb1) which makes Bilate River bed. Temperature of these group springs at the discharge point ranges between 50 ℃ and 61 ℃ with a near neutral pH. No significant hydrothermal alteration except white bicarbonate salt and iron-oxide stain on the basalt.

6. **Dimtu warm springs** consist of numerous large discharge warm springs with temperature ranging between 38 ℃ and 40℃ and a near neutral pH. The springs emerge from the sand bedded gullies (up to 5 m deep) formed within the lake sediments, to collectively form a stream (>500 l/s) which drains into Bilate River. Hydrothermal alteration is minor and is represented by a thin film bicarbonate salts on the lacustrine sediments

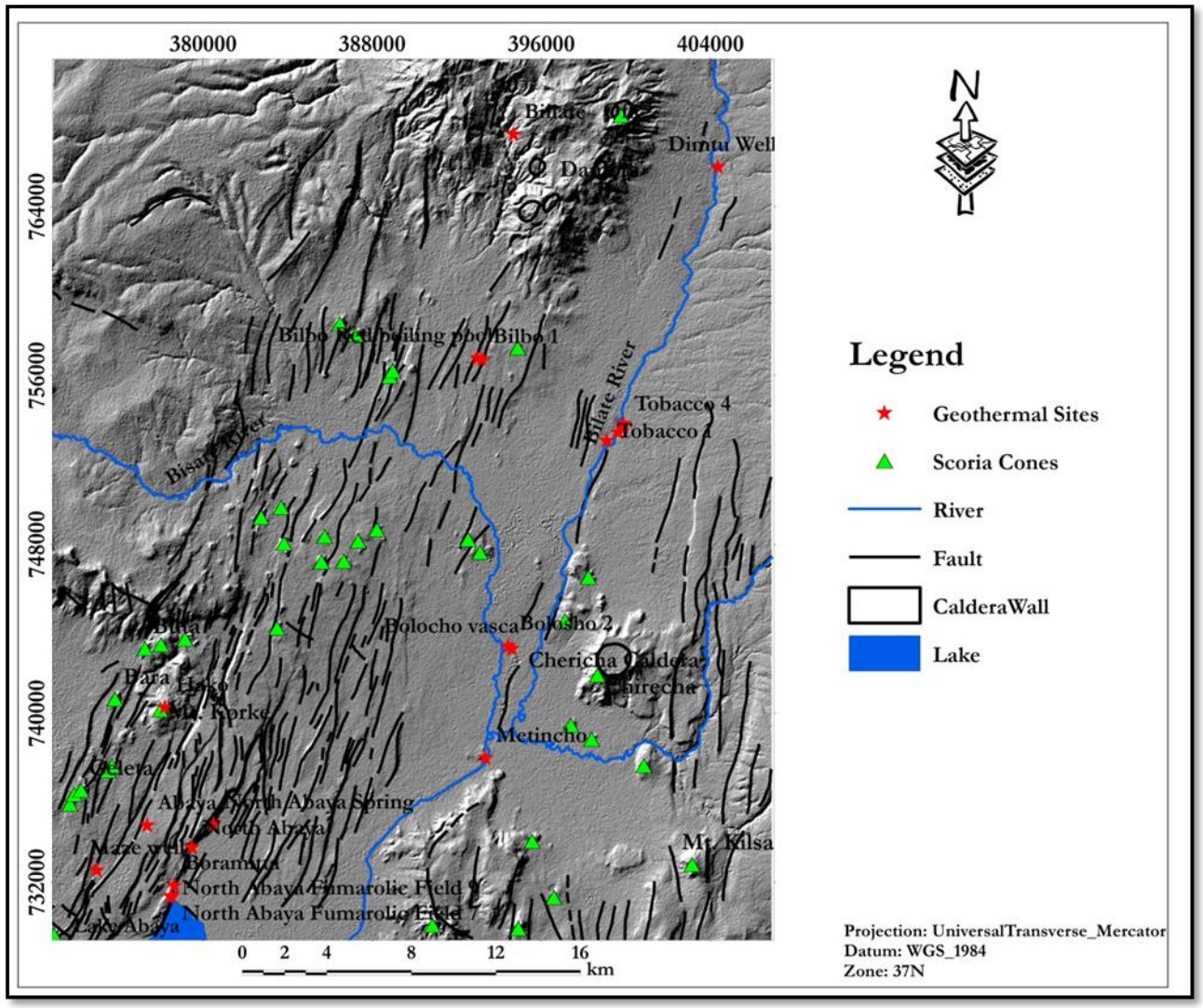

Figure 3. 2 ***Location of major Quaternary volcanic complexes and hydrothermal manifestations in the northern Lake Abaya Geothermal prospect.***

4. Chapter Four

Results

4.1. Normalized Difference Vegetation Index (NDVI)

Normalized Difference Vegetation Index (NDVI) is essential to identify different land cover types of a given area. It is calculated on per-pixel basis as the normalized difference between the red and near infrared bands (Table 2.7) of the images using equation 4. Generally NDVI values are in the range of -1.0 to +1.0.

The output values range between -0.69 to 0.65 for the year 2000; - 0.41 to 0.89 for the year 2003; -0.41 to 0.57 for 2006; 0.17 to - 0.88 for the year 2008; 0.93 to -0.23 for the year 2012; 0.52 to-0.19 for year 2014; 0.89 to -0.60 for the year 2016; 1 to -0.133 for the year 2018 and 0.933 to -0.19 for the year 2019.

The lowest values represented by red color indicate areas with no vegetation, whereas those appearing green are highly vegetated areas with higher NDVI values. The lowest positive values of the study area are less vegetated soils and barren lands. Water bodies have negative values since water has high absorption and virtually no reflectance in the near infrared wavelength ranges and beyond. Vegetated areas, such as forest near and on the elevated areas, crop lands near the lake and the tobacco plantation corresponds to higher NDVI values in the study area (Fig 4.1)

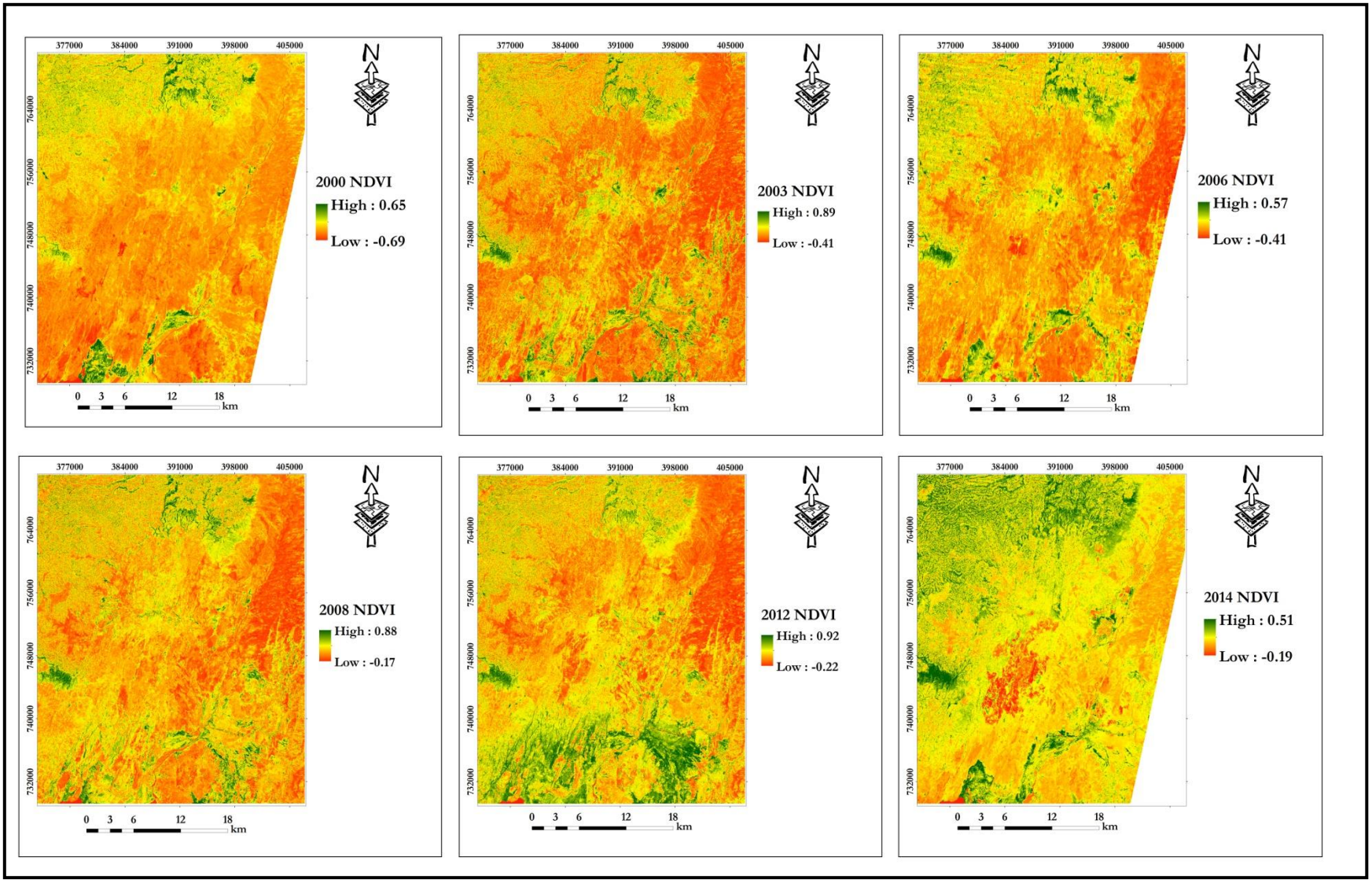

Figure 4.1 NDVI maps for the year 2000, 2003,2006,2008,2012 and 2014.

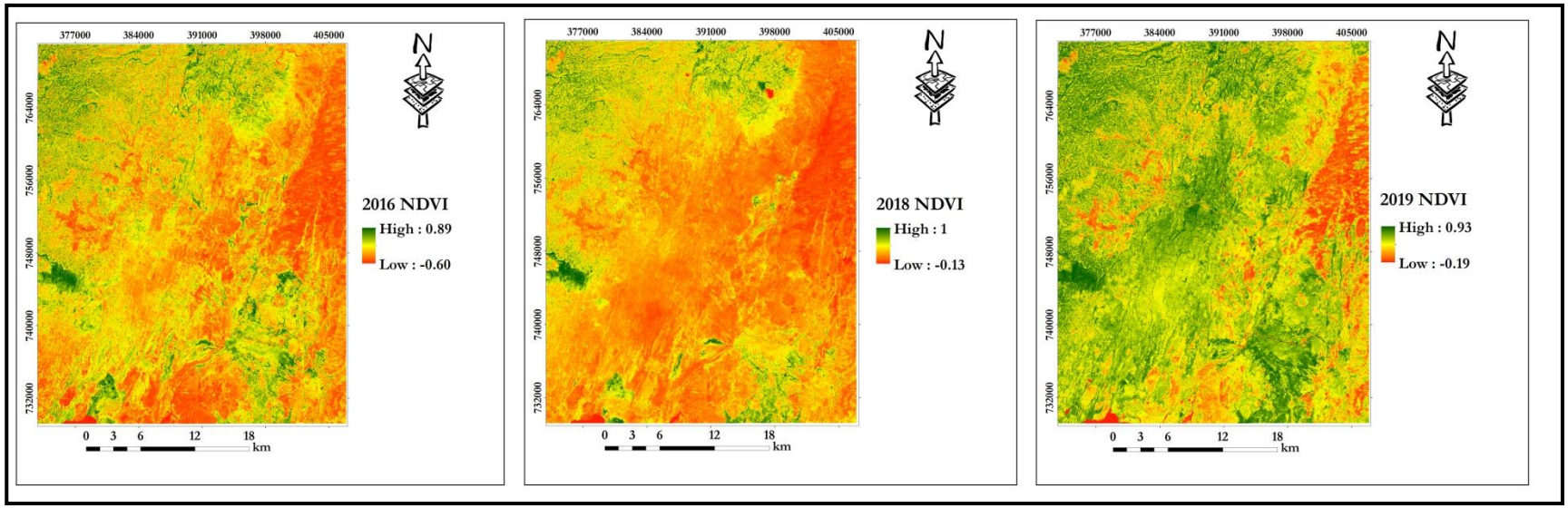

Figure 4. 1 *NDVI maps for the year 2016, 2018 and 2019.*

The maximum and minimum values of NDVI being values for vegetation ($NDVI_V$) and soil ($NDVI_S$) respectivel……..y serve as inputs for the calculation of PV, which is proportion of vegetation and an important factor for calculating emissivity (ε).

Table 4.1 Maximum and minimum NDVI values of Northern Lake Abaya (2000-2019).

Year	Maximum NDVI	Minimum NDVI
2000	0.65	-0.69
2003	0.89	-0.41
2006	0.57	-0.41
2008	0.88	-0.17
2012	0.93	-0.23
2014	0.53	-0.19
2016	0.89	-0.6
2018	1.00	-0.13
2019	0.93	-0.19

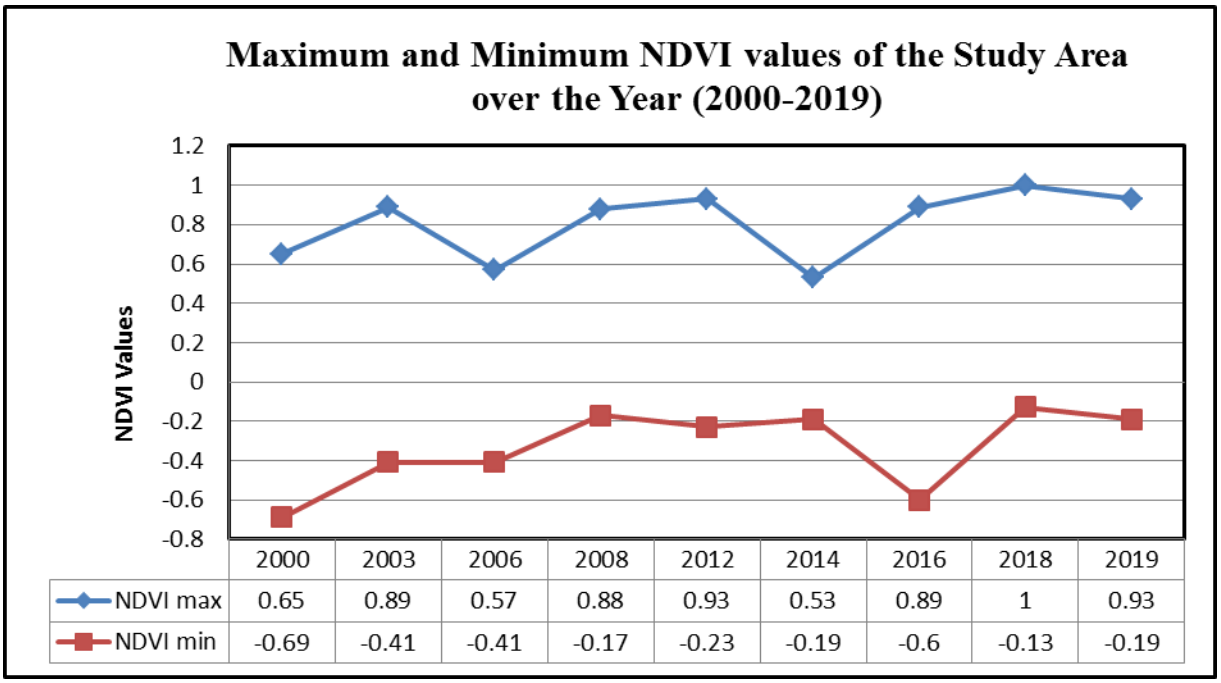

Figure 4. 2 *Max and min value of NDVI*

4.2 Land Surface Emissivity (ε)

Since it is a proportionality factor that scales the black body radiance (Plank's law) to measure emitted radiance and it is the ability of transmitting thermal energy across the surface into the atmosphere (Jimenez M. et al., 2006), LSE is an important parameter to estimate LST .It is calculated using Equation (12) for ASTER images and Equation (14) for the Landsat images. The resulting LSE maps of the study area are shown in Figure 4.4 A-I.

LSE (ε) is highly dependent on the surface roughness and nature of vegetation cover. Areas covered by vegetation generally have higher emissivity values than areas with none.

Table 4.2. Maximum and minimum Emissivity Values of Northern Lake Abaya area

Year	Emissivity Max	Emissivity Min
2000	0.99	0.986
2003	0.987	0.969
2006	0.99	0.986
2008	0.987	0.97
2012	0.987	0.968
2014	0.99	0.986
2016	0.987	0.968
2018	0.99	0.969
2019	0.989	0.968

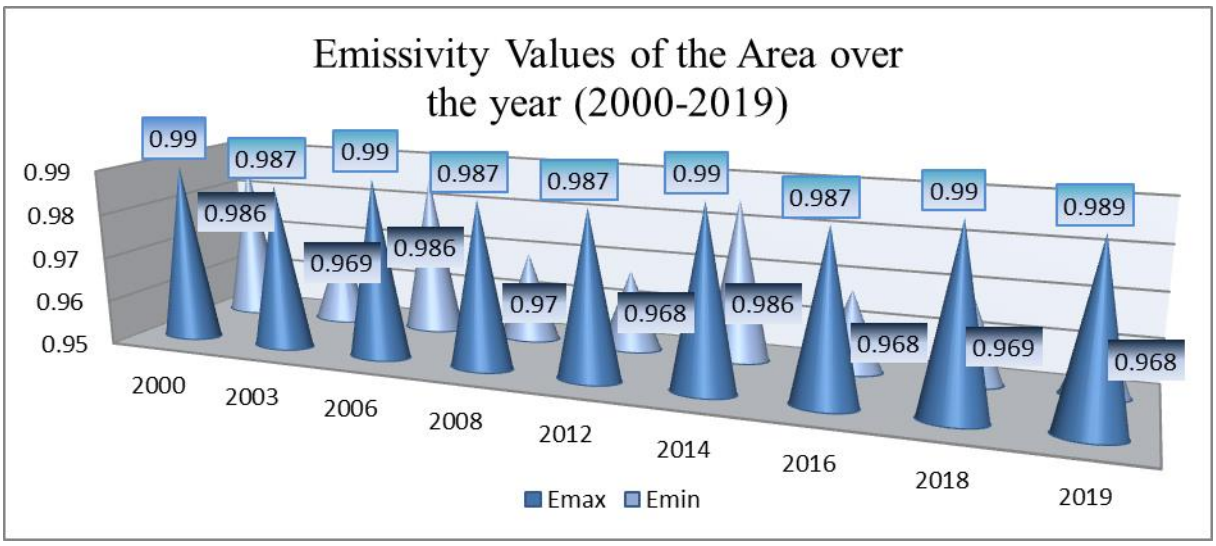

Figure 4. 3 Emissivity values of Northern Abaya Area for the year (2000-2019).

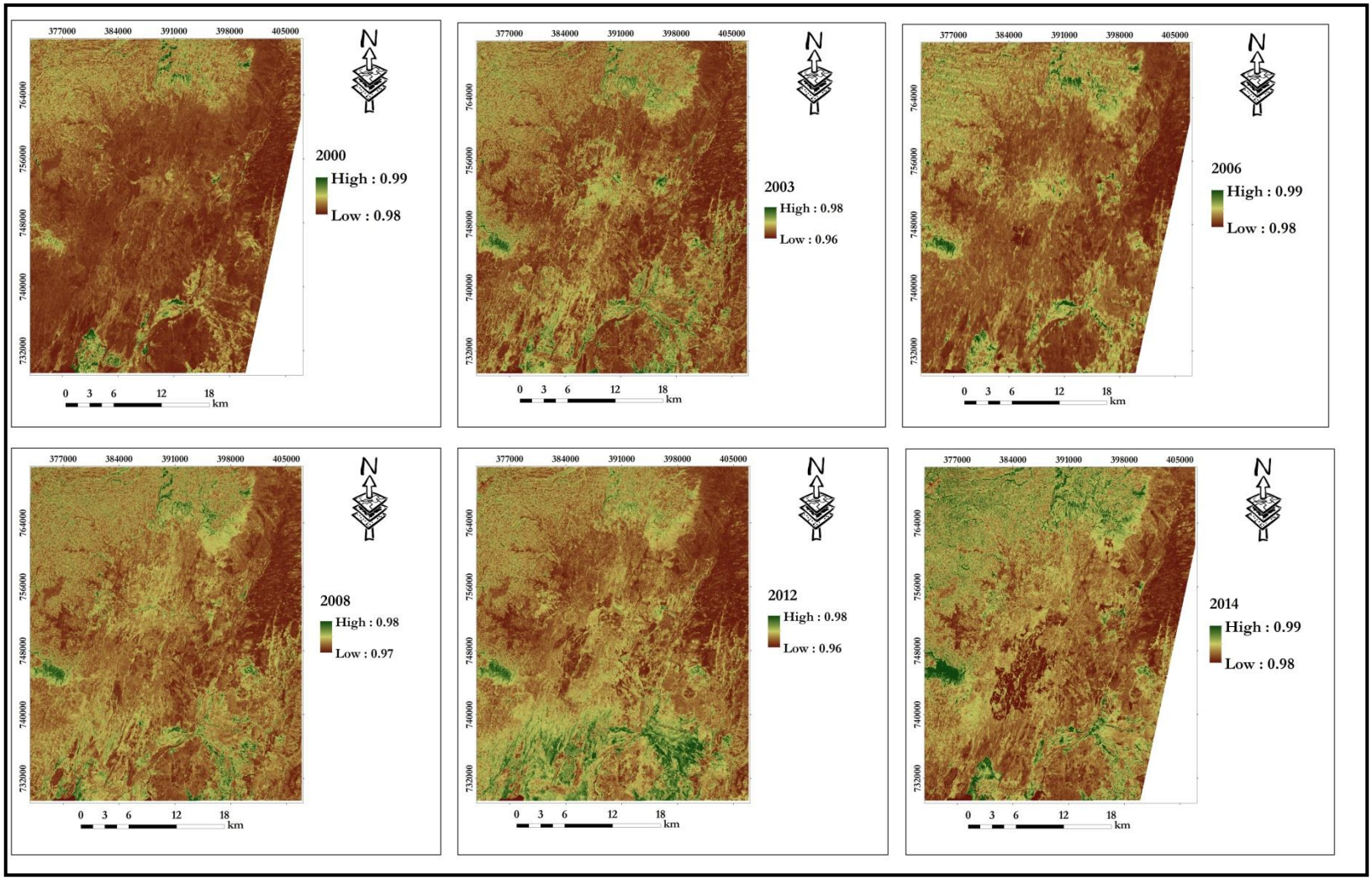

Figure 4.4 **LSE maps of Year 2000, 2003, 2006, 2008, 2012 and 2014.**

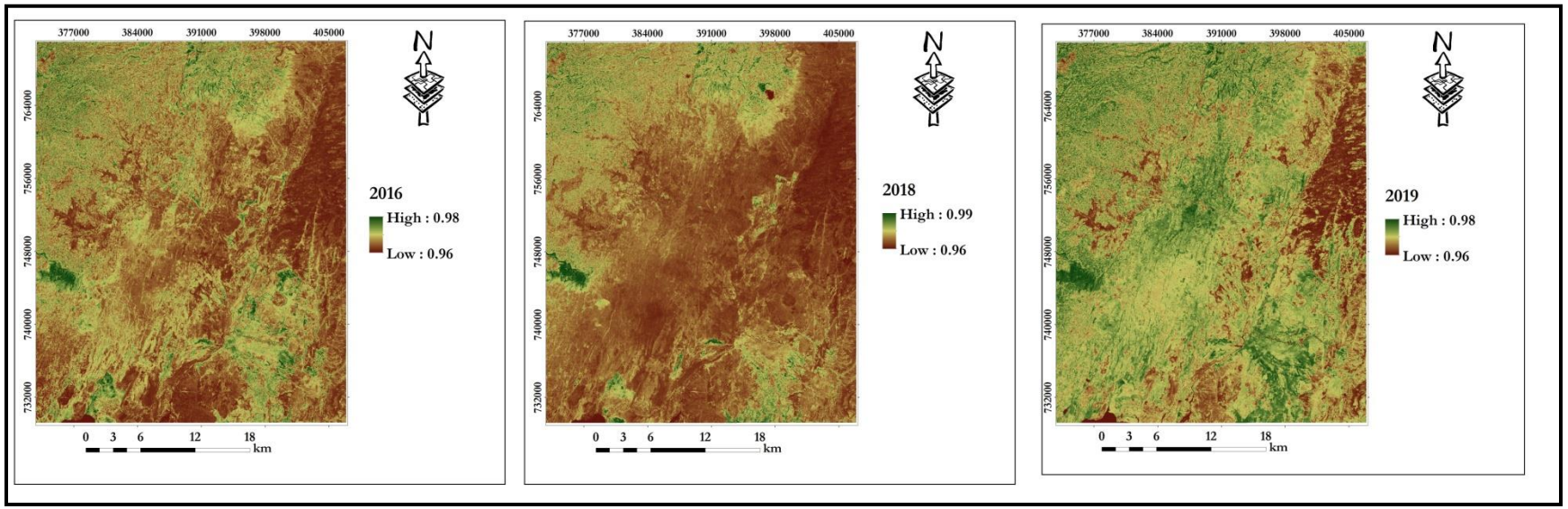

Figure 4. 4 *LSE maps of Year 2016, 2018 and 2019.*

The emissivity value of the study area is more or less the same throughout the given time frame. It is in the range of 0.99 and 0.96; higher emissivity values being traced on densely vegetated areas of Loka Abaya National park and on the elevated areas of the Northern, North western and western parts of the study area. On the other hand, lower LSE values have been traced on the northern tips of Lake Abaya which is found in the South western part of the study area. As shown in figure 4.2.4

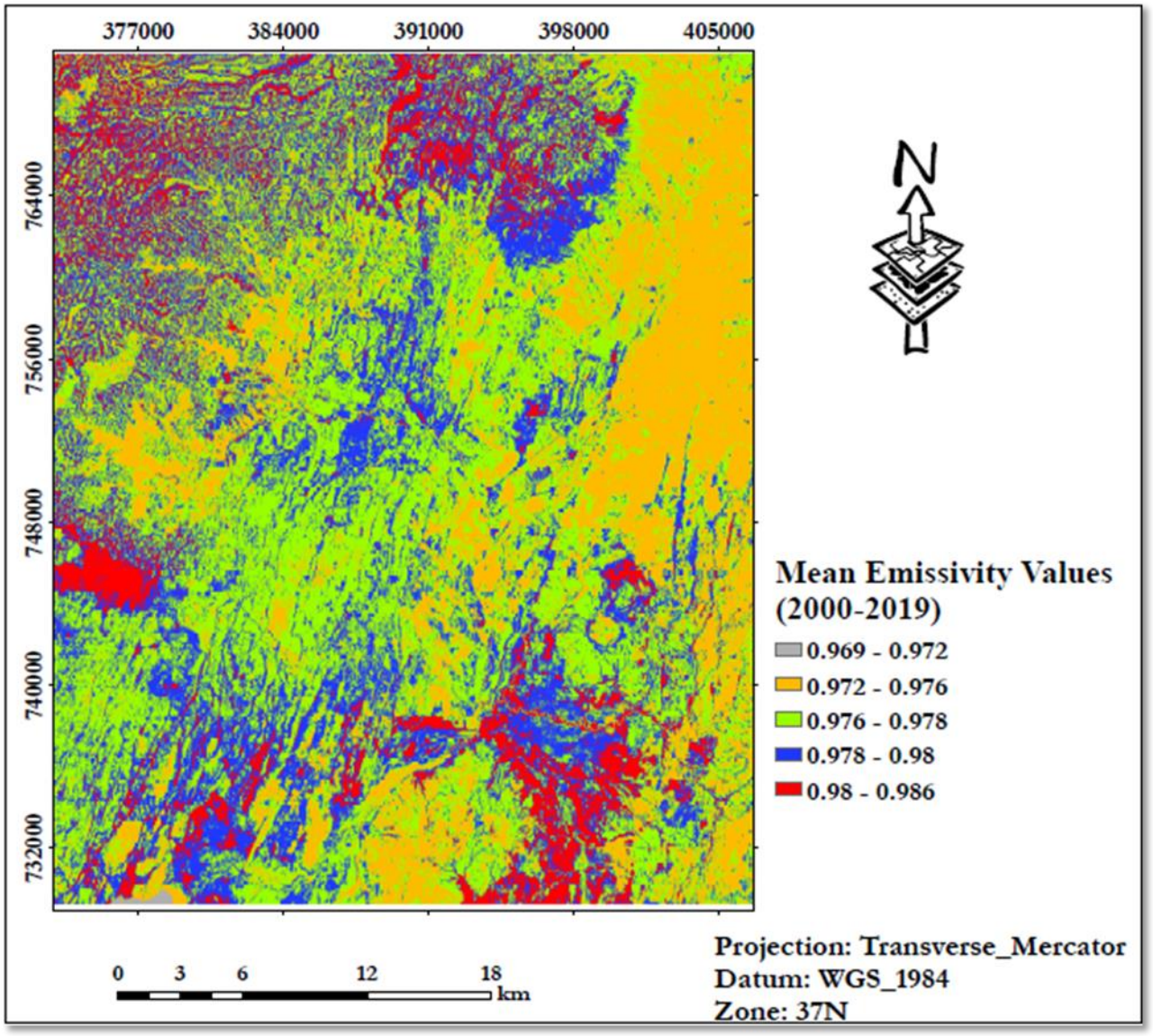

Figure 4. 5*Cell statistics (Mean) of the emissivity values of Northern Lake Abaya. Red portions correspond to areas having higher emissivity values.*

4.3 Brightness Temperature

Remote sensing data, Landsat imagery thermal band 6 on ETM+, band 10 and 11 on OLI/TIRS, and ASTER's band 10 to 14 needs to be converted from spectral radiance to at sensor brightness temperature. Brightness temperature is the radiance travelling upward from the top of the atmosphere. To convert spectral radiance to brightness temperature Equation (15) has been used.

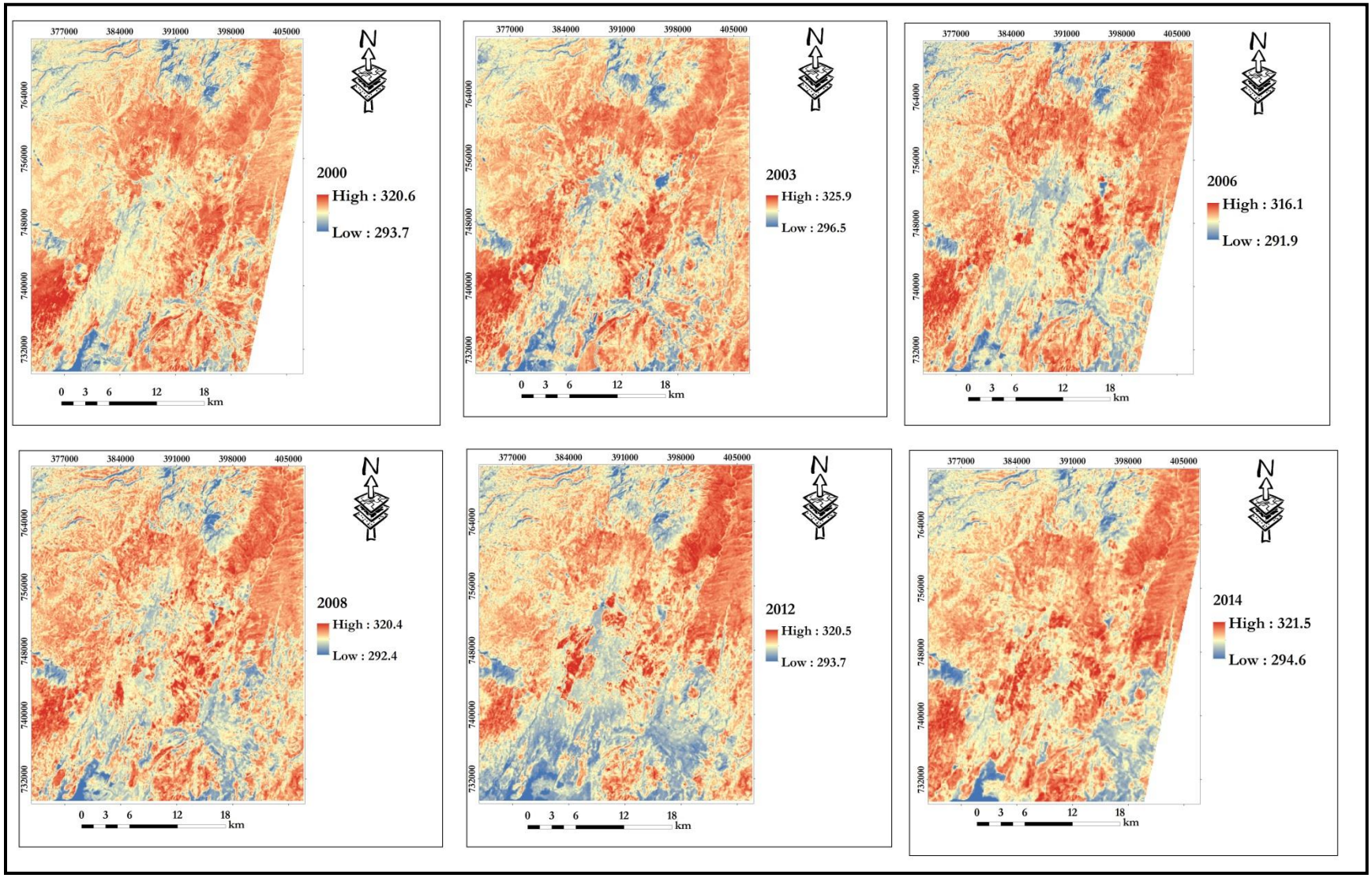

Figure4.6 Brightness Temperature maps for the year 2000, 2003,2006,2008,2012 and 2014. (K)

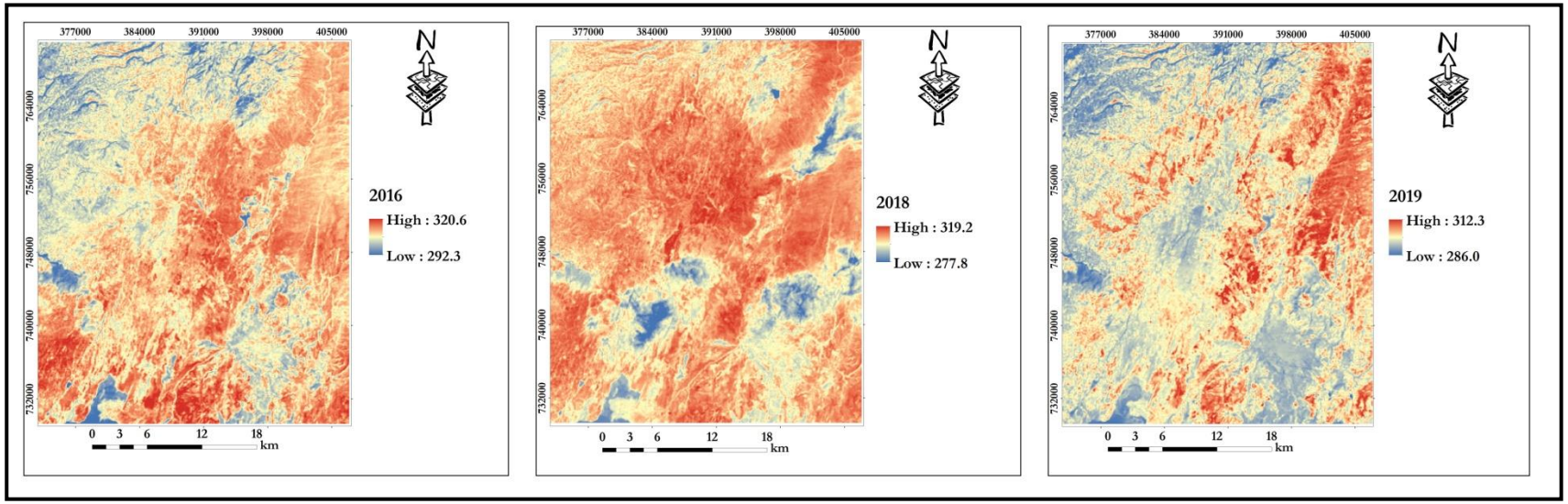

Figure 4. 6 *Brightness Temperature maps (K) of year 2016, 2018 and 2019.*

The result of at satellite temperature ranges from 293.7K to 320.6K with a mean of 310.2K and standard deviation 3.1 for the year 2000. The value is in the range of 296.5K to 325.9K with a mean of 314.3K and standard deviation 3.6 for the year 2003. In 2006 the values ranged from 291.9K to 316.1K with a mean of 306.3K and standard deviation 3. In the year 2008, the value is in the range of 292.4K to 320.4K with a mean of 309.2K and standard deviation 3.4. (Figure 4.3.2)

In 2012, the value is in the range of 293.7K to 320.5K with a mean of 307.7K and standard deviation 3.8. Highest brightness temperatures greater than 315K are traced in the NNE and central part of the study area. The value is in the range of 294.6K to 321.5K with a mean of 307.6K and standard deviation 3 in 2014; 292.3K to 320.6K with a mean of 307.3K and standard deviation of 3.4 on 2016; 277.8K to 319.2K with a mean of 307.3K and standard deviation of 4.4 in 2018 and from 286.0K to 312.3K with a mean of 301.3K and standard deviation of 2.7 in the year 2019 (Table 4.3.1).

Table 4.3.1 Maximum and minimum Brightness Temperature value of the study area

Year	Standard Deviation	Mean Value	Maximum Value	Minimum Value
2000	3.1	310.2	320.6	293.7
2003	3.6	314.3	325.9	296.5
2006	3.0	306.3	316.1	291.9
2008	3.4	309.2	320.4	292.4
2012	3.8	307.7	320.5	293.7
2014	3.0	307.6	321.5	294.6
2016	3.4	307.3	320.6	292.3
2018	4.4	307.3	319.2	277.8
2019	2.7	301.3	312.3	286

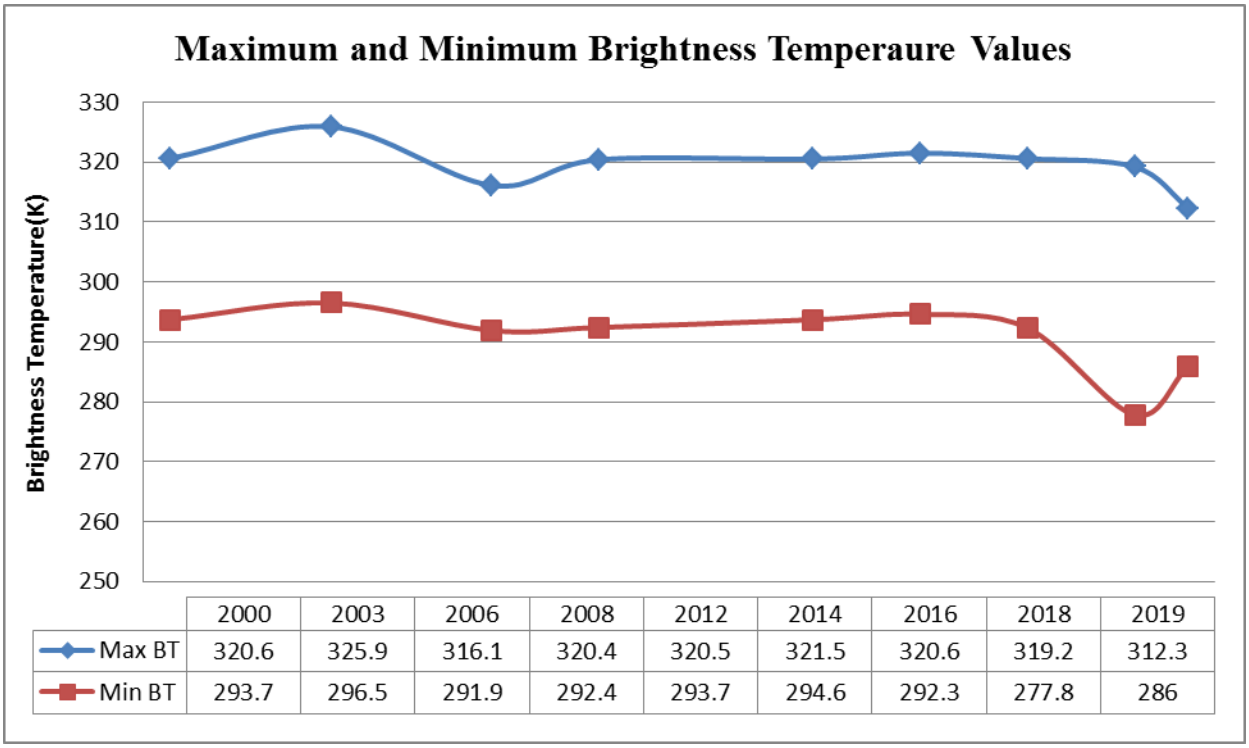

Figure 4. 7 *Maximum and minimum Brightness Temperature values of Northern Abaya area.*

The highest BT is recorded in the year 2003 having a value close to 326 K. The fact that the image has been taken in a summer season in which abundant sunlight is available contributed a lot for the highest BT values. On the other hand, the lowest BT value of 312K is recorded in

2019. The image has been taken in December. Most part of the study area has been covered with vegetation in that particular year.

Table 4.3.2 Maximum, Minimum and change in Brightness Temperature values of the study area (2000-2019).

Year	Maximum Value	Minimum Value	Max ΔT(K)	Min ΔT(K)
2000	320.9	293.4	-5.0	-3.1
2003	325.9	296.5	9.8	4.9
2006	316.1	291.7	-4.3	-0.8
2008	320.4	292.4	-0.2	-1.3
2012	320.6	293.8	-4.7	-0.4
2014	325.2	294.2	4.6	1.8
2016	320.6	292.3	1.3	14.5
2018	319.3	277.9	6.9	-8.2
2019	312.4	286.1	8.5	7.3

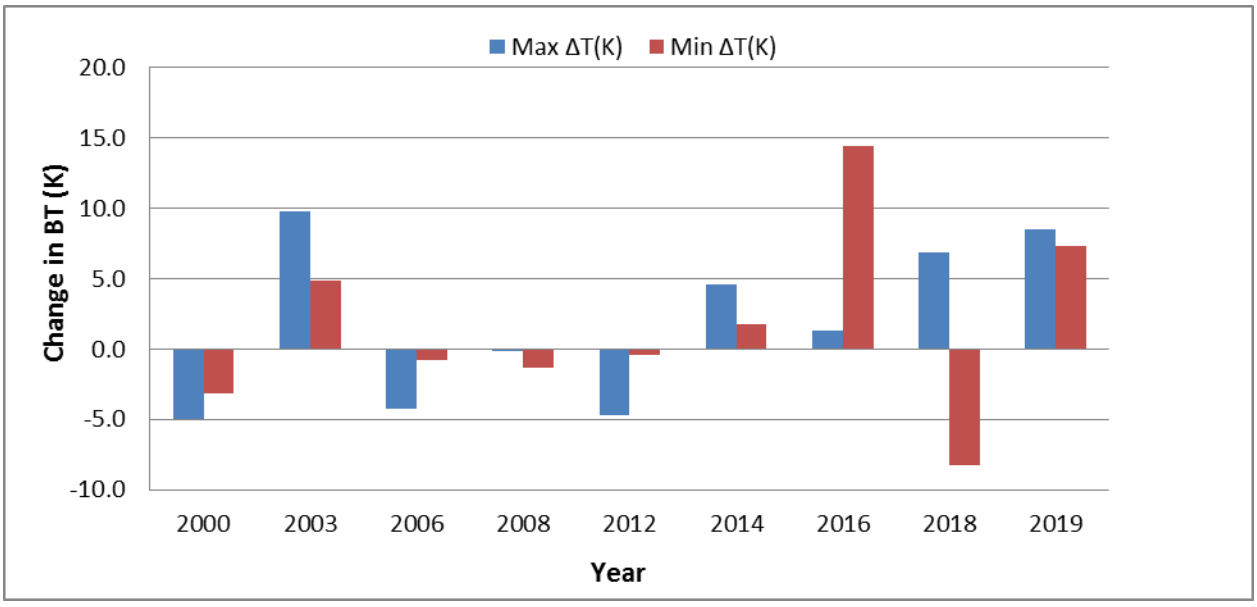

Figure 4. 8 *Change in Brightness Temperature*

4.4 Land surface Temperature

Figure 4.4.1 and 4.4.2 are generated from the emissivity and brightness temperature values of the thermal bands for each year. The LST values are in the range of 283.1K to 336.2K. Areas

appearing red on the map indicate land features having higher LST. Those appearing blue have lower LST values. The highest LST values are observed in the NNE, SSW and SE part of the study area. The North eastern part which is mainly covered by the lacustrine sediments and water lain pumice deposits show the highest LST values throughout the given time frame. Highly elevated regions with immense vegetation cover show lower values of LST in the study area.

In the year 2000 the LST value is in the range of 321.6K to 294.56K with a mean value of 311.26K and standard deviation of 3.2. In 2003 the value is in the range of 336.26K to 297.2K with a mean value of 320.1 and standard deviation of 5.3. In 2006 the value is in the range of 317 and 292.8K with a mean value of 307 and standard deviation 3.1. In 2008, the temperature value varies from 328.6 to 293 with a mean value of 313.5 and standard deviation of 4.6. In 2012, the LST is in the range of 327.9 and 294.6 with a mean value of 311.2 and standard deviation 5.1.

Table 4.4 presents the maximum, minimum and mean values of derived LSTs for the Northern Lake Abaya Area.

Year	Maximum LST (K)	Minimum LST (K)	Mean LST(K)	Standard deviation
2000	321.6	294.5	311.2	3.2
2003	336.2	297.2	320.1	5.3
2006	317.0	292.8	307.0	3.1
2008	328.6	293.0	313.5	4.6
2012	327.9	294.6	311.2	5.1
2014	322.6	295.5	308.6	3.1
2016	328.0	292.8	311.4	4.8
2018	323.6	283.1	311.1	4.9
2019	317.5	290.2	303.1	3.7

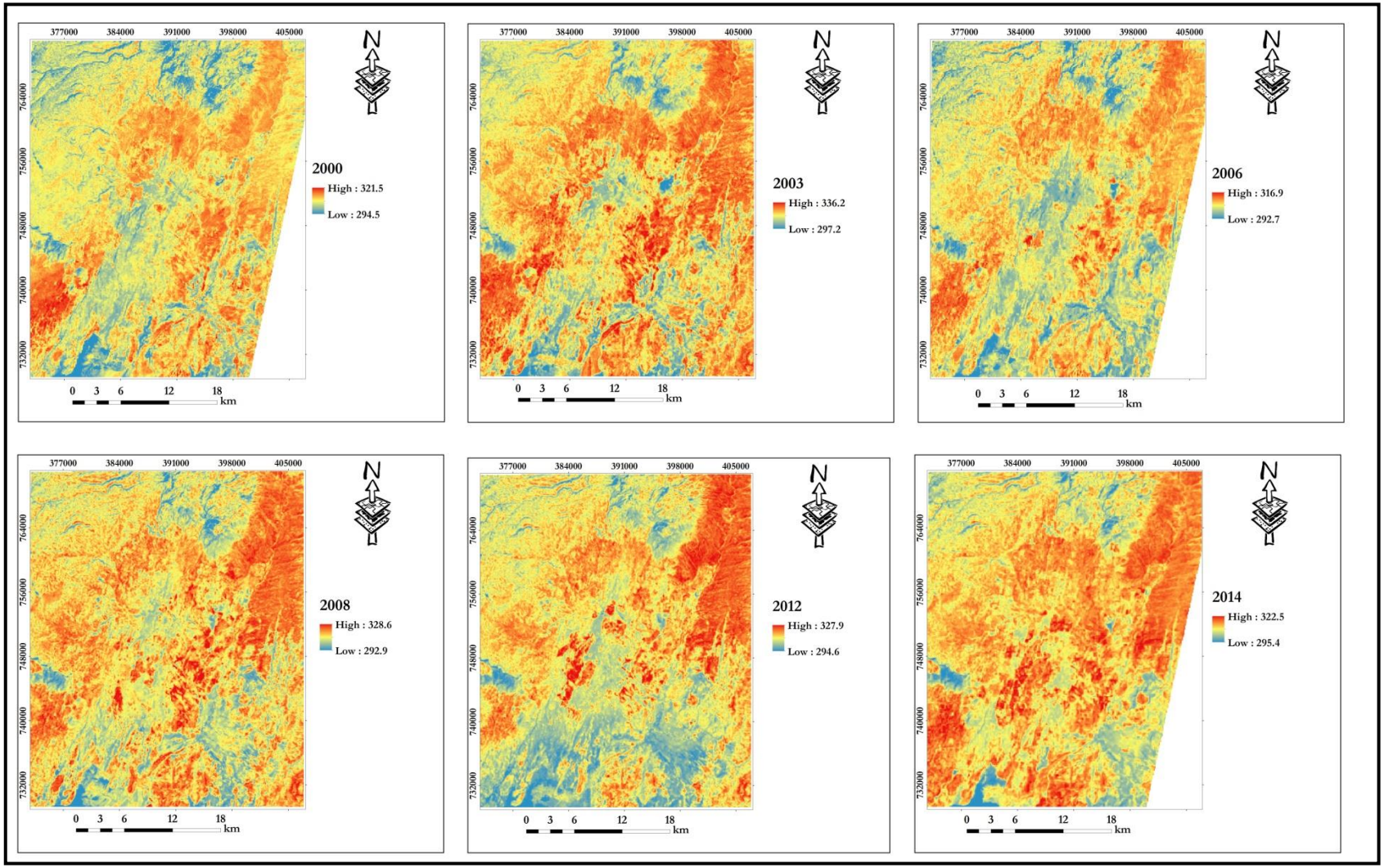

Figure 4.9 1LST values of Lake Abaya for the year 2000-2014. (K)

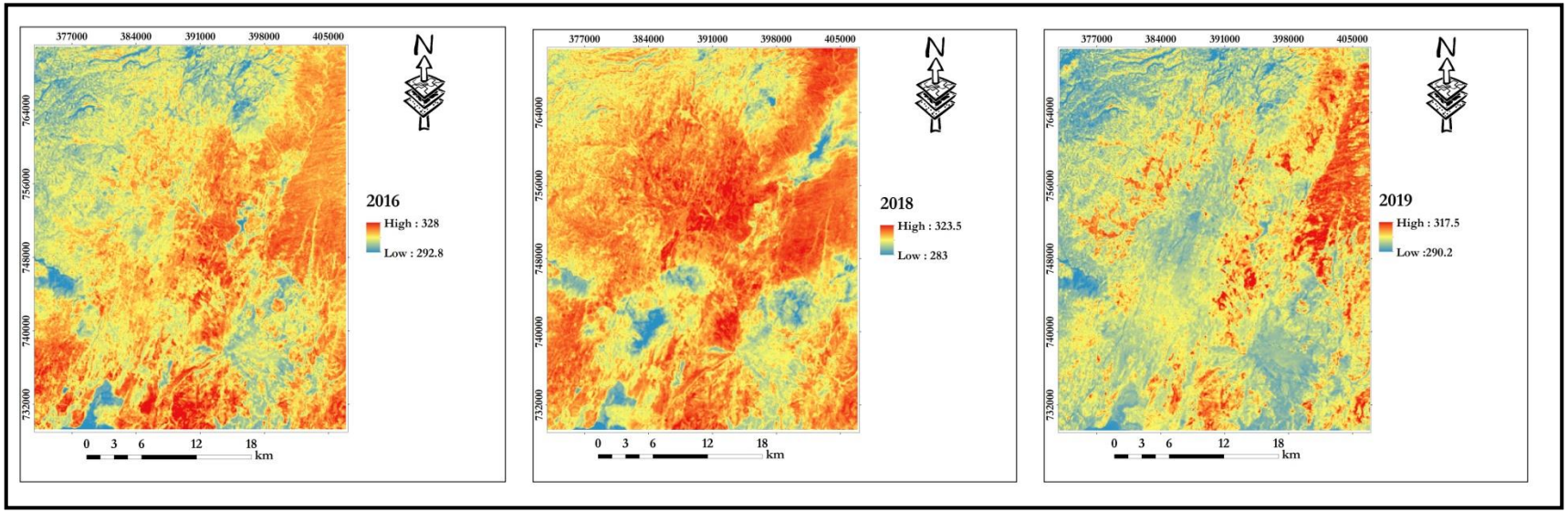

Figure 4. 9 *LST values of Lake Abaya for the year 2016-2019(K)*

In 2014, the value is in the range of 322.6 and 295.5K with a mean value of 308.6 and standard deviation of 3.1. The LST values are in the range of 328 to 292.8K with a mean value of 311.4K and standard deviation 4.8 in 2016. In 2018, the value is in the range of 323.6K and 283.1K with a mean value of 311.1K and standard deviation 4.9. The LST value is in the range of 317.5 to 290.2K with a mean value of 303.1K and standard deviation of 3.7.

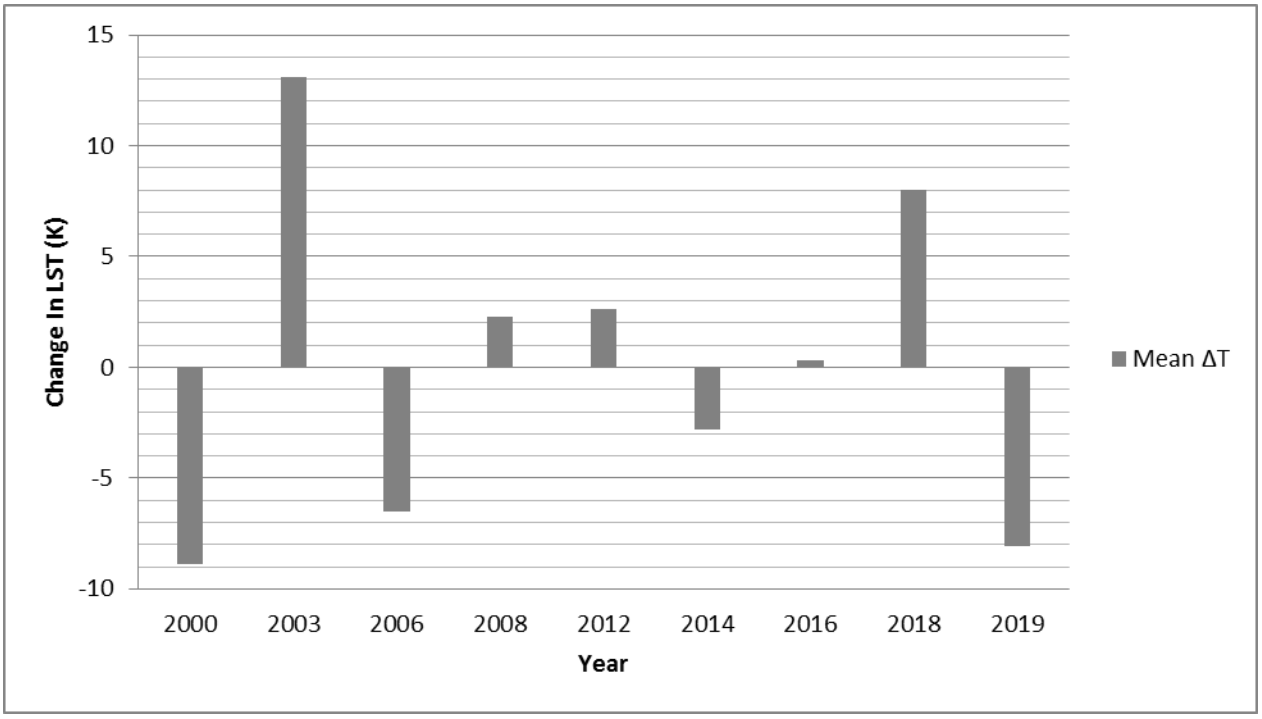

Figure 4. 10 *Change in LST values of the Northern Lake Abaya Area (2000-2019).*

4.5 Geothermal Anomaly detection Using Remote Sensing

LST anomaly is a key indicator of geothermal areas in TIR remotely sensed imagery. It can give an insight to locations of surface heat manifestations having a geothermal potential. Areas with larger LST values than the background are considered to be anomalous. Qin et al, 2011 and Yosef Darge et al., 2019 were able to identify four and nine anomalous areas with geothermal potential in Tengchong, china and Tulu Moye geothermal prospect Ethiopia, respectively. The mode value was used as a background value in both cases. Accordingly, the LST value next to the mode for each year was considered to be the background value in the present thesis. Artificial features like towns and built ups have a tendency to have greater emitted radiance recorded by a sensor and they might be considered anomalous areas with a geothermal potential, misleading the analyst. Therefore, in order to reduce the urban effect a 1000m buffer from built up areas has been applied. Areas that fall in to the buffer are considered to have a false anomaly.

Table 4.5 List of mode values taken as a background for each year

Year	Mode Value(K)	Background Value (K)
2000	311	312
2003	321	322
2006	307	308
2008	314	315
2012	311	312
2014	308	309
2016	313	314
2018	312	313
2019	301	302

The mode value for the year 2000 was 311K. Around thirteen areas having LST values 3 to 7K greater than the background value have been traced in the North eastern and south western part of the study area. The Dimtu well, the Bilbo 1 fumaroles, Bilbo 1 red boiling pool, Tobacco 1

and Bolosho vasca bubbling pool, Metincho and North Abaya thermal springs together with the Maze well are among the identified anomalous areas in that particular year(Figure 4.5.1)

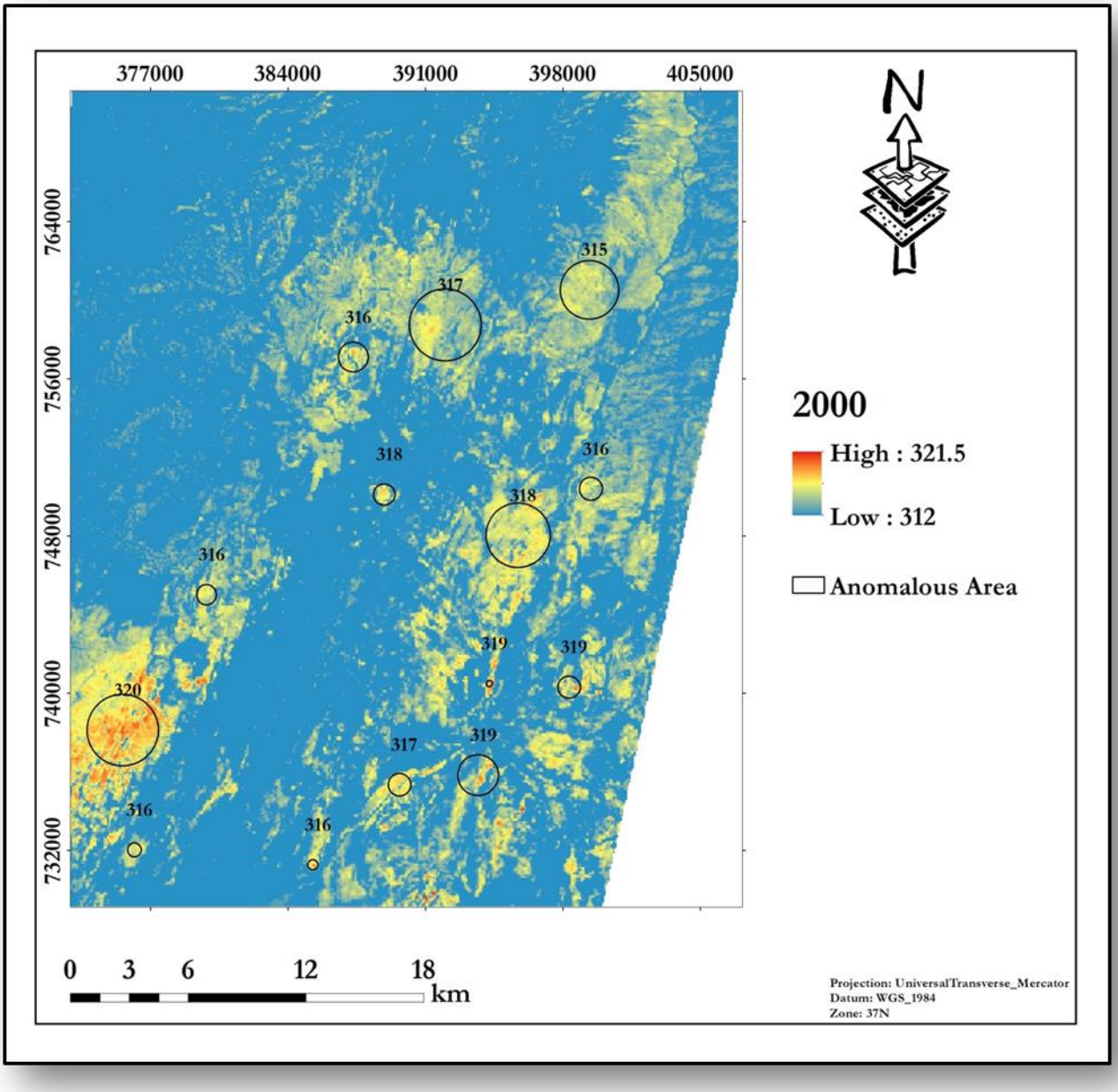

Figure 4. 11 Identified Anomalous areas for the year 2000

Table 4.6 List of Derived LST values and MODIS LST product of the hydrothermal manifestations near the Lake Abaya area for the year 2000.

Name	Type	2000 Derived LST (K)	MODIS LST Product (K)	Derived LST-MODIS LST product	
Biilate	Hot Spring	305.4	303.71	1.7	
Dimtu	Well	314.7	303.00	11.7	
Bilbo 1	Fumaroles	314.5	301.87	12.6	
Bilbo Red boiling pool	Boiling pool	314.74	301.87	12.9	
Tobacco 1	Bubbling pool	314.99	302.77	12.2	
Tobacco 2	Thermal spring	311.71	302.76	8.9	
Tobacco 4	Thermal spring	309.14	302.76	6.4	
Tobacco 5	Thermal spring	309.16	302.76	6.4	
Bolocho vasca	Bubbling pool	314.00	302.87	11.1	
Bolosho 2	Boiling pool	312.71	303.67	9.0	
Hako	Steam vent	309.41	302.66	6.8	
Metincho	Thermal spring	314.49	304.93	9.6	
Abaya	Hot Spring	308.63	306.19	2.4	
North Abaya	Bubbling pool	310.94	300.78	10.2	
North Abaya Spring	Thermal spring	314.49	300.58	13.9	
Maze well	Well	317.94	304.22	13.7	
North Abaya Fumaroles Field 7	Fumaroles	312.99	301.00	12.0	
North Abaya Fumaroles Field 9	Fumaroles	312.99	301.00	12.0	
Boramitta	Bubbling pool	311.98	300.39	11.6	
				Correlation	0.15

The mode value for the year 2003 was 321K, fifteen areas with LST values 4 to 11K higher than the background has been identified. The north eastern and south western part of the study area shows the highest LST values close to 330K. The Dimtu well, Bilbo boiling pool, Bilbo 1thermal spring, Metincho hot springs and Maze well are among the identified anomalous areas with

geothermal potential. Nineteen known anomalous areas from the geological Survey and previous literatures has been collected as a sample to be tested against the derived LSTs as shown in figure 4.5.2.

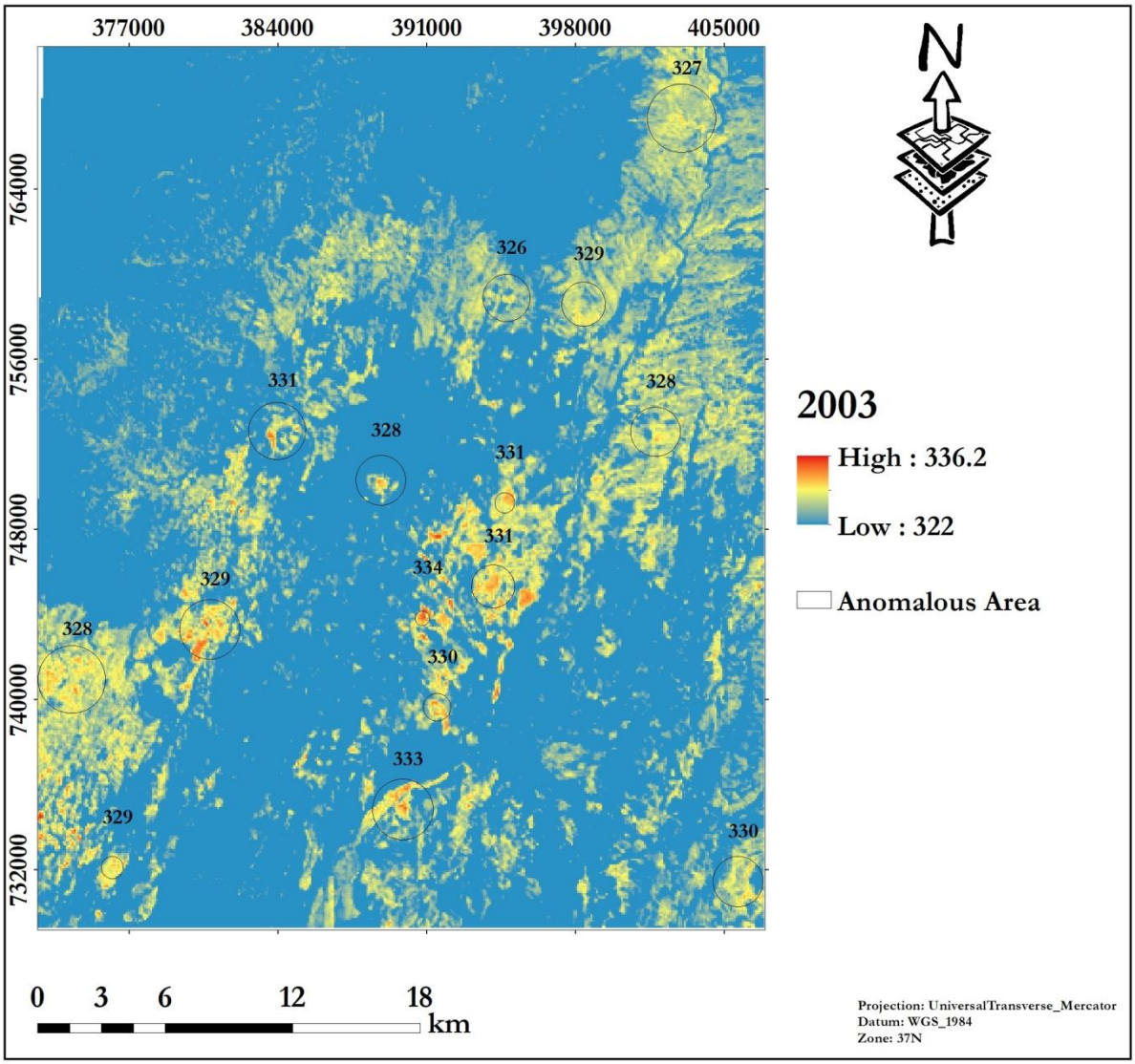

Figure 4. 12 Identified Anomalous areas for the year 2003.

LST values of those points have been validated with ASTER level 2 Surface kinetic Temperature data products Table 4.7.

Table 4.7 List of Derived LST values and AST_ product of the hydrothermal manifestations near the Lake Abaya area for the year 2003

Name	Type	2003 Derived LST (K)	AST LST Product (K)	Derived LST-AST_08 LST product
Biilate	Hot Spring	316.28	316.80	0.5
Dimtu	Well	330.28	326.60	3.7
Bilbo 1	Fumaroles	327.58	328.40	0.8
Bilbo Red boiling pool	Boiling pool	329.20	329.00	0.2
Tobacco 1	Bubbling pool	319.88	321.70	1.8
Tobacco 2	Thermal spring	322.62	325.50	2.9
Tobacco 4	Thermal spring	318.98	320.70	1.7
Tobacco 5	Thermal spring	321.00	322.90	1.9
Bolocho vasca	Bubbling pool	331.69	327.20	4.5
Bolosho 2	Boiling pool	319.08	324.50	5.4
Hako	Steam vent	320.32	314.90	5.4
Metincho	Thermal spring	325.12	326.90	1.8
Abaya	Hot Spring	317.64	319.10	1.5
North Abaya	Bubbling pool	319.97	321.00	1.0
North Abaya Spring	Thermal spring	321.87	326.70	4.8
Maze well	Well	324.86	328.30	3.4
North Abaya Fumaroles Field 7	Fumaroles	319.38	322.10	2.7
North Abaya Fumaroles Field 9	Fumaroles	321.51	322.00	0.5
Boramitta	Bubbling	316.47	321.10	4.6

	pool				
				Correlation	0.77

The mode value for the year 2006 was 307K. Areas having LST values of 4 to 8 K greater than the background have been identified in the North eastern, central and south western parts of the study area which is mainly covered with the Abela fissural basalt (Qb1), lacustrine sediment (Ql1/Qp1), and recent basalt flows and scoria cones (Qb2).

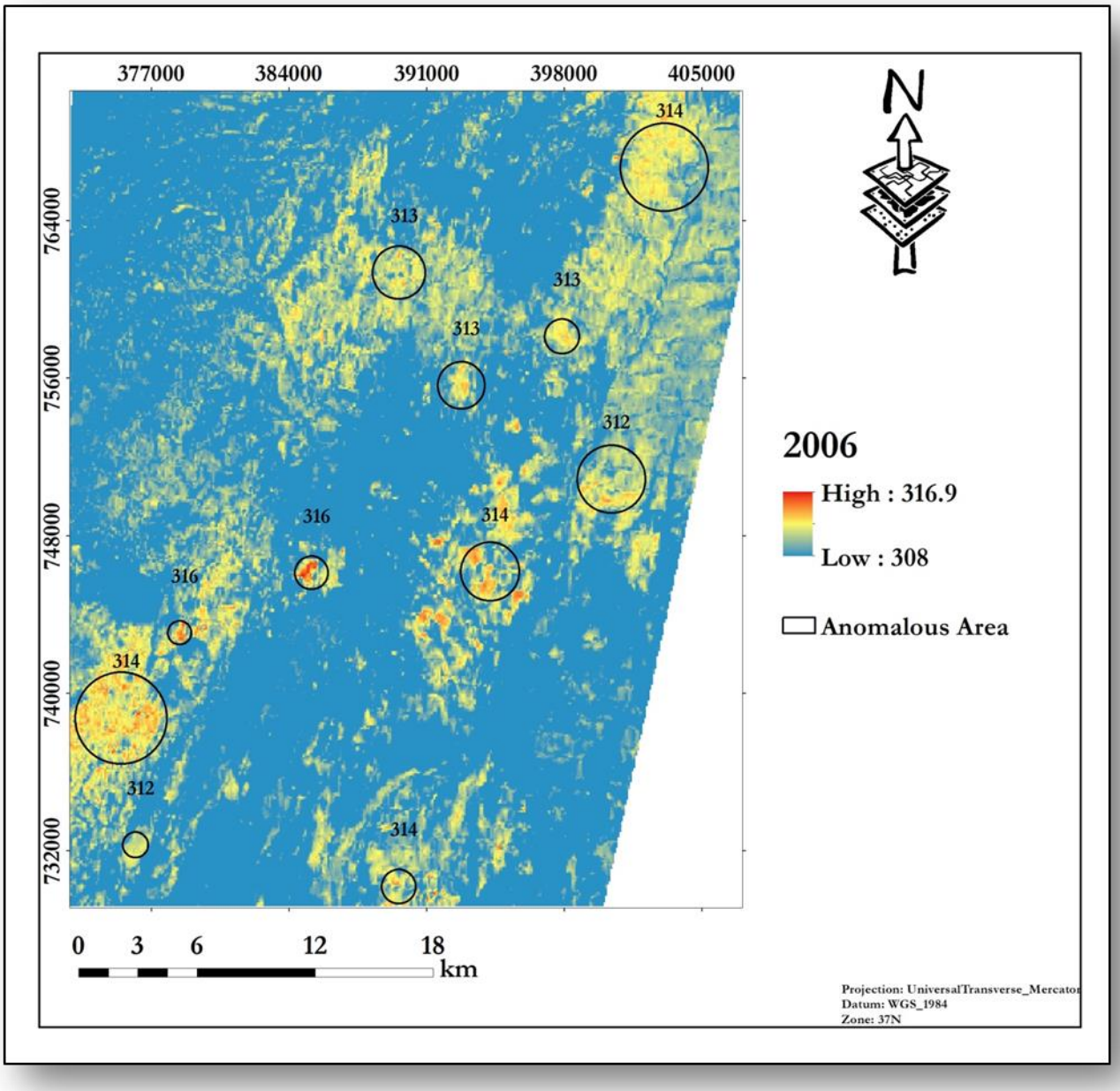

Figure 4. 13 Identified Anomalous areas for the year 2006.

The Dimtu well, the Bilbo 1 fumaroles, Bilbo red boiling pool and the maze well are among the identified anomalous areas in the year 2006(Table 4.8)

Table 4.8 List of Derived LST values and MODIS LST product of the hydrothermal manifestations near the Lake Abaya area for the year 2014

Name	Type	2006 Derived LST (K)	MODIS LST Product (K)	Derived LST-MODIS LST product
Biilate	Hot Spring	301.93	301.40	0.5
Dimtu	Well	310.96	300.17	10.8
ssBilbo 1	Fumaroles	311.22	298.47	12.8
Bilbo Red boiling pool	Boiling pool	311.72	298.47	13.3
Tobacco 1	Bubbling pool	308.89	No data	-
Tobacco 2	Thermal spring	308.90	No data	-
Tobacco 4	Thermal spring	306.53	No data	-
Tobacco 5	Thermal spring	307.08	No data	-
Bolocho vasca	Bubbling pool	309.43	No data	-
Bolosho 2	Boiling pool	305.98	303.04	2.9
Hako	Steam vent	307.06	300.33	6.7
Metincho	Thermal spring	303.05	299.52	3.5
Abaya	Hot Spring	306.80	301.02	5.8
North Abaya	Bubbling pool	308.37	298.97	9.4
North Abaya Spring	Thermal spring	309.67	299.38	10.3
Maze well	Well	310.96	302.37	8.6
North Abaya Fumaroles Field 7	Fumaroles	308.63	298.58	10.1
North Abaya Fumaroles Field 9	Fumaroles	308.63	298.58	10.1
Boramitta	Bubbling pool	308.90	298.50	10.4
				Correlation

The mode value for the year 2008 is 314K, more than ten areas having a 4 to 12K LST values greater than the background have been identified. Most of the anomalous areas in the year 2003 appeared to be anomalous once again. The north eastern and central part of the study area which

is covered with the Abela Basalt (Qb1), the lacustrine sediments and pumice (Ql1/Qp1) has LST value which is around 11K greater than the mode value. Figure4. Table 4.9 presents List of Sample points and their derived LST values validated with ASTER Level 2 for the year 2008.

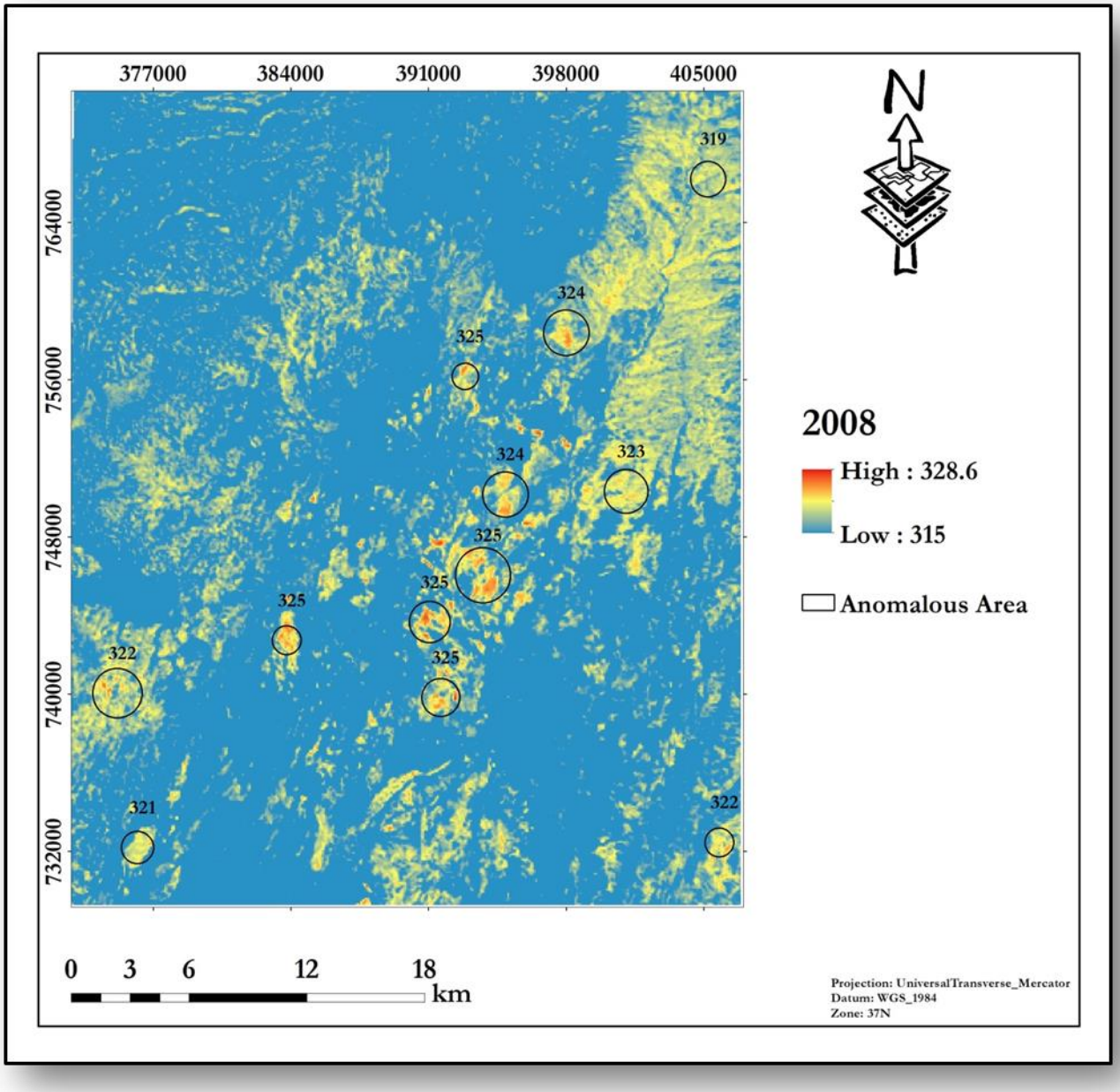

Figure 4. 14 Identified Anomalous areas for the year 2008.

The Dimtu well, Bilbo 1 Fumaroles, Bilbo Red boiling pool, the thermal springs near the Tobacco plantation and Metincho area and the Bolocho vasca bubbling pool are among the identified area with highest LST values in the year 2008.

Table 4.9 List of Derived LST values and AST_ product of the hydrothermal manifestations near the Lake Abaya area for the year 2008

Name	Type	2008 Derived LST (K)	AST LST Product (K)	Derived LST - AST_08 LST	
Biilate	Hot Spring	307.60	311.40	3.8	
Dimtu	Well	322.34	313.90	8.4	
Bilbo 1	Fumaroles	323.17	323.10	0.1	
Bilbo Red boiling pool	Boiling pool	324.19	321.40	2.8	
Tobacco 1	Bubbling pool	316.99	317.70	0.7	
Tobacco 2	Thermal spring	316.65	316.50	0.1	
Tobacco 4	Thermal spring	313.27	315.20	1.9	
Tobacco 5	Thermal spring	311.14	309.50	1.6	
Bolocho vasca	Bubbling pool	321.75	318.90	2.9	
Bolosho 2	Boiling pool	310.75	316.50	5.8	
Hako	Steam vent	310.14	305.10	5.0	
Metincho	Thermal spring	317.49	317.80	0.3	
Abaya	Hot Spring	312.70	310.40	2.3	
North Abaya	Bubbling pool	315.80	314.30	1.5	
North Abaya Spring	Thermal spring	315.18	314.00	1.2	
Maze well	Well	311.69	315.10	3.4	
North Abaya Fumaroles Field 7	Fumaroles	312.08	312.50	0.4	
North Abaya Fumaroles Field 9	Fumaroles	313.71	308.00	5.7	
Boramitta	Bubbling pool	309.00	313.50	4.5	
				Correlation	0.71

In the year 2012, the mode value was 311K. Areas that have greater LST values have been traced on the NNE (near the Dimtu city) and NE (near the tobacco plantation) part of the study area. Values close to 322K have been identified in those particular areas.

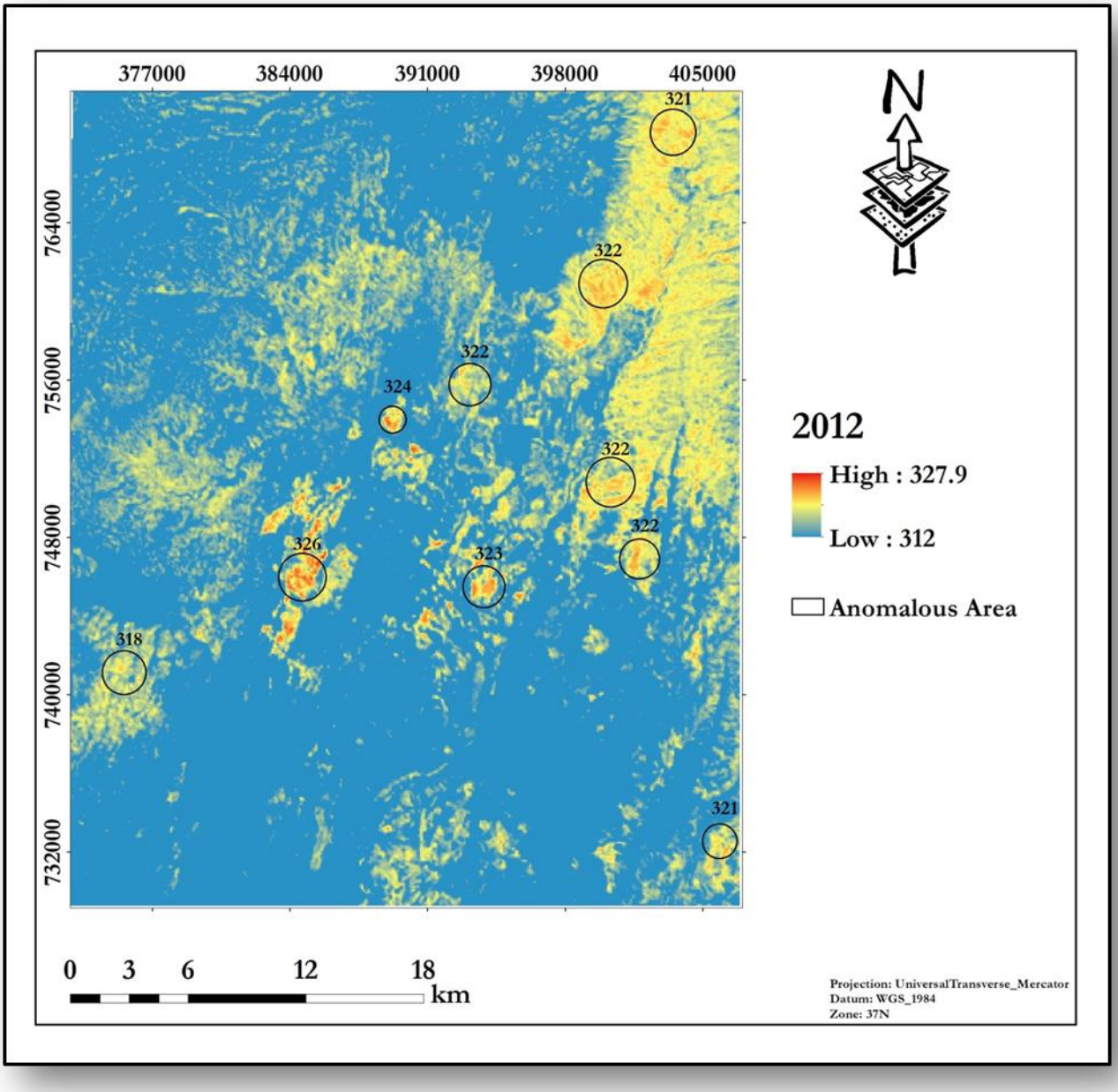

Figure 4. 15 Identified Anomalous areas for the year 2012.

The Anka Bilbo fumaroles and bubbling pools together with the Dimtu well have been identified as anomalous areas once again. In addition to that the Tobacco 2 thermal spring and the Bolosho vasca bubbling pools have also been determined to be anomalous in the year 2012. (Table 4.10)

Table 4.10 List of Derived LST values and AST_ product of the hydrothermal manifestations near the Lake Abaya area for the year 2012.

Name	Type	2012 Derived LST (K)	AST LST Product (K)	Derived LST - AST_08 LST	
Biilate	Hot Spring	309.38	309.30	0.1	
Dimtu	Well	319.57	314.80	4.8	
Bilbo 1	Fumaroles	320.07	321.50	1.4	
Bilbo Red boiling pool	Boiling pool	318.51	314.90	3.6	
Tobacco 1	Bubbling pool	311.26	310.50	0.8	
Tobacco 2	Thermal spring	315.88	317.40	1.5	
Tobacco 4	Thermal spring	312.52	315.50	3.0	
Tobacco 5	Thermal spring	312.29	314.10	1.8	
Bolocho vasca	Bubbling pool	315.73	314.90	0.8	
Bolosho 2	Boiling pool	306.15	312.80	6.7	
Hako	Steam vent	305.81	304.20	1.6	
Metincho	Thermal spring	312.88	315.70	2.8	
Abaya	Hot Spring	306.99	305.60	1.4	
North Abaya	Bubbling pool	310.81	312.10	1.3	
North Abaya Spring	Thermal spring	308.01	307.70	0.3	
Maze well	Well	303.78	309.50	5.7	
North Abaya Fumaroles Field 7	Fumaroles	307.09	307.70	0.6	
North Abaya Fumaroles Field 9	Fumaroles	307.99	306.70	1.3	
Boramitta	Bubbling pool	305.16	310.50	5.3	
				Correlation	0.8

The mode value for the year 2014 was 308K. Areas with LST values as high as 322K has been traced in the south western part of the study area. The Bolosho vasca and Bilbo red boiling pool,

Tobacco 1 bubbling pool, and the Maze well are among the identified anomalous areas with a value of 312. 5K, 311.3K, 311K and 312.6K respectively (Figure 4.5.6)

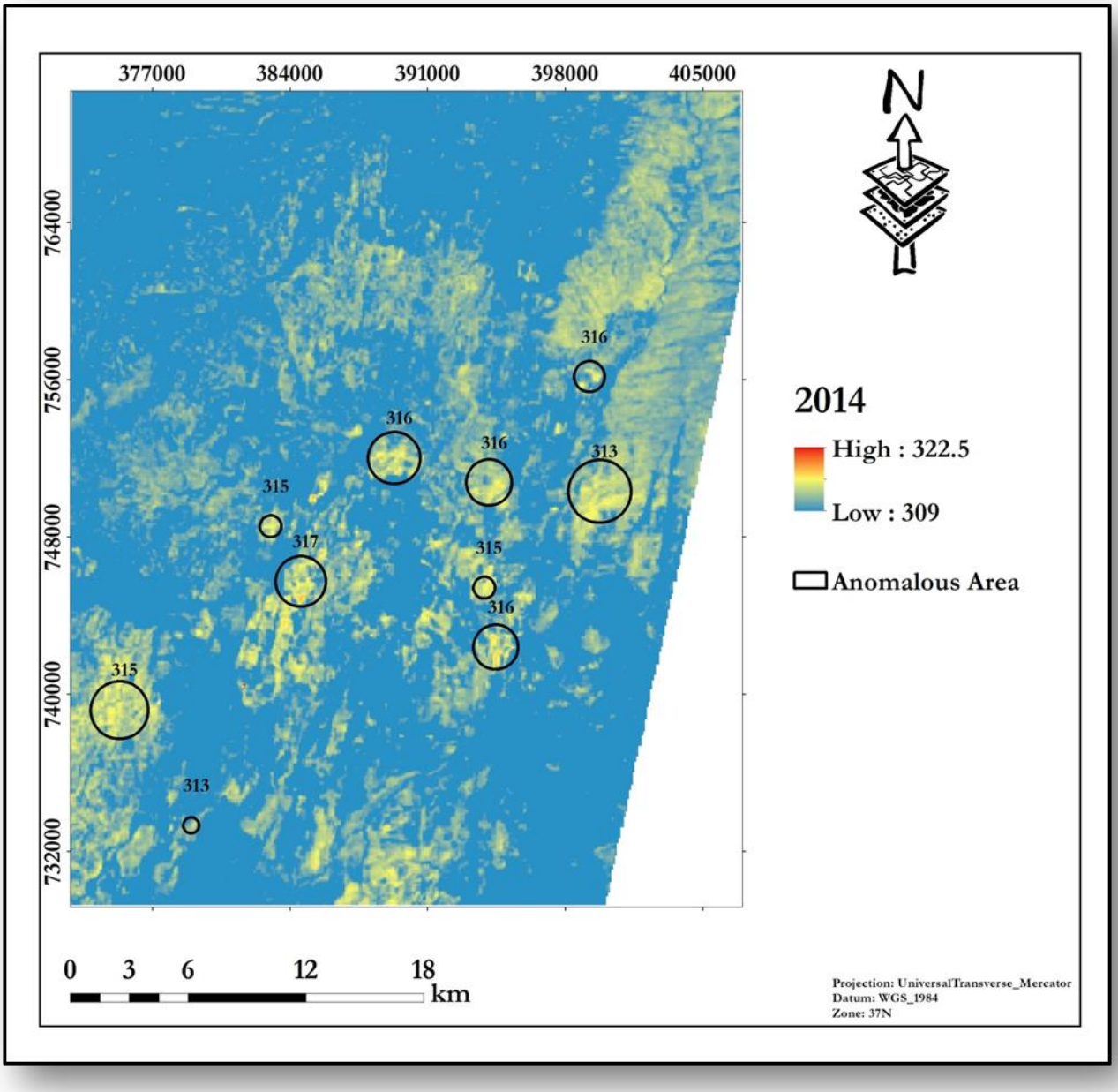

Figure 4. 16 Identified Anomalous areas for the year 2014.

Table 4.11 List of Derived LST values and MODIS LST product of the hydrothermal manifestations near the Lake Abaya area for the year 2014

Name	Type	2014Derived LST (K)	MODIS LST Product (K)	Derived LST - AST_08 LST	
Biilate	Hot Spring	303.73	303.49	0.2	
Dimtu	Well	310.06	302.61	7.4	
Bilbo 1	Fumaroles	310.54	301.02	9.5	
Bilbo Red boiling pool	Boiling pool	311.35	301.02	10.3	
Tobacco 1	Bubbling pool	311.00	302.10	8.9	
Tobacco 2	Thermal spring	309.69	301.98	7.7	
Tobacco 4	Thermal spring	309.11	301.98	7.1	
Tobacco 5	Thermal spring	307.93	301.98	5.9	
Bolocho vasca	Bubbling pool	312.57	303.16	9.4	
Bolosho 2	Boiling pool	308.92	303.91	5.0	
Hako	Steam vent	305.86	303.14	2.7	
Metincho	Thermal spring	309.22	303.09	6.1	
Abaya	Hot Spring	307.34	300.79	6.5	
North Abaya	Bubbling pool	309.71	298.78	10.9	
North Abaya Spring	Thermal spring	310.59	299.54	11.1	
Maze well	Well	312.59	304.80	7.8	
North Abaya Fumaroles Field 7	Fumaroles	309.17	300.58	8.6	
North Abaya Fumaroles Field 9	Fumaroles	309.17	300.58	8.6	
Boramitta	Bubbling pool	308.04	299.80	8.2	
				Correlation	-0.02

In the year 2016 the mode value was 313K. Around 10 areas with LST values 4 to 14K higher than the background have been identified. Areas found in the southern part of the study area show the highest LST values greater than 320K.

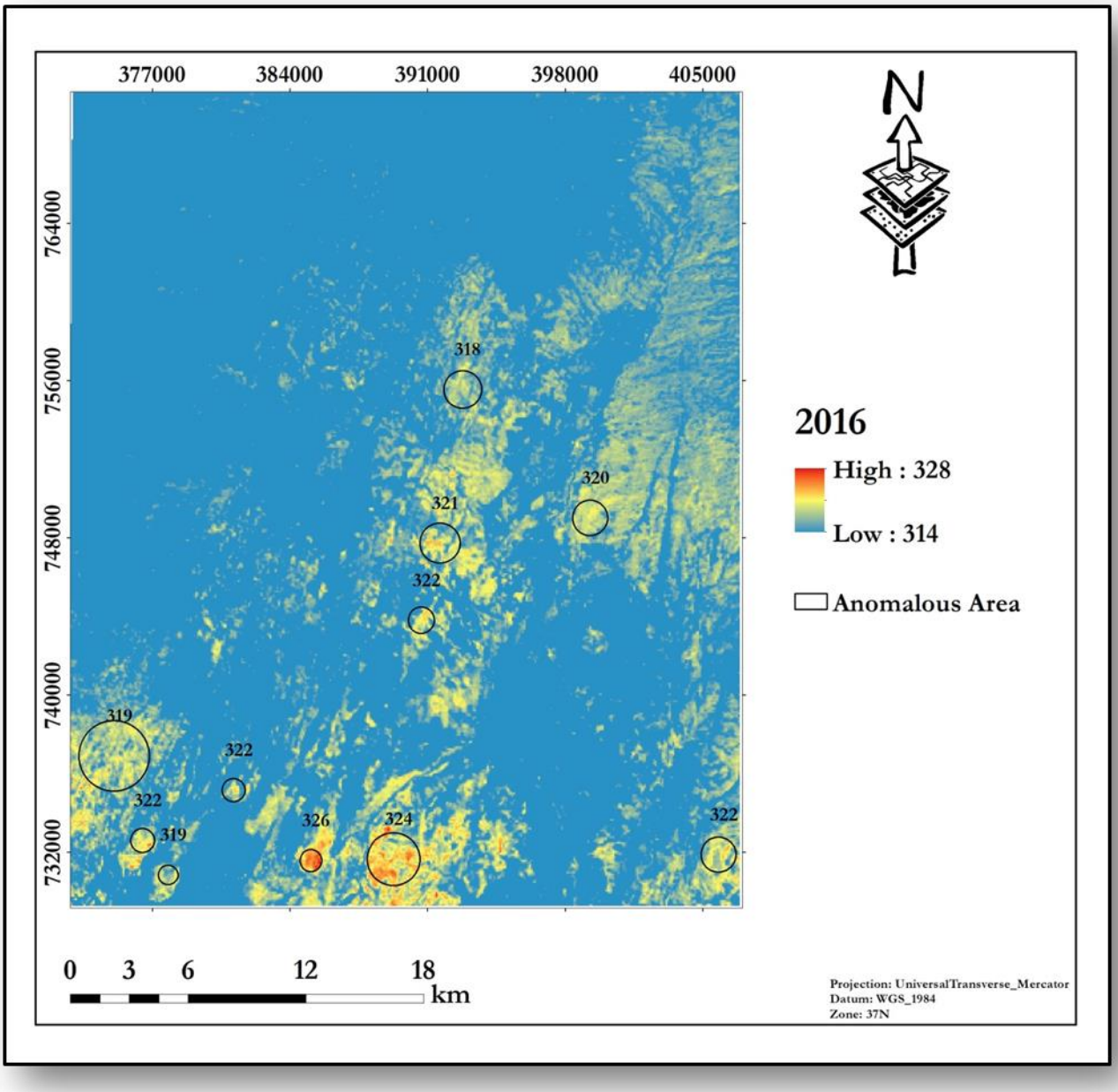

Figure 4. 17 Identified Anomalous areas for the year 2016.

The Bolosho Vasca bubbling pool, the Bilbo 1 fumaroles, the Dimtu well and the Bilbo red boiling pools are among the identified anomalous areas with LST value of 317.6K, 319K, 320.65K and 315K respectively. (Table 4.12)

Table 4.12 List of Derived LST values and AST_ product of the hydrothermal manifestations near the Lake Abaya area for the year 2016.

Name	Type	2016 Derived LST (K)	AST LST Product (K)	Derived LST - AST_08 LST	
Biilate	Hot Spring	306.20	306.30	0.1	
Dimtu	Well	315.07	312.50	2.6	
Bilbo 1	Fumaroles	319.04	318.10	0.9	
Bilbo Red boiling pool	Boiling pool	320.65	318.80	1.8	
Tobacco 1	Bubbling pool	311.15	313.00	1.9	
Tobacco 2	Thermal spring	314.77	316.20	1.4	
Tobacco 4	Thermal spring	311.11	314.70	3.6	
Tobacco 5	Thermal spring	312.99	314.80	1.8	
Bolocho vasca	Bubbling pool	317.68	317.50	0.2	
Bolosho 2	Boiling pool	314.95	318.70	3.8	
Hako	Steam vent	305.37	303.80	1.6	
Metincho	Thermal spring	313.48	316.90	3.4	
Abaya	Hot Spring	312.77	313.40	0.6	
North Abaya	Bubbling pool	314.39	316.70	2.3	
North Abaya Spring	Thermal spring	314.96	317.70	2.7	
Maze well	Well	312.24	312.90	0.7	
North Abaya Fumaroles Field 7	Fumaroles	311.98	312.30	0.3	
North Abaya Fumaroles Field 9	Fumaroles	312.63	312.20	0.4	
Boramitta	Bubbling pool	310.63	316.10	5.5	
				Correlation	0.84

The mode value for the year 2018 was 312K. The NNE and central part of the study area show the highest LST values of more than 320K. The Anka Bilbo fumaroles and red boiling pool, the Tobacco 2 and 5 thermal springs together with the Bolosho 2 Boiling pool are among the identified anomalous areas.

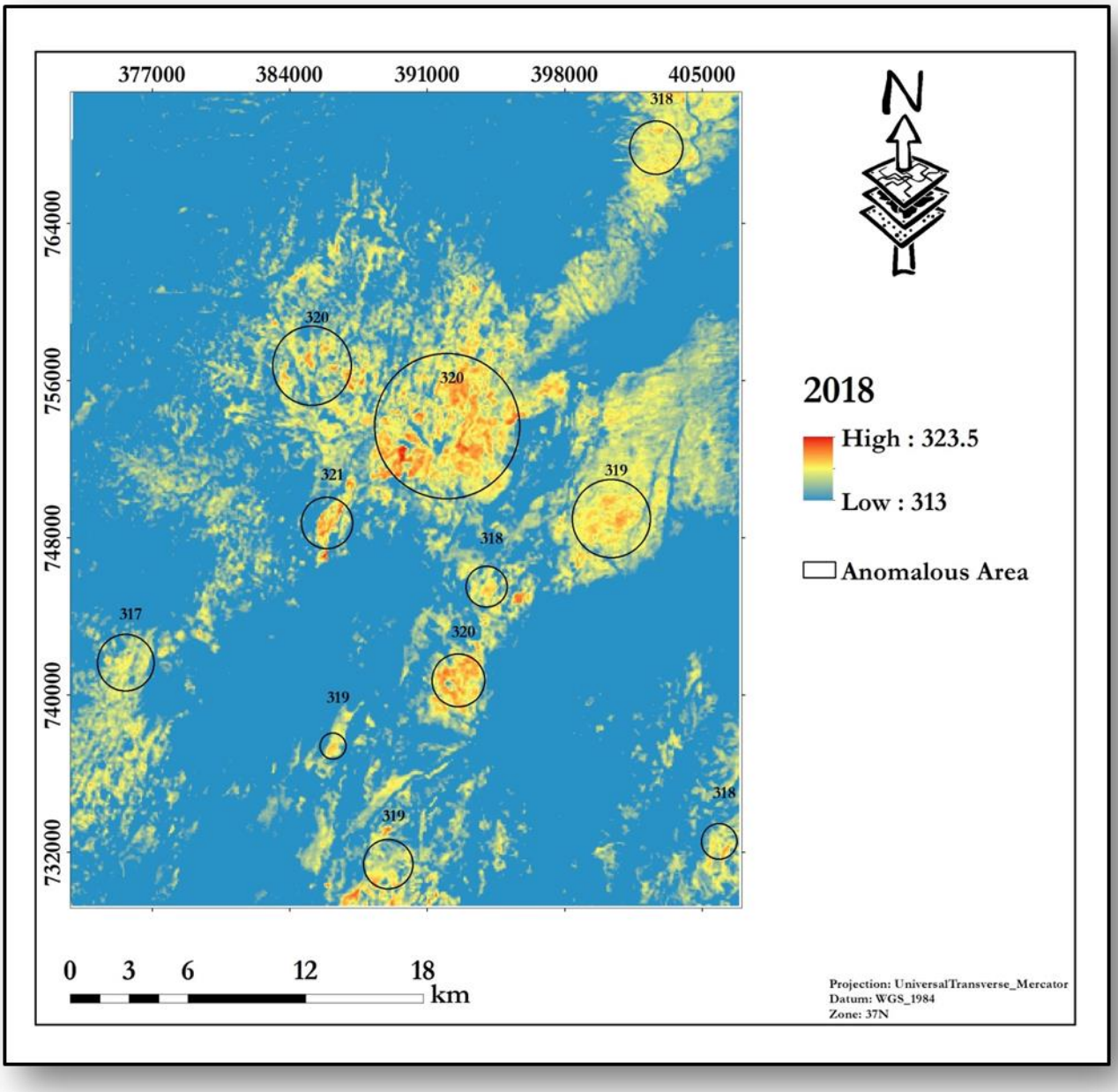

Figure 4. 18 Identified Anomalous areas for the year 2018.

Table 4.13 List of Derived LST values and AST_ product of the hydrothermal manifestations near the Lake Abaya area for the year 2018.

Name	Type	2018 Derived LST (K)	AST LST Product (K)	Derived LST - AST_08 LST	
Biilate	Hot Spring	306.75	308.10	1.4	
Dimtu	Well	313.36	312.50	0.9	
Bilbo 1	Fumaroles	319.83	320.80	1.0	
Bilbo Red boiling pool	Boiling pool	320.58	322.30	1.7	
Tobacco 1	Bubbling pool	314.42	316.10	1.7	
Tobacco 2	Thermal spring	317.03	319.20	2.2	
Tobacco 4	Thermal spring	314.04	314.00	0.0	
Tobacco 5	Thermal spring	315.35	317.40	2.0	
Bolocho vasca	Bubbling pool	313.43	314.10	0.7	
Bolosho 2	Boiling pool	315.94	319.10	3.2	
Hako	Steam vent	308.44	305.00	3.4	
Metincho	Thermal spring	314.98	313.00	2.0	
Abaya	Hot Spring	312.39	312.80	0.4	
North Abaya	Bubbling pool	312.91	309.90	3.0	
North Abaya Spring	Thermal spring	311.34	314.10	2.8	
Maze well	Well	310.30	310.80	0.5	
North Abaya Fumaroles Field 7	Fumaroles	308.60	308.30	0.3	
North Abaya Fumaroles Field 9	Fumaroles	308.13	307.60	0.5	
Boramitta	Bubbling pool	307.00	307.00	0.0	
				Correlation	0.94

The mode value for the year 2019 was 301K; higher LST values are traced in the NNE, NE and southern part of the study area. About 15 areas with LST values 8 to 15K higher than the background have been identified

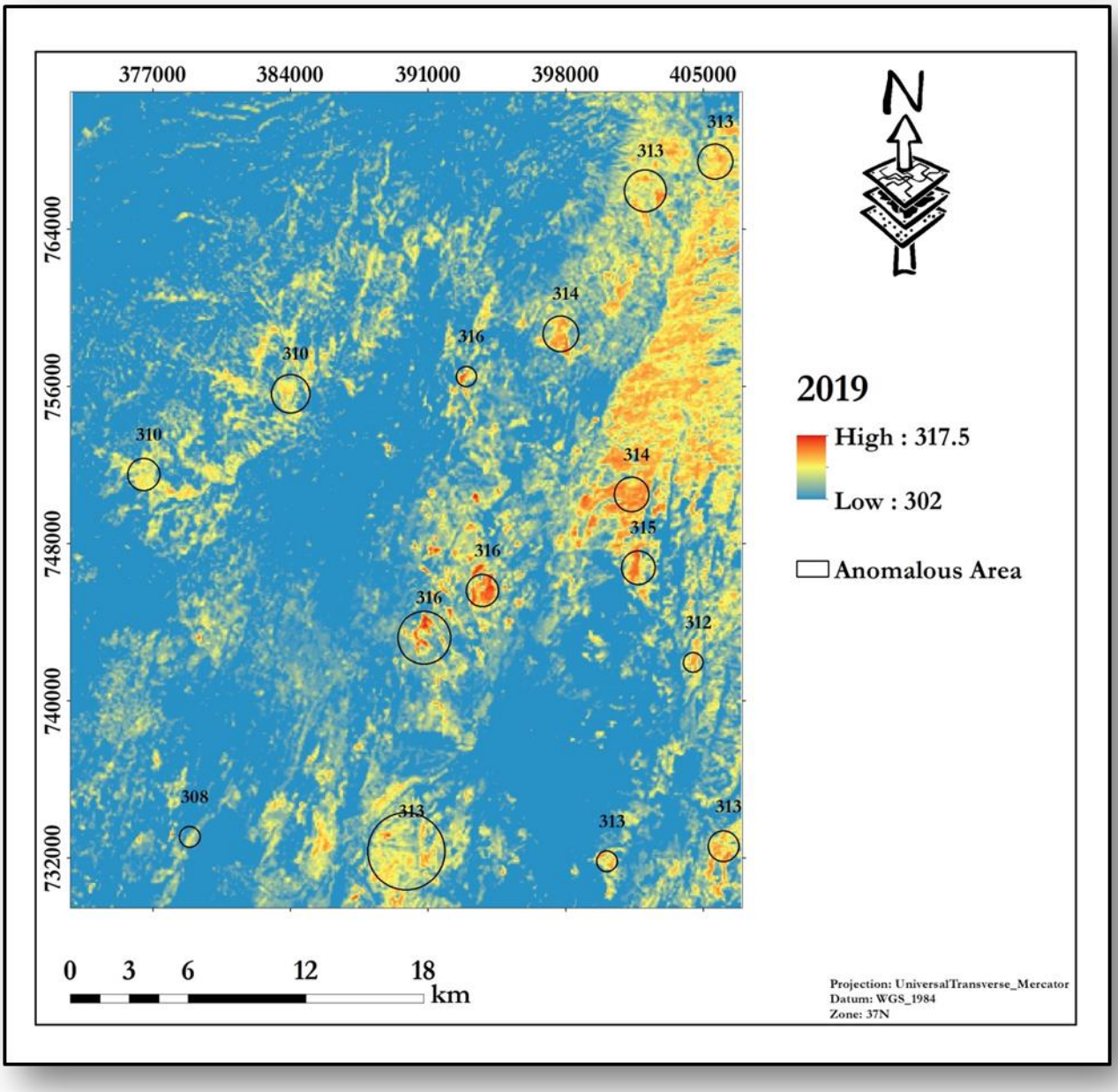

Figure 4. 19 Identified Anomalous areas for the year 2019.

Volcano sedimentary rocks, Pleistocene basalt, pumice and unwelded tuff, rhyolitic and trachytic lava flows are the major geological units associated with areas showing higher surface temperature values. The Dimtu well, Bilbo 1 fumaroles, Bilbo red and Bolosho 2 boiling pool, the thermal springs near the tobacco plantation (2, 4, 5) and metincho area, Bolocho vasca and

Tobacco 1 bubbling pool, together with the Northern Abaya fumaroles (7,9)and spring are among the anomalous area identified in that particular year. Table 4.14

Table 4.14 List of Derived LST values and AST_ product of the hydrothermal manifestations near the Lake Abaya area for the year 2019.

Name	Type	2019 Derived LST (K)	AST LST Product (K)	Derived LST - AST_08 LST
Biilate	Hot Spring	298.77	304.50	5.7
Dimtu	Well	306.04	309.00	3.0
Bilbo 1	Fumaroles	308.09	319.00	10.9
Bilbo Red boiling pool	Boiling pool	310.63	311.30	0.7
Tobacco 1	Bubbling pool	304.97	308.80	3.8
Tobacco 2	Thermal spring	307.84	313.40	5.6
Tobacco 4	Thermal spring	307.34	310.90	3.6
Tobacco 5	Thermal spring	305.28	309.80	4.5
Bolocho vasca	Bubbling pool	305.66	310.70	5.0
Bolosho 2	Boiling pool	304.54	310.60	6.1
Hako	Steam vent	300.42	303.00	2.6
Metincho	Thermal spring	305.98	314.50	8.5
Abaya	Hot Spring	301.14	306.60	5.5
North Abaya	Bubbling pool	303.23	311.50	8.3
North Abaya Spring	Thermal spring	304.48	312.60	8.1
Maze well	Well	303.19	307.40	4.2
North Abaya Fumaroles Field 7	Fumaroles	305.26	308.60	3.3
North Abaya Fumaroles Field 9	Fumaroles	306.12	308.80	2.7
Boramitta	Bubbling pool	301.65	308.60	7.0
			Correlation	0.71

The Anka Bilbo boiling pools and fumaroles, the Dimtu well and Bolosho Vasca bubbling pools appear to be anomalous more than five times. The Maze well and tobacco 1 bubbling pools were analyzed to be anomalous four times. Metincho and Tobacco 2 thermal springs appear to be

anomalous two times out of nine.(Table 4.15) The Abaya hot spring, Bilate hot springs, the Hako steam vent and Boramitta bubbling pools are among the known surface manifestations that happened to be anomalous in none of the years in the given time frame (2000-2019 in two years interval).

Table 4.15 List of the Northern Abaya Surface Manifestation and particular years they appear to be Anomalous

Name	2000	2003	2006	2008	2012	2014	2016	2018	2019
Abaya	0	0	0	0	0	0	0	0	0
Biilate	0	0	0	0	0	0	0	0	0
Bilbo 1	1	1	1	1	1	0	1	1	1
Bilbo Red boiling pool	1	1	1	1	1	1	1	1	1
Bolocho vasca	1	1	0	1	1	1	1	0	1
Bolosho 2	0	0	0	0	0	0	0	1	1
Boramitta	0	0	0	0	0	0	0	0	0
Dimtu Well	1	1	1	1	1	0	0	0	1
Hako	0	0	0	0	0	0	0	0	0
Maze well	1	1	1	0	0	1	0	0	0
Metincho	1	1	0	1	0	0	0	0	0
North Abaya	1	0	0	0	0	0	0	0	1
N.Abaya Fumarolic Field 7	0	0	0	0	0	0	0	0	1
N. Abaya Fumarolic Field 9	0	0	0	0	0	0	0	0	1
North Abaya Spring	1	0	0	0	0	0	0	0	0
Tobacco 1	1	0	0	1	0	1	0	0	1
Tobacco 2	0	0	0	0	1	0	0	1	1
Tobacco 4	0	0	0	0	0	0	0	0	1
Tobacco 5	0	0	0	0	0	0	0	1	1

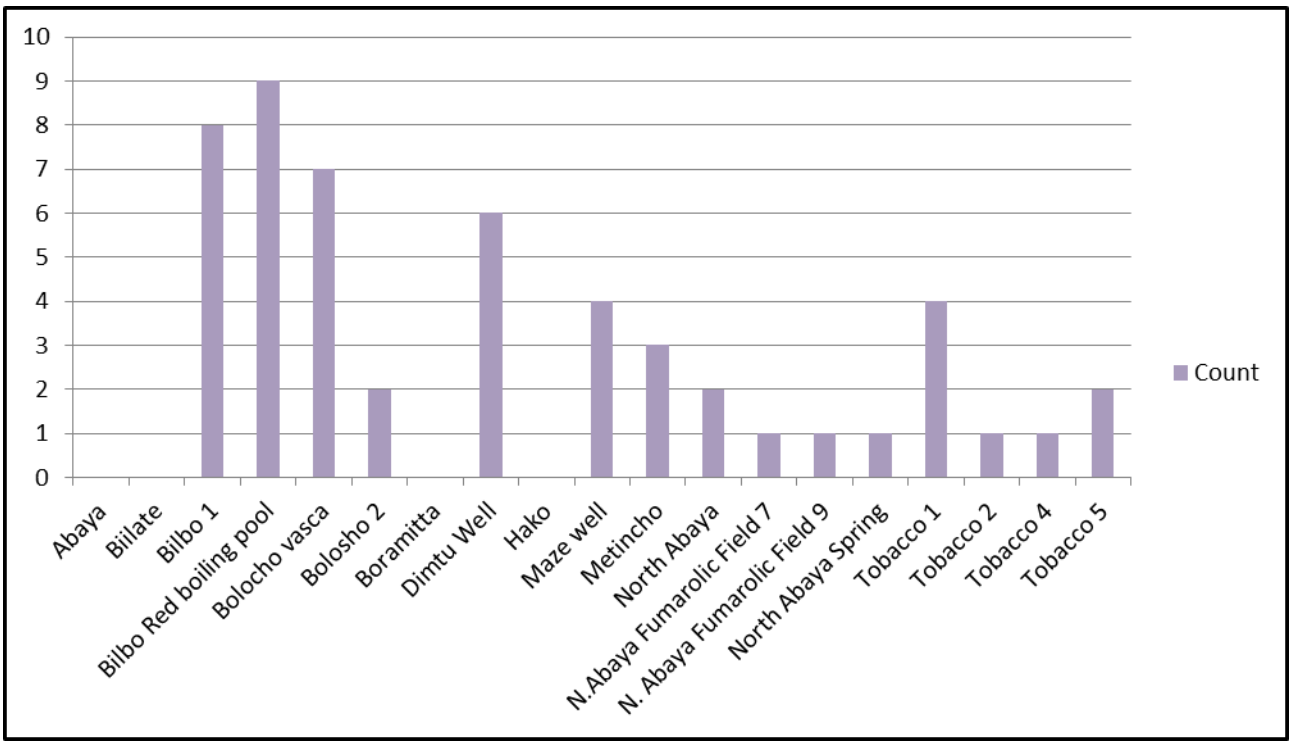

Figure 4. 20 *List of the surface manifestations and the count they appear to be anomalous.*

4.6 Validation of Land Surface Temperature Anomalies

It may not always be possible to test the reliability of LST results derived from TIR sensor with ground surface temperature due to non-availability of field data concomitantly with satellite overpass, nevertheless LST of a given area can be retrieved from other TIR sensors and compared on spatial scales if their overpass time is close to the satellite being used. In this study, MODIS TIR and AST_08 data were used for LST comparison and validation. LST data products of MODIS (MOD11A2) of 1 km spatial resolution couldn't be found on the exact days as the Landsat, therefore an average value of three months have been used. For the ASTER scenes the level 2 products of the same day as the AST_L1T were used.

The Landsat LSTs are re-sampled to 1000m to match with the MODIS products. The correlation between the MODIS and the derived LSTs from Landsat is lower compared to the ASTER. This is mainly related to the combined effect of the re-sampling process and the fact that we have used an average LST of three months.

The ASTER LSTs have higher correlation therefore lower difference between the derived LSTs and the level 2 products. A maximum difference of 6K have been traced this is mainly related to the difference in the algorithms used for estimation of the land surface. The present thesis used a single channel algorithm to estimate LST values of the study area whereas the level 2 products are driven using a Temperature Emissivity Separation (TES) method.

5. Chapter Five

Discussion

LST is an important measurement in studies related to the Earth surface processes. It is the temperature of the surface of the Earth and among the most important datasets collected by satellites from space. It can be obtained efficiently from Thermal infrared remote (TIR) sensing. Since it varies rapidly with time and location, in order to be able to acquire accurate LST measurements over time; there arises a need to estimate LST in a relatively higher spatial resolution. Due to the high variation of temperature over land, satellite derived LST provides researchers with a unique opportunity to acquire LST of the entire globe with a relatively high spatial resolution in average values rather than values in a point form (Li Z et al.,2013).

Integrated image analysis from different satellites like Landsat, ASTER and others give robust result to show temporal variables of LST. Varying characteristics of those satellites in spatial and radiometric resolutions, acquisition time and availability of a particular scene enables users to estimate multi temporal LST values of an area.

The combined result shows that some places like Abaya, Bilate, Boramita and Hako have low LSTs in almost all the 9 images and couldn't be determined as a geothermal area using the method applied even if they were identified to be anomalous by different researches (Tadiwos Cherenet, 2011; Solomon Kebede, 2015). Other places like North Abaya, Bolosho 2 have low LSTs in about 7 images. (Fig 4.6) this shows that using one image to show geothermal anomaly is not enough like in many researches (Darge et al., 2019). However multi temporal images from different datasets will give a better result in the indication of geothermal areas since it gives us a chance to consider and minimize the effects of factors. The spatial resolution of the sensor, the acquisition date of satellite images being used, the size and type of the surface manifestations

and the land covers of their surrounding are among the factors that influence the identification of anomalous areas and the surface heat manifestations near Lake Abaya area.

As the spatial resolution of the sensor gets lower, its ability to detect small features decreases that is why the fumaroles near the shore of the lake couldn't be identified. Regarding type, the bubbling pools which have the highest temperature in the area were identified to be anomalous in almost all the images. On the other hand the Hako steam vent doesn't appear to be anomalous in any of the analyzed nine images. This is mainly related to the fact that identifying a steam vent from a 90m distance is difficult and this can be considered as limitation of the method. The surrounding of the surface manifestations is also another factor which can be considered to have an influence in the detection of geothermal anomalous area.

5.1 Surface Temperature changes of the surface manifestations near Lake Abaya.

Braddok M. et al., 2017 was able to monitor the changes in the fumaroles activity of the Aluto volcano, Ethiopia using ASTER night time imageries. The surface manifestations show a temperature change of 1 to 9°C over the given time. Our result indicates that the surface manifestations in the study area also show an average temperature change of 7.6 K over the last 20 years. The maximum temperature change of 14.7K is attained in the Maze well whereas the lowest temperature change of 1.8K is attained in the thermal springs near the tobacco 4. (Table 5.1)

5.2 Comparison of the derived LSTs with the borehole data

Borehole data of the geothermal sites in the northern Lake Abaya area from the Geological Survey of Ethiopia (GSE) and other literatures have been compared with the derived LSTs. The result shows that the difference is in the range of 1.5 to 55.9K. A temperature difference of less than 25K have been traced in about 10 cites out of 15. The North Abaya spring, Metincho and tobacco 2 thermal springs are among the sites with the lowest temperature difference. The average LST value of the Northern Abaya spring, Metincho and Tobacco 2 thermal spring is

312.3, 323.5and 324.3K having a temperature difference of 1.5,10.4, and 10.5K respectively from the borehole data.

The spatial resolution of the satellite compared to the field data and the time of field survey are among the reasons why a temperature difference of such value is attained. The time for the field work is unknown as it is from literature but its value is much closer to the LST values of year 2003. The derived LSTs are estimated using a sensor 90m above the ground which is very small resolution as compared to a field survey. Moreover a borehole data records subsurface temperature unlike the satellites that are sensitive to the surface temperatures. A further investigation is needed to determine the exact locations of previously mapped geothermal sites, so that a temperature from the subsurface and the surface could be compared.

Table 5.1 List of the surface heart manifestations near the Lake Abaya area and their derived LST values (2000-2019)

Name	2000	2003	2006	2008	2012	2014	2016	2018	2019	2019-2000
Abaya	308.6	317.6	306.8	312.7	307	307.3	312.8	312.4	301.1	7.5
Biilate	305.4	316.3	301.9	307.6	309.4	303.7	306.2	306.7	298.8	6.6
Bilbo 1	314.5	327.6	311.2	323.2	320.1	310.5	319	319.8	308.1	6.4
Bilbo Red boiling pool	314.7	329.2	311.7	324.2	318.5	311.3	320.6	320.6	310.6	4.1
Bolocho vasca	314	331.7	309.4	321.8	315.7	312.6	317.7	313.4	305.7	8.3
Bolosho 2	312.7	319.1	306	310.7	306.1	308.9	315	315.9	304.5	8.2
Boramitta	312	316.5	308.9	309	305.2	308	310.6	307	301.6	10.4
Dimtu Well	314.7	330.3	311	322.3	319.6	310.1	315.1	313.4	306	8.7
Hako	309.4	320.3	307.1	310.1	305.8	305.9	305.4	308.4	300.4	9.0
Maze well	317.9	324.9	311	311.7	303.8	312.6	312.2	310.3	303.2	14.7
Metincho	314.5	325.1	303.1	317.5	312.9	309.2	313.5	315	306	8.5
North Abaya	310.9	320	308.4	315.8	310.8	309.7	314.4	312.9	303.2	7.7
North Abaya Fumarolic Field 7	313	319.4	308.6	312.1	307.1	309.2	312	308.6	305.3	7.7
North Abaya Fumarolic Field 9	313	321.5	308.6	313.7	308	309.2	312.6	308.1	306.1	6.9
North Abaya Spring	314.5	321.9	309.7	315.2	308	310.6	315	311.3	304.5	10.0
Tobacco 1	315	319.9	308.9	317	311.3	311	311.2	314.4	305	10.0
Tobacco 2	311.7	322.6	308.9	316.7	315.9	309.7	314.8	317	307.8	3.9
Tobacco 4	309.1	319	306.5	313.3	312.5	309.1	311.1	314	307.3	1.8
Tobacco 5	309.2	321	307.1	311.1	312.3	307.9	313	315.3	305.3	3.9

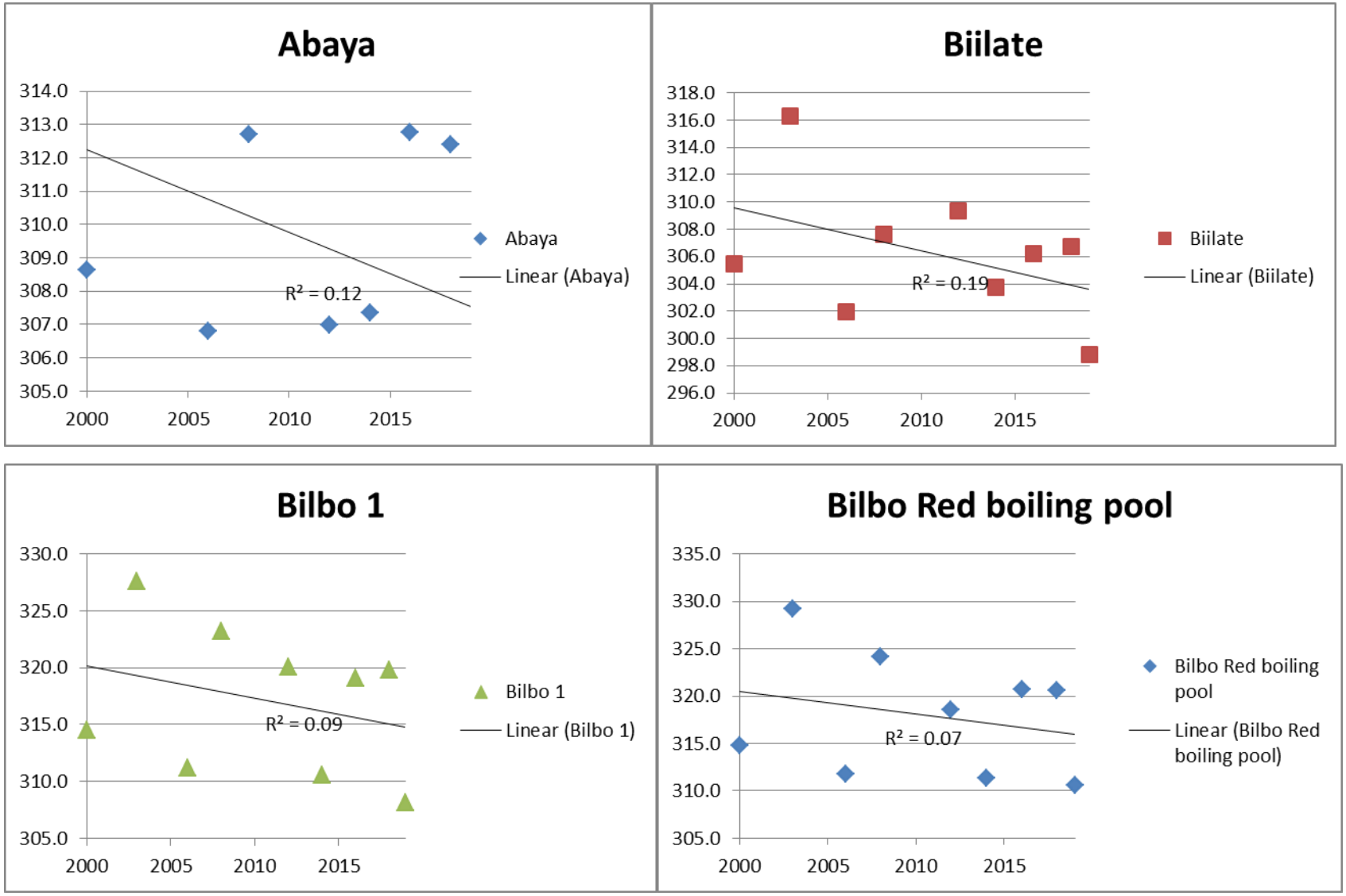
Abaya
314.0
313.0
312.0
311.0
310.0
309.0
308.0
307.0
306.0
305.0
2000
2005
2010
2015
R² = 0.12
Abaya
Linear (Abaya)
Biilate
318.0
316.0
314.0
312.0
310.0
308.0
306.0
304.0
302.0
300.0
298.0
296.0
2000
2005
2010
2015
R² = 0.19
Biilate
Linear (Biilate)
Bilbo 1
330.0
325.0
320.0
315.0
310.0
305.0
2000
2005
2010
2015
R² = 0.09
Bilbo 1
Linear (Bilbo 1)
Bilbo Red boiling pool
335.0
330.0
325.0
320.0
315.0
310.0
305.0
2000
2005
2010
2015
R² = 0.07
Bilbo Red boiling pool
Linear (Bilbo Red boiling pool)

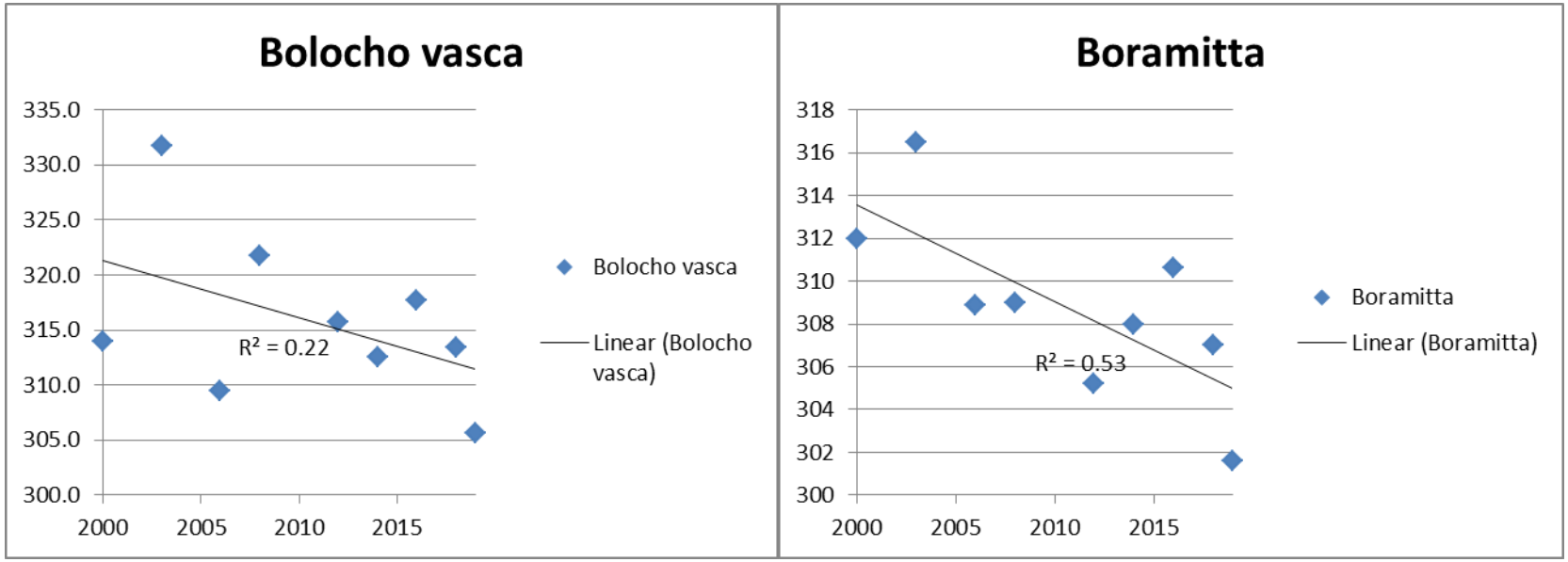
Bolocho vasca
335.0
330.0
325.0
320.0
315.0
310.0
305.0
300.0
2000
2005
2010
2015
R² = 0.22
Bolocho vasca
Linear (Bolocho vasca)
Boramitta
318
316
314
312
310
308
306
304
302
300
2000
2005
2010
2015
R² = 0.53
Boramitta
Linear (Boramitta)

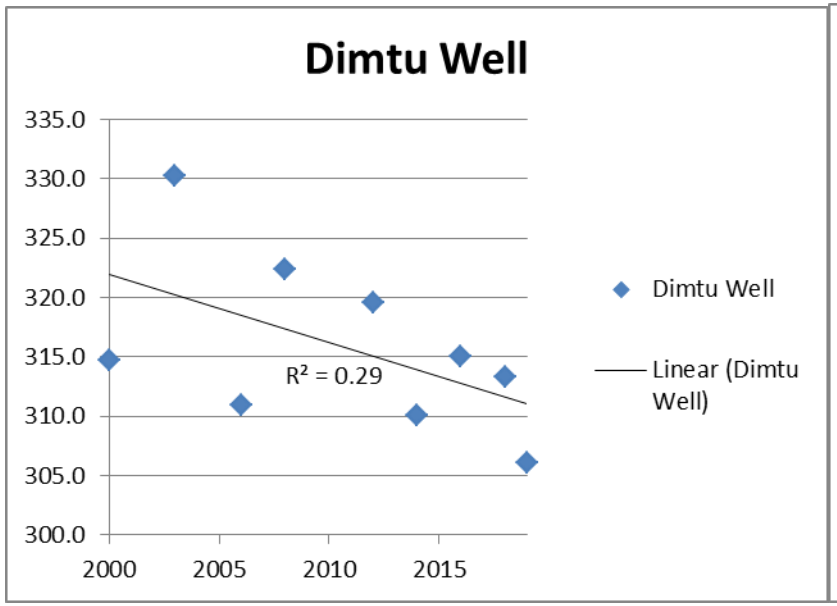
Dimtu Well
335.0
330.0
325.0
320.0
315.0
310.0
305.0
300.0
2000
2005
2010
2015
R² = 0.29
Dimtu Well
Linear (Dimtu Well)

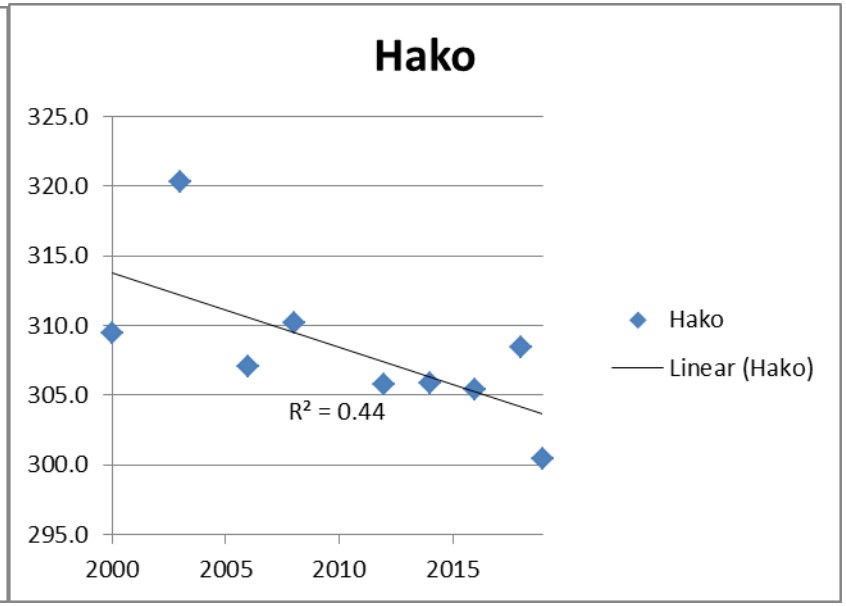
Hako
325.0
320.0
315.0
310.0
305.0
300.0
295.0
2000
2005
2010
2015
R² = 0.44
Hako
Linear (Hako)

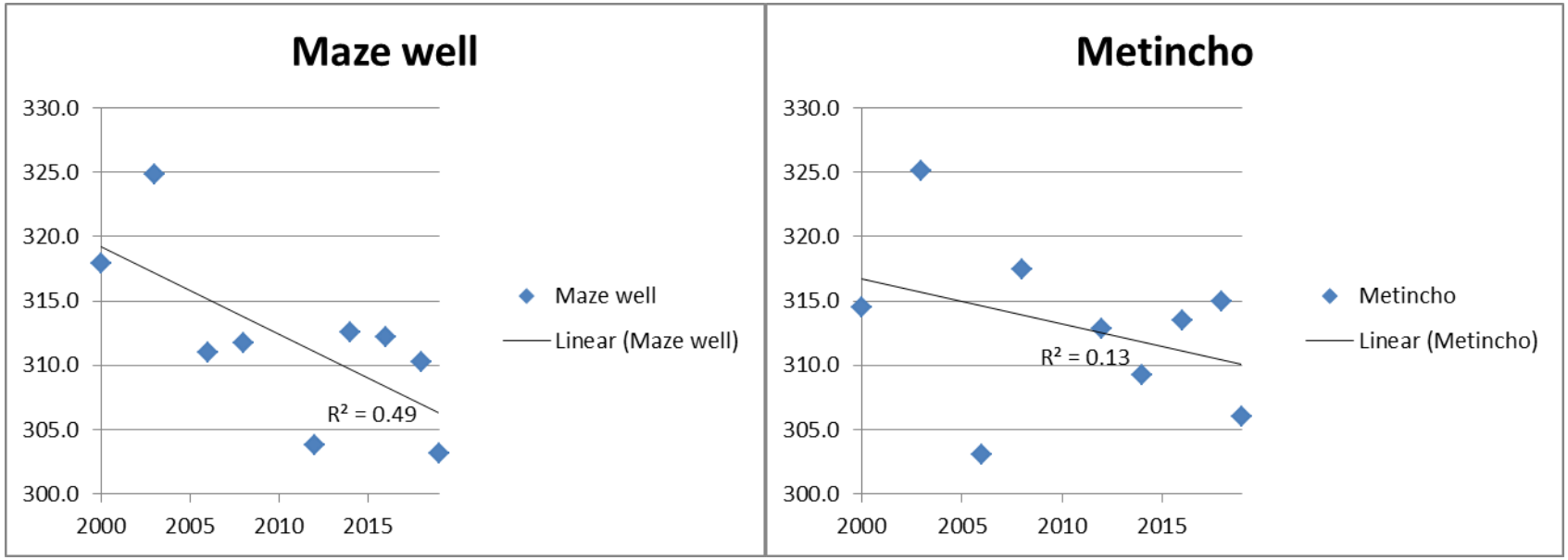
Maze well
330.0
325.0
320.0
315.0
310.0
305.0
300.0
2000
2005
2010
2015
R² = 0.49
Maze well
Linear (Maze well)
Metincho
330.0
325.0
320.0
315.0
310.0
305.0
300.0
2000
2005
2010
2015
R² = 0.13
Metincho
Linear (Metincho)

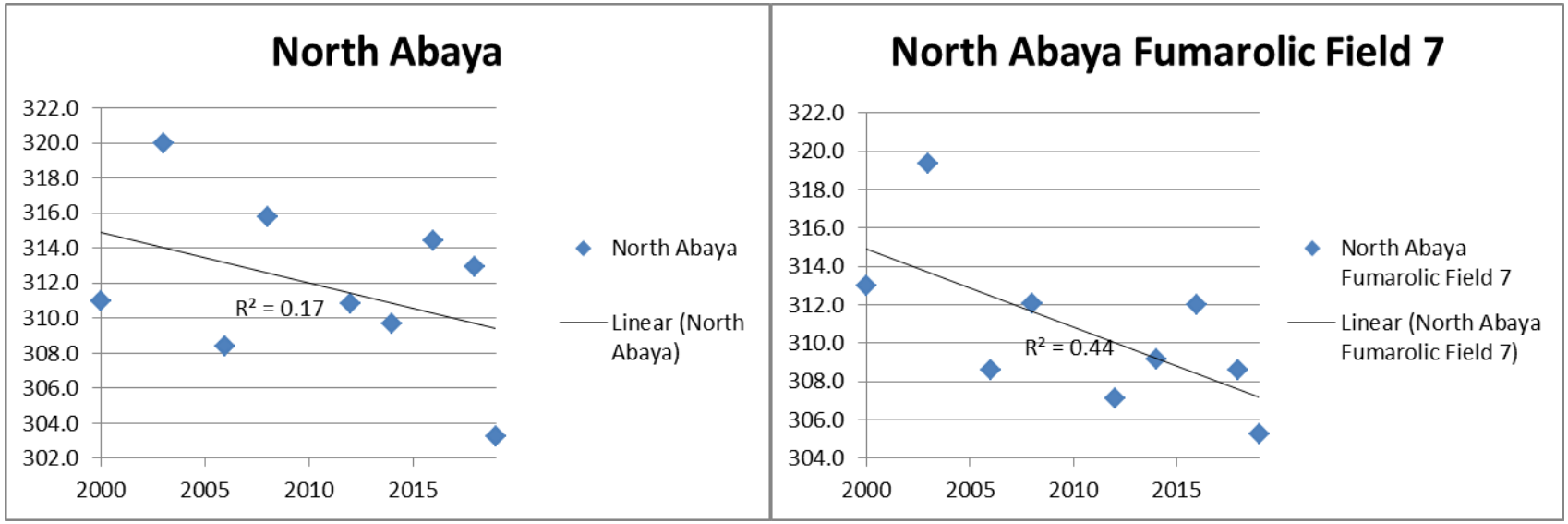
North Abaya
322.0
320.0
318.0
316.0
314.0
312.0
310.0
308.0
306.0
304.0
302.0
2000
2005
2010
2015
R² = 0.17
North Abaya
Linear (North Abaya)
North Abaya Fumarolic Field 7
322.0
320.0
318.0
316.0
314.0
312.0
310.0
308.0
306.0
304.0
2000
2005
2010
2015
R² = 0.44
North Abaya Fumarolic Field 7
Linear (North Abaya Fumarolic Field 7)

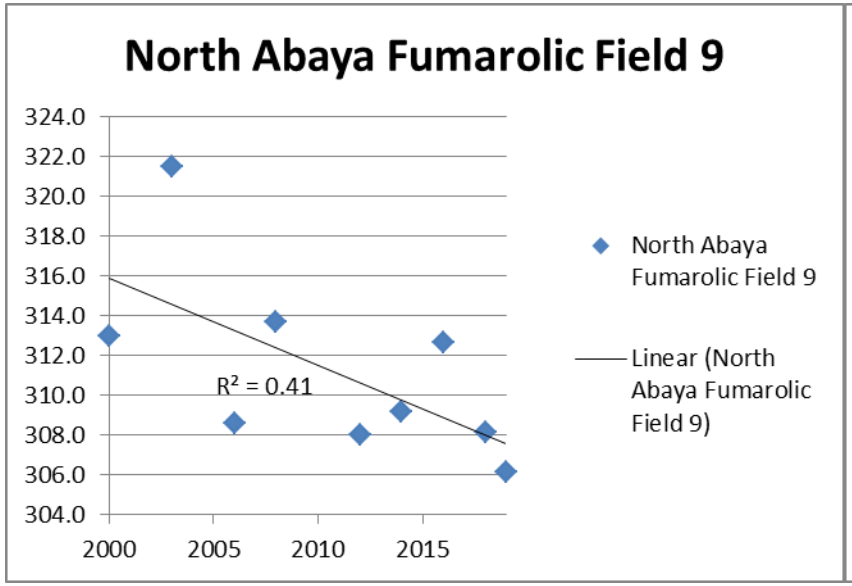
North Abaya Fumarolic Field 9
324.0
322.0
320.0
318.0
316.0
314.0
312.0
310.0
308.0
306.0
304.0
2000
2005
2010
2015
R² = 0.41
North Abaya Fumarolic Field 9
Linear (North Abaya Fumarolic Field 9)

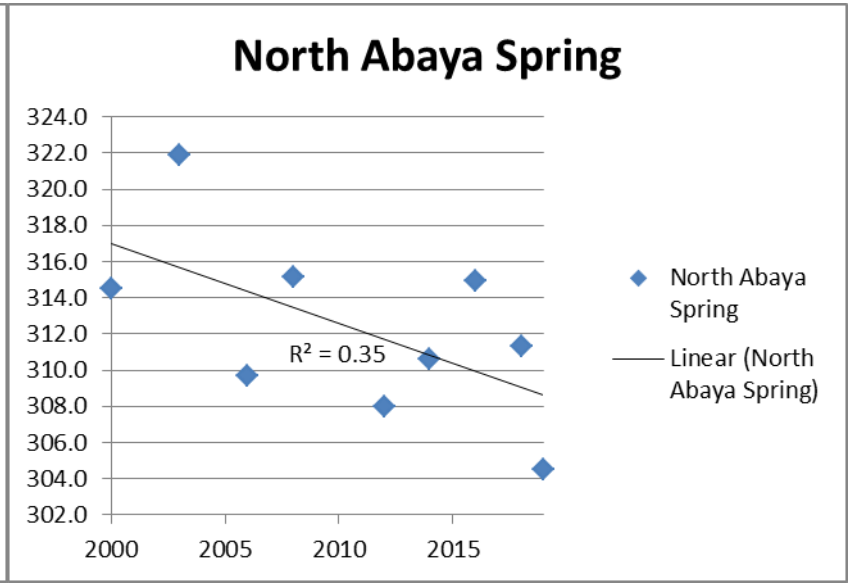
North Abaya Spring
324.0
322.0
320.0
318.0
316.0
314.0
312.0
310.0
308.0
306.0
304.0
302.0
2000
2005
2010
2015
R² = 0.35
North Abaya Spring
Linear (North Abaya Spring)

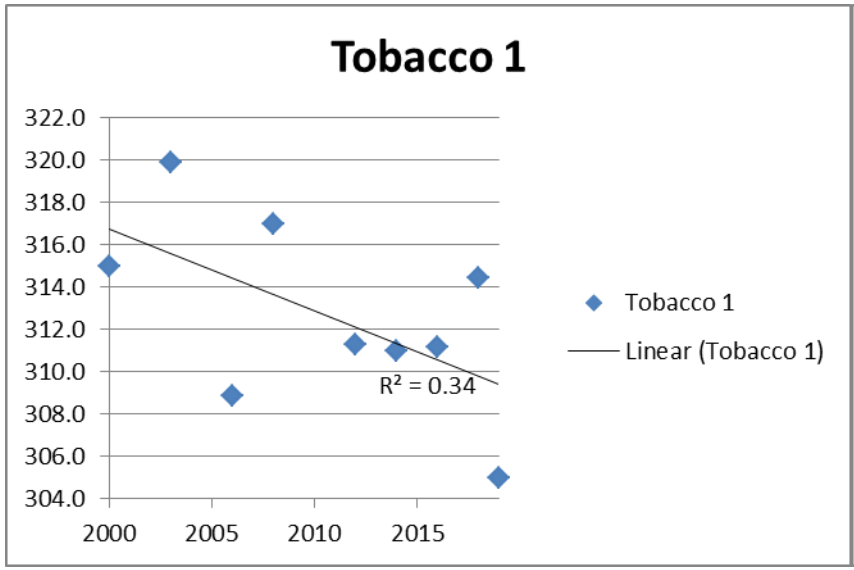
Tobacco 1
322.0
320.0
318.0
316.0
314.0
312.0
310.0
308.0
306.0
304.0
2000
2005
2010
2015
R² = 0.34
Tobacco 1
Linear (Tobacco 1)

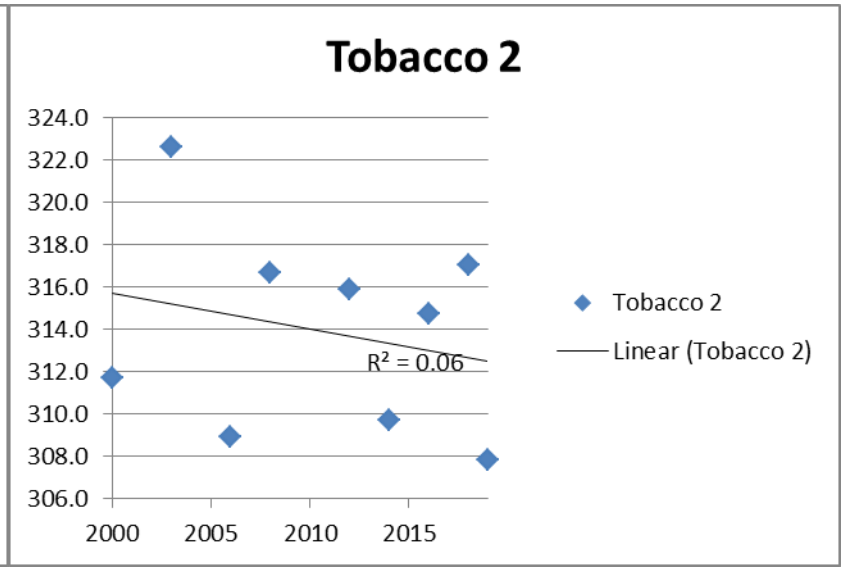
Tobacco 2
324.0
322.0
320.0
318.0
316.0
314.0
312.0
310.0
308.0
306.0
2000
2005
2010
2015
R² = 0.06
Tobacco 2
Linear (Tobacco 2)

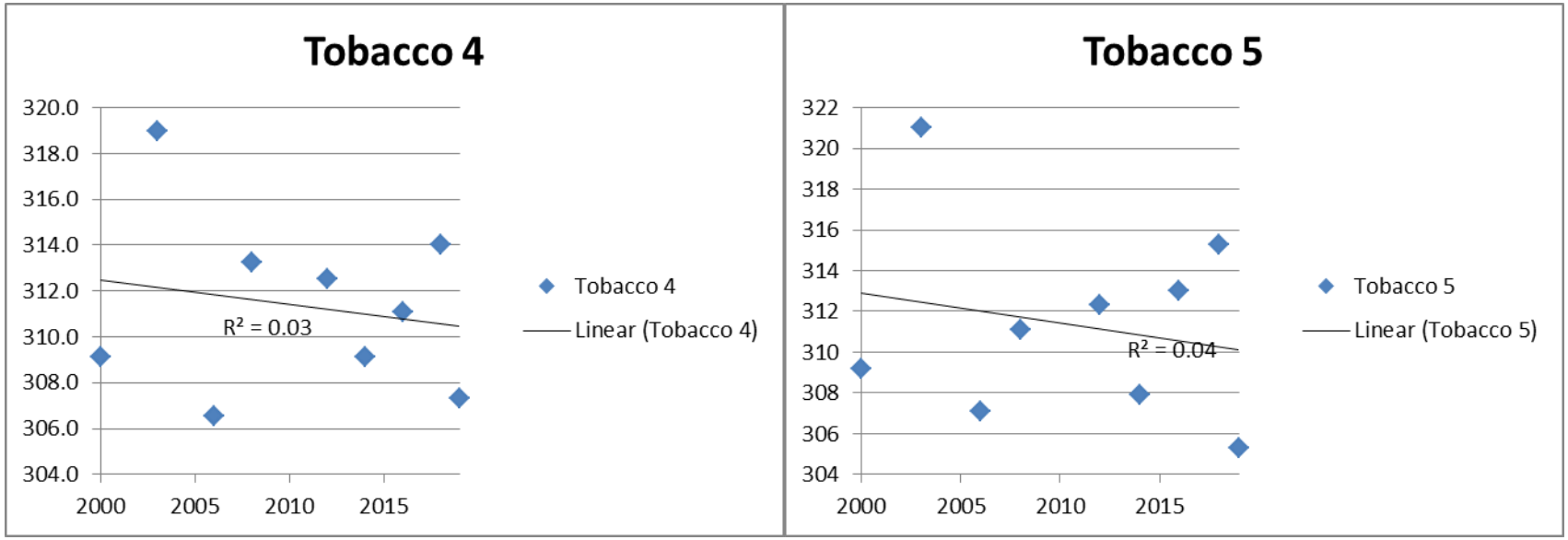

Figure 5. 1 *graphs showing the temperature changes of the surface heat manifestations in the area (2000-2019)*

As it can be seen from the graphs (Figure 5.1) in all the sites there is an inverse correlation between time and LST and in some cases no correlation at all. This shows that the LST is time invariant which goes well with the fact that there shouldn't be any significant change of LST in geothermal anomalous areas and confirms that the satellite results are correct.

Table 5.2 Derived LSTs (2000-2019) Versus Temperature measurements of a borehole data

Name	2000	2003	2006	2008	2012	2014	2016	2018	2019	T(K)	Average	Difference(K)
Bilbo 1	314.48	327.58	311.22	323.17	320.07	310.54	319.04	319.83	308.09	368.4	317.1	51.2
Bilbo Red boiling pool	314.74	329.2	311.72	324.19	318.51	311.35	320.65	320.58	310.63	368.6	318.0	50.6
Bolocho vasca	314	331.69	309.43	321.75	315.73	312.57	317.68	313.43	305.66	339.0	315.8	23.2

Bolosho 2	312.71	319.08	305.98	310.75	306.15	308.92	314.95	315.94	304.54	364.7	311.0	53.6
Dimtu Well	314.74	330.28	310.96	322.34	319.57	310.06	315.07	313.36	306.04	327.0	315.8	11.1
Maze well	317.94	324.86	310.96	311.69	303.78	312.59	312.24	310.3	303.19	300.4	312.0	11.6
Metincho	314.49	325.12	303.05	317.49	312.88	309.22	313.48	314.98	305.98	323.5	313.0	10.5
North Abaya	310.94	319.97	308.37	315.8	310.81	309.71	314.39	312.91	303.23	335.8	311.8	24.0
NorthAbaya Fumarolic Field 7	312.99	319.38	308.63	312.08	307.09	309.17	311.98	308.6	305.26	364.7	310.6	54.1
NorthAbaya Fumarolic Field 9	312.99	321.51	308.63	313.71	307.99	309.17	312.63	308.13	306.12	367.2	311.2	55.9
North Abaya Spring	314.49	321.87	309.67	315.18	308.01	310.59	314.96	311.34	304.48	313.8	312.3	1.5
Tobacco 1	314.988	319.88	308.89	316.987	311.26	310.998	311.15	314.42	304.969	336.6	312.6	23.9
Tobacco 2	311.71	322.62	308.9	316.65	315.88	309.69	314.77	317.03	307.84	324.3	313.9	10.4
Tobacco 4	309.14	318.98	306.53	313.27	312.52	309.11	311.11	314.04	307.34	324.7	311.3	13.3
Tobacco 5	309.16	321	307.08	311.14	312.29	307.93	312.99	315.35	305.28	331.2	311.4	19.8

6. Chapter Six

Conclusion and Recommendation

There exist several methods for detecting geothermal anomalies and most require a very large amount of resources (time, budget and expertise) if one uses geophysical methods and ground surveys. Remote sensing technology has been greatly used in the identification of geothermal anomaly areas in different parts of the world. Land Surface Temperature (LST), which is a radiative skin temperature of the land surface, is an important measurement in studies related to the Earth surface's processes. In the present thesis, a multi temporal Thermal infrared (TIR) remote sensing data (2000-2019 in two years interval) from ASTER and Landsat has been used to detect geothermal areas and evaluate the LST of the northern Lake Abaya area of the southern Main Ethiopian Rift (MER).

The study uses the single channel algorithm to derive LSTs of the study area for the last 20 years and compare the result with borehole data from different literatures. The combined result shows that some geothermal sites couldn't be determined to be anomalous at all, some others have been identified to be anomalous in a few images out of nine even if they were identified to be anomalous by different researches this show that using one time image analysis won't be enough to determine anomalous areas with geothermal potential. However, a multi-temporal image analysis could give a better result as it gives the analyst a chance to minimize the effects of different factors on the derived LSTs and get rid of the false anomalies.

The temperature value next to the mode has been used as the background value for all the nine images. Areas having higher LST values than the background have been considered to be anomalous. Areas with temperature values as high as 333K have been measured in the year 2003. The mean LST is highest in 2003 (320.1 K) and lowest in 2019 (303.1 K). The change in mean LST was between –9 K to 13 K. This LST results from ASTER images were validated with ASTER LST products and show more than 0.7 correlations.

The derived LSTs from the nine images were compared with the borehole data. LSTs of the year 2003 have been much closer to the temperature value from borehole data (Sub-surface temperature). The geothermal anomaly areas were validated with the existed field data (19 sites). Fifteen sites fall in the identified geothermal anomaly areas, which is 79 % of the total. The spatial resolution of the sensor, the acquisition date of satellite images being used, the size and type of the surface manifestations and the land covers of their surrounding are among the factors that influence the identification of anomalous areas and the surface heat manifestations near Lake Abaya area.

The result of correlation between time and LST values in known geothermal activity sites shows no correlation (less than 0.5) except one site, which is Boramitta (0.53). This shows that the LST is time invariant which goes well with the fact that there shouldn't be any significant change of LST in geothermal anomalous areas.

The results also indicate that thermal infrared remote sensing is an overall effective and accurate method for geothermal exploration especially for the pre visibility of geothermal exploration. The methodology applied in this work has efficiently reduced the extent for geothermal exploration and locate the promising geothermal areas for further exploration. The spatial difference between the known sites and the identified anomalous areas were very small proving that a remote sensing thermal infrared is a very important tool in the indication of anomalous areas with geothermal potential. The re

However, it can only detect the surficial thermal anomaly and is sensitive to the geothermal resource covered by vegetation/forest with small in size. Therefore, geologic analysis and the mechanism of geothermal anomaly are required to assist and facilitate the identification of geothermal areas with TIR remote sensing. With the knowledge of geothermal mechanism and the complement from the geological investigation, the accuracy of geothermal detection using TIR remote sensing can be much improved.

Reference

1. Abiye.T.A., (2003), "Controls on the occurrence of cold and thermal springs in the central Ethiopia". *African Geoscience Review*. 19(4):245-251
2. Abrams M. (2000). "The Advanced Thermal Emission and Reflection Radiometer (ASTER):Data products for the high spatial resolution imager on NASA'S Terra platform" *International Journal of Remote Sensing*.21(5):847859
3. Abrams M., Tsu H., Hulley G., Iwao K., Pieri D., Cudahy T., Kargel J. (2015). "The Advanced Thermal Emission and Reflection Radiometer (ASTER) after fifteen years: Review of global products". *International Journal of Applied Earth Observation and Geoinformation.* 38*:292-301.*
4. Aparicio, M.S Anaya P.A, Del Pozo S. and Laguela S. (2020). "Retrieving Land surface Temperature from Satellite Imagery with a Novel Combined Strategy". *Remote sensing* 12:277
5. Ashok S.; Pramod V K.: Arora, Manoj K. (2007) "Robustness of Change Detection Algorithms in the Presence of Registration Errors" *Photogrammetric Engineering and Remote Sensing.* 4:375-383
6. ASTER Reference guide version 1 (2003) ERSDAC Earth Remote Sensing Data Analysis Center. http://www.science.aster.ersdac.or.jp/en/index.html
7. Avdan U. and Jovanovska G. (2016) "Algorithm for Automated Mapping of land Surface Temperature Using LANDSAT 8Satellite Data" *Sensors* doi.org/10.1155/2016/1480307
8. Boccaletti M, Bonini M, Muzzuoli R, Bekele Abebe, Piccardi L., Tortorici L. (1998). "Quaternary oblique extensional tectonics in the Ethiopian Rift (Horn of Africa)." *Tectonophysics,* 287(1-4): 97-116.
9. Bonini M, Corti G, Innocenti F, Manetti P, Mazzarini F, Tsegaye Abebe, Pecskay Z.(2005). "Evolution of the Main Ethiopian Rift in the fram of Afar and Kenya rifts propagation" *Tectonics* 24(1).

10. Bonini M, Sokoutis D, Genene Mulugeta, Bocaletti M, Corti G. , Innocenti F., Manetti P, Mazzarini F.(2001). "Dynamics of magma emplacement in centrifuge models of continental extension with implications for flank volcanism". *Tectonics.* 20 (6) https:// doi.org10.1029/2001TC900017
11. Braddock M, Biggs J, Watson L.M, Hutchison W, Pyle D.M and Mather T.A. (2017). "Satellite observations of fumarole activity at Aluto Volcano, Ethiopia, Implications for geothermal monitoring and volcanic hazard". *Volcanology and Geothermal Research,* DOI: 10.1016/j.jvolgeores.2017.05.006.
12. Chan, H., Chang, C. and Dao, P. (2018). "Geothermal Anomaly Mapping Using Landsat ETM+ Data in Ilan Plain, Northeastern Taiwan." *Pure and Applied Geophysics.* 175: 303-323
13. Coolbaugh M.F, Kratt C, Fallacaro A, Calvin W.M , Taranik J.V. (2007) "Detecting of geothermal anomalies using Advanced Thermal Emission and Reflection Radiometer (ASTER) thermal infrared images at Bradys Hot springs, Nevada,USA". *Remote Sensing of Environment* 106(3):350-359
14. Corti G. (2008). "Control of the rift obliquity on the evolution and segmentation of the Main Ethiopian Rift". *Nature Geoscience* 1:258-262
15. Corti G. (2009). "Continental rift evolutions: From rift initiation to incipient breakup in the Main Ethiopian Rift, East Africa" *Earth Science Reviews*. 96(1-2):1-53
16. Curewitz D, Karson J. A (1997). "Structural setting of hydrothermal out flow: Fracture permeability maintained by fault propagation and interaction" *Journal of Volcanology and Geothermal Research Vol 79:149-168*
17. Dar, I., Qadir, J. and Shukla, A. (2019). "Estimation of LST from multi-sensor thermal remote sensing data and evaluating the influence of sensor characteristics." *Annals of GIS*, 25(3): 263-281. https://doi.org/10.1080/19475683.2019.1623318
18. Dickson, M. and Fanelli, M. (2004). What is geothermal energy? Instituto di Geoscienze e Georisorse, CNR, Pisa, Italy.
19. Duda K., Siemonsma D., Daucsavage J., Brooks B., (2015). AST_L1T Product User's Guide USGS EROS Data Center Sioux Falls, South Dakota, USA.

20. Ebinger C. J, Alan, L Deino, RE Drake, AL Tesha, (1989). "Chronology of volcanism and rift basin propagation: Rungwe volcanic province, East Africa." *Geophysical Research: Solid Earth*, 94 (B11): 15785-15803.
21. Ebinger C.J, Tesfaye Yemane, Giday Woldegabriel, Aronson JL and Rc Walter, (1993). "Late Eocene-Recent volcanism and faulting in the southern main Ethiopian rift." *Geological Society*, 150 (1): 99-108.
22. EIGS-GEP,(1981). "Geological report on North Lake Abaya Geothermal region",40 pp. Unpublished Report,1:250,000 Scale map by Berhane Melaku,Molla Bellaineh, Nigussie Mekuria, Paulos Tesfa Giorgis and Tesfaye T/Mariam., Geothermal exploration project, EIGS, Addis Abeba.
23. Feizizadeh, B., T. Blaschke, H. Nazmfar, E. Akbari, and H. Kohbanani, (2013). "Monitoring Land Surface Temperature Relationship to Land Use/Land Cover from Satellite Imagery in Maraqeh County, Iran." *Environmental Planning and Management* 56: 1290-1315.
24. Fred G.R Watson, Ryan E. Lockwood , Wendi B. Newman, Thor N. Anderson, Robert A. Garrot. (2008). " Development and comparison of Landsat radiometric and snowpack model inversion techniques for estimating geothermal heat flux" *Remote Sensing of Environment* 112(2):471-481
25. Ghulam A., (2009). How to calculate reflectance and temperature using ASTER data. Unpublished document www.PANCROMA.com accessed on 12/11/2019, 7:41.
26. Gibson I.L (1969) "The structure and Volcanic Geology of an axial portion of the Main Ethiopian Rift" *Tectonophysics.* 8(4-6): 561-565
27. Harvey M.C., Rowland J.V, Luketina K.M (2016)."Drone with thermal infrared camera provides high resolution georeferenced imagery of Waikite geothermal area,New Zealand". *Journal of Volcanology and Geothermal Research Vol* 325:61-69.
28. Hayward N.J and Ebinger C. (1996). "Variations in along-axis segmentation of the Afar Rift System." *Tectonics,* 15 (2): 244-257.
29. Heasler, H., C. Jaworowski, and D. Foley, (2009). "Geothermal systems and monitoring hydrothermal features". Geological Monitoring. R. Young and L. Norby. Boulder, Colorado, Geological Society of America.

30. Heasler, H., Jaworowski, C., (2018). "Hydrothermal monitoring of Norris Geyser Basin, Yellowstone National Park, USA, using airborne thermal infrared imagery". *Geothermics* 72, 24–46.
31. Hellman M.J, Ramsey M.S (2004). "Analysis of hot springs and associated deposits in Yellowstone National park using ASTER and AVIRIS remote sensing" *Journal of Volcanology and Geothermal Research.* 135(1-2):195-219.
32. Hewson, R., Mshiu, E., Hecker, C., Van der Werff, H., Van Ruitenbeeka, F., Dinand, Alkema, D., Freek Van der Meer F. "The application of day and night time ASTER satellite imagery for geothermal and mineral mapping in East Africa." *Int. Applied Earth Observation and Geoinformation*, https://doi.org/10.1016/j.jag.2019.101991.
33. Hochstein, M.P. (1990). Classification and assessment of geothermal resources, In: Dickson, M.H. and Fanelli, M., *eds*., *Small Geothermal R00esources: A Guide to Development and Utilization*, UNITAR, New York, 1990, pp. 31—57.
34. Japan International Cooperation Agency (JICA) (2015) .The project for formulating master plan on development of geothermal energy in Ethiopia. Addis Ababa, Ethiopia. Unpublished report of geological Survey of Ethiopia (GSE).
35. Jimenez-Munoz J.C, Sobrino J.A., Gillespie A., Sabol D., Gystafson W.T. (2006). "Improved land surface emissivitys over agricultural areas using ASTER NDVI". *Remote Sensing of Environment*, 103: 474-487.
36. Jimenez-Munoz J.C. and Sobrino J.A, (2007). "Feasibility of Retrieving Land-Surface Temperature From ASTER TIR Bands using Two-Channel Algorithms, A case study of Agricultural Areas". *IEEE Geoscience and Remote Sensing Letters*, 4 (1)
37. Karnieli, A., N. Agam, R. T. Pinker, M. Anderson, M. L. Imhoff, and G. G. Gutman. 2010. "Use of NDVI and Land Surface Temperature for Drought Assessment: Merits and Limitations." Journal of Climate 23: 618–633.
38. Keranen K; Klempere S.L; Glouguen R; eagle Working Group. (2004) "Three dimensional seismic imaging of a protoridge axis in the Main Ethiopian Rift." *Geology* 32(11):949-952.
39. Lee K. (1978). "Analysis of thermal infrared imagery of the Black Rock Desert geothermal area" *Colorado School of Mines Quarterly*, 4(2):31-48

40. Li Z.L, Tang B.H, Wu H., Ren H., Yan G., Wan Z., Trigo I.F, Sobrino J.A(2013) "Satellite derived Land Surface temperature : Current status and perspectives". *Remote Sensing of Environment.*131 (15):14-37.
41. Lloyd, E. F., (1977). "Geological factors influencing Geothermal Exploration in the Langano Region, Ethiopia. Unpublished report, NZ Geological survey, Rotoura, New Zealand , pp.73
42. Lu D., Weng Q. (2006), "Spectral mixture analysis of ASTER images for examining the relationship between urban thermal feature and biophysical descriptors in Indianapolis, Indiana,USA". *Remote Sensing of Environment* 104(2):157-167
43. McMillin L.M (1975). "Estimation of Sea surface temperatures from two infrared window measurements with different absorption" *Journal of Geophysical Research* 80(36). https:// doi.org/10.1029/JC080i036p05113
44. Meseret Teklemariam, (2008). "Strategic plan for geothermal exploration and development in Ethiopia". In: Presented at Short Course III on Exploration for Geothermal Resources, organized by UNU-GTP and KenGen, at Lake Naivasha, Kenya, Oct. 24 – Nov. 17.
45. Milton I.N and Avdan U., 2016. Inversion of Land Surface Temperature (LST) Using Terra ASTER Data, A Comparison of Three Algorithms. *Remote sensing.* 8:993
46. Minissale, A., Corti, G., Tassi, F., Darrahc, T. H., Vaselli, O., Montanari, D., Montegrossi G., Gezhagn Yirgu, Selmo, E. and Asfaw Teclu (2017). "Geothermal potential and origin of natural thermal fluids in the northern Lake Abaya area, Main Ethiopian Rift, East Africa". *Journal of Volcanology and Geothermal Research*, 336: 1-8.
47. Moeck (2014). "Catalog of geothermal play types based on geologic controls." *Renewable and Sustainable Energy Reviews*, 37: 867-882.
48. Mohr, P. (1962). "The Ethiopian Rift System". *Nature*, 5*:*33-62.
49. Mohr, P. and Zanettin, B. (1988). "The Ethiopian flood basalt province". Kluwer Academic Publishers, 45: 63–110.
50. Monteih J.L and Unsworth M.H (1973). "Principle of Environmental Physics" Edward Arnold, London, United Kingdom

51. Oguz H. (2014). "A Software tool for retrieving Land Surface Temperature from ASTER imagery" *Journal of Agricultural Sciences*
52. Omenda, P.A. and Meseret Teklemariam (2010). "Overview of geothermal resource utilization in the east African rift system". In: *Presented at Short Course V on Exploration for Geothermal Resources*, organized by UNU-GTP, GDC and KenGen, at Lake Bogoria and Lake Naivasha, Kenya, Oct. 29 – Nov. 19.
53. Philippon M, Corti G, Sani F., Bonini M, Balestrieri M.L and Molin P, Willingshofer E, Sokoutis D and Cloetingh S. (2014). 'Evolution, distribution and characteristics of rifting in southern Ethiopia". *Tectonics,* 33 (4): 485-508.
54. Prakash, R.G.S Sastry, R.P .Gupta and A. K. Saraf(1995) "Estimating the depth of buried hot features from thermal IR remte sensing data: a conceptual approach" *International Journal of Applied Earth Observation and Geoinformation.* 16(13): 2503-2510
55. Purschel, M., Gloaguen, R., Stadler, S. (2013). " Geothermal activities in the Main Ethiopian Rift: hydro geochemical characterization of geothermal waters and geothermometry applications (Dofan-Fantale, Gergede-Sodere, Aluto-Langano)." *Geothermics* 47: 1–12.
56. Qin, Q., Ning, Z., Peng, N. and Leile, C. (2011). "Geothermal area detection using Landsat ETM+ thermal infrared data and its mechanistic analysis- A case study in Tengchong, China." *International Journal of Applied Earth Observation and Geoinformatics*.13: 552-559.
57. Ramdhan, M.R (2019). "The investigation of geothermal temperature anomalies and structures using airborne TIR and LiDAR data, a case study in Bajawa area, Indonesia." Unpublished MSc Thesis, pp 65.
58. Ronald, D. (2005). Geothermal Power Plants: Principle, Applications and Case Studies. Elsevier, UK, 512 pp.
59. Rozenstein, O., Qin, Z., Dermian, Y. and Karnieli, A. (2014). Derivation of Land Surface Temperature for Landsat-8 TIRS Using a Split Window Algorithm . *Sensors* 14(4), 5768-5780.

60. Rudnik R.L, William F. McDonough, Richard J. O'Connell (1998). "Thermal structure thickness and composition of continental lithosphere" *Chemical Geology*. 145(3-4):395-411.
61. Siahaan, M., Soebandrio, A. and Wikantika, K. (2011). "Geothermal Potential Exploration Using Remote Sensing Technique (Case Study: Patuwa area, West Java)". In: Proceedings of the 10th Annual Asian Conference, pp. 1–13. Jakarta, Indonesia
62. Sobrino J.A., Jimenez-Munoz J.C, Paolini L. (2004) "Land surface temperature retrieval from LANDSAT TM 5". *Remote Sensing of Environment* 90(4):434-4430
63. Solomon Kebede, (2015): "Country update on geothermal exploration and development in Ethiopia". In: Presented at Short Course IX on Exploration for Geothermal Resources, organized by UNU-GTP, GDC and KenGen, at Lake Bogoria and Lake Naivasha, Kenya, Nov. 9 - Dec.1
64. Tadiwos Chernet (2011). "Geology and hydrothermal resources in the northern Lake Abaya area, Ethiopia.' *Journal of African Earth Sciences*, 61: 129-141.
65. Tsegaye Abebe, Balestrieri M.L. and Bigazzi G. (2010). "The Central Main Ethiopian Rift is younger than 8 Ma: confirmation through apatite fission-track thermochronology". *Terra Nova*, 22: 470-476.
66. U.S. Geological Survey (2014) Landsat 8 data users handbook. USGS Earth Resources Observation and science, Sioux Falls, South Dakota,USA.
67. United Nation Development Program (UNDP) (1973). Investigation of geothermal resources for power development: Geology, geochemistry and hydrology of hot springs of the East Africa rift system within Ethiopia. Unpublished technical report, (UNDP), United Nations, New York, 146 pp.
68. Van der Meer, F., Hecker, C., Van Ruitenbeek, F., Can der Werff, H., de Wijkerslooth, C. and Wechsler, C. (2014). "Geologic remote sensing for geothermal exploration": A review. *Applied Earth Observation and Geoinformation.* 33: 255-269.
69. Varghese J. (2016). "Detecting the effects of soil moisture and hotspot size on geothermal anomalies via remote sensing techniques" unpublished thesis work. Pp 55

70. Vaughan, R.G., Hook, S.J., Calvin, W.M., Taranik J.V.(2005) " Surface mineral mapping at Steamboat Springs, Nevada, USA with multi wavelength thermal infrared images" *Remote Sensing of Environment.* 99(1-2):140-158
71. Wang K., Giang Q., Yu D., Yang Q., Wang L., Han T.C., Xu X. (2019). "Detecting daytime and nighttime land surface temperature anomalies using thermal infrared remote sensing in Dandong geothermal prospect" *International Journal of Applied Earth Observation and Geoinformation.* 80:196-205
72. Weng Q., Lu D., Schubring J. (2004) "Estimation of Land surface temperature-vegetation abundance relationship for urban heat island studies". *Remote Sensing of Environment* 89(4):461-483
73. Wolfenden E, Ebinger C, Gezahegn Yirgu and Deino A., Dereje Ayalew (2004). "Evolution of the Main Ethiopian Rift: Birth of a triple junction". *Earth and Planetary science,* 224 (1-2): 213-228.
74. Wu, P., H. Shen, A. Tinghua, and Y. Liu. (2013). "Land-Surface Temperature Retrieval at High Spatial and Temporal Resolutions Based on Multi-Sensor Fusion." *Digital Earth* 6 (1): 113–133. Doi: 10.1080/ 17538947.2013.783131.
75. Y. Nithiyanandam ,J. E. Nichol(2016) "A simple and effective retrieval of land surface temperature using a new reflectance based emissivity estimation technique" *The International Archives of the Photogrammetry, Remote Sensing and Spatial Information Sciences,* XLI-B8, 2016 XXIII ISPRS Congress, 12–19 July 2016, Prague, Czech Republic.
76. Yosef Mengistu Darge, Binyam Tesfaw Hailu, Ameha Atnafu Muluneh and Tesfaye Kidane. (2019). "Detection of geothermal anomalies using Landsat 8 TIRS data in Tulu Moye geothermal prospect, Main Ethiopian Rift". *Applied Earth Observation Geoinformation.* 74: 16-26.

Appendices

Appendix A: Geological Map of study area in scale 1: 50, 000. Source: Geological Survey of Ethiopia.

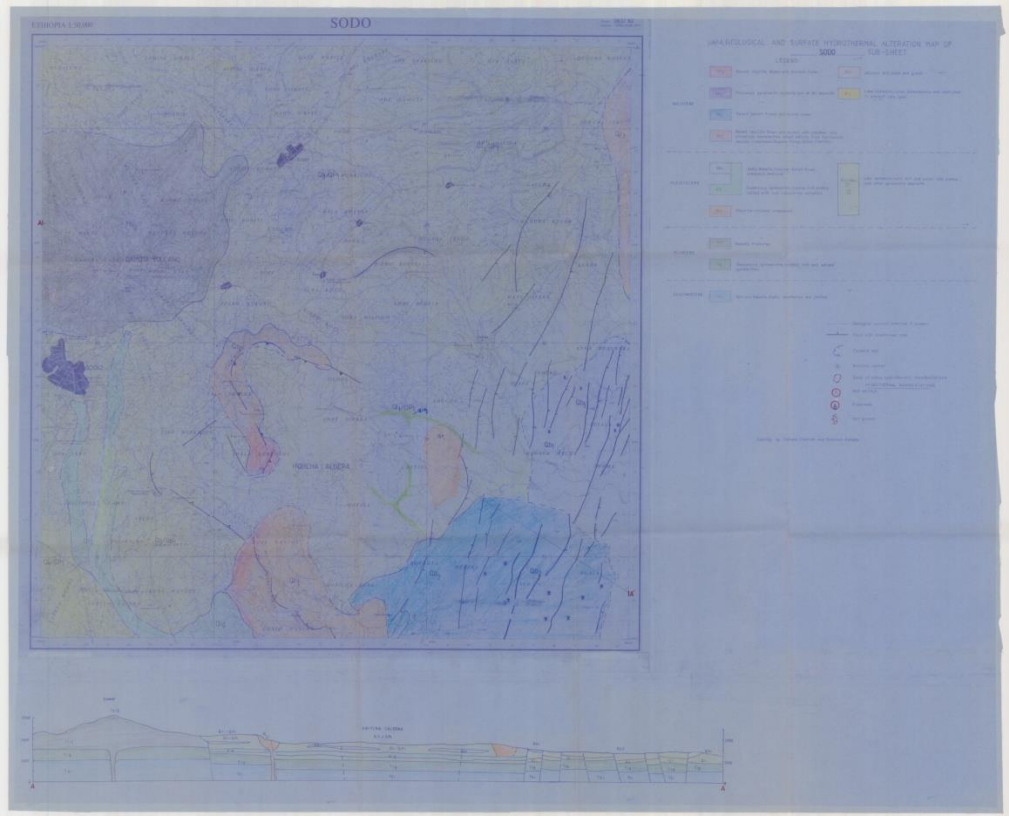

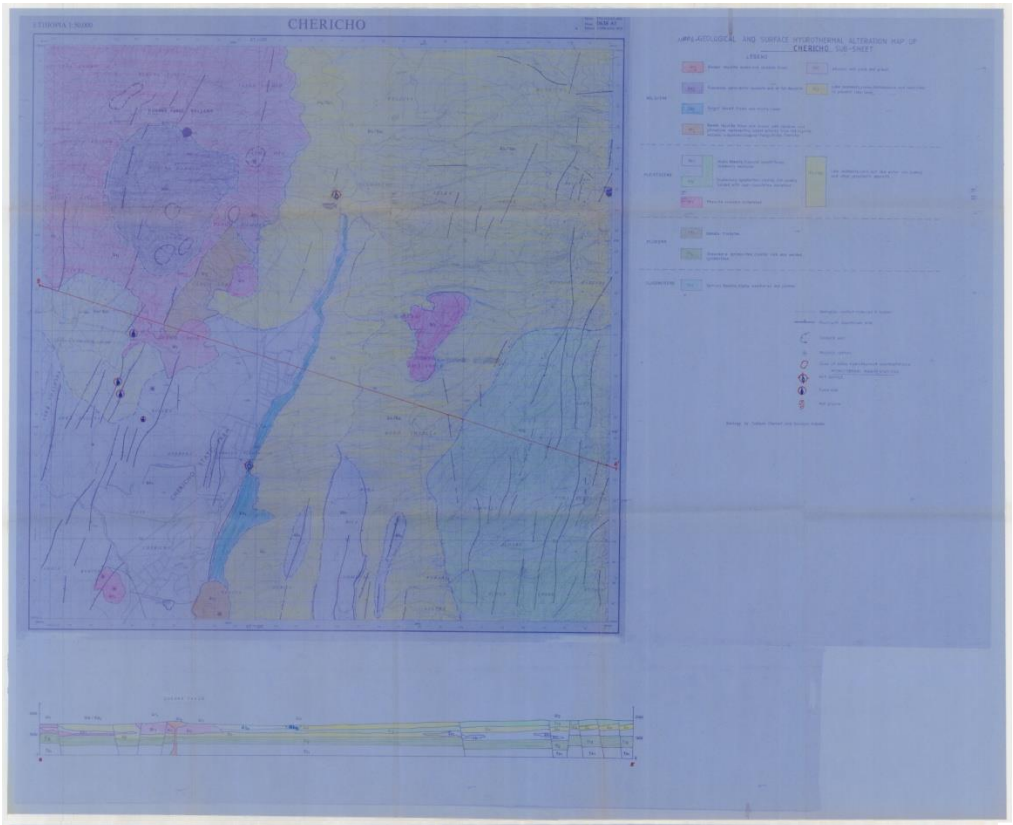
CHERICHO

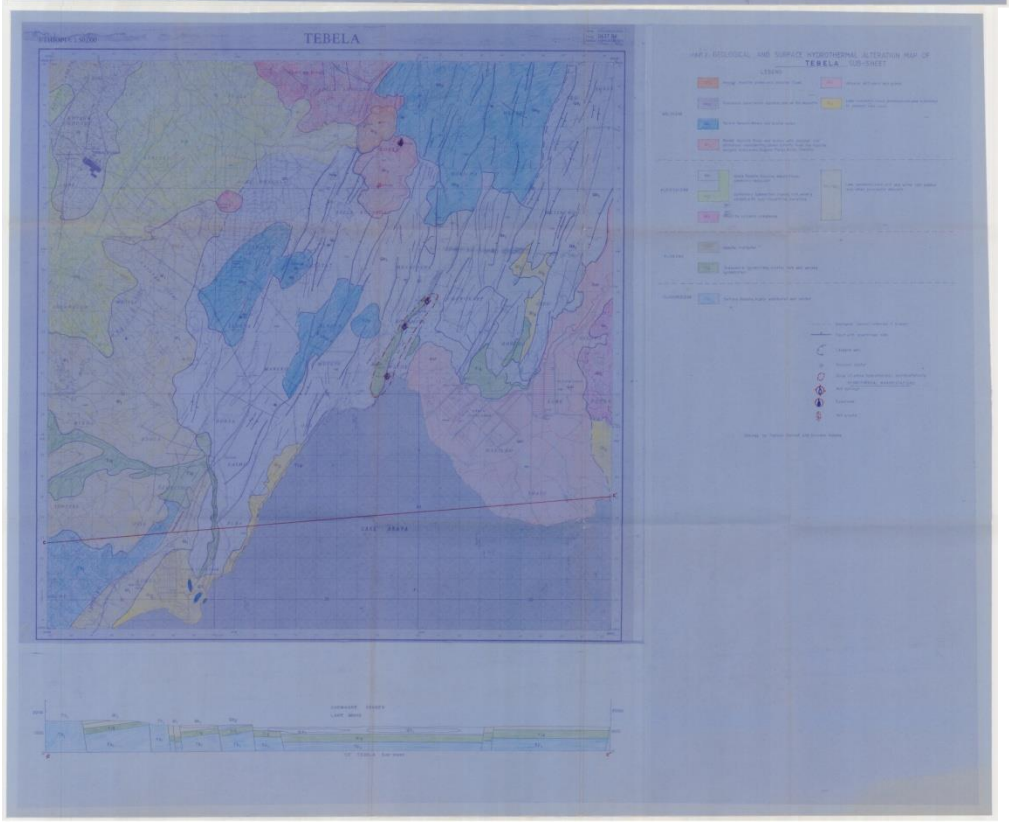
TEBELA


Map 8. GEOLOGICAL AND SURFACE HYDROTHERMAL ALTERATION MAP OF PART OF SODO SUBSHEET (1·20,000 Scale)
SURA KOYE
AMBE BEDESA
TORA WILISHO
MAYO
OLOBA
AGAZA
ADECHA
AMBE GIRARA
SHELA BORKOSHE
CHEFISA
MOTALA
BIGE WANCHE
BONGOTA
MERERU
HOBICHA BEDA
WANCHE RIDGE
UGALO WANCHE
ELO

Appendix B Borehole data at hydrothermal Manifestation area for Comparison

GTSite_ID	Name	Geothrm_Ty	Long	Lat	Elevation	Temp	PH
GTS0019	Biilate	Hot Spring	38.047	6.942	0	0.0	0.0
GTS0083	Dimtu Well	Well	38.134	6.928	1480	53.8	8.0
GTS0081	Bilbo Red boiling pool	Boiling pool	38.031	6.846	1386	95.4	0.0
GTS0080	Bilbo 1	Fumarole	38.033	6.846	1392	95.2	0.0
GTS0098	Tobacco 2	Thermal spring	38.094	6.818	1355	51.1	7.2
GTS0099	Tobacco 4	Thermal spring	38.094	6.817	1355	51.5	7.2
GTS0100	Tobacco 5	Thermal spring	38.092	6.814	1348	58.0	7.3
GTS0082	Tobacco 1	Bubbling pool	38.087	6.811	1346	63.4	7.3
GTS0096	Bolosho 2	Boiling pool	38.045	6.723	1240	91.5	7.7
GTS0095	Bolocho vasca	Bubbling pool	38.047	6.722	1255	65.8	7.3
GTS0084	Hako	Steam vent	37.898	6.696	1597	39.6	0.0
GTS0101	Metincho	Thermal spring	38.035	6.675	1219	50.3	7.8
GTS0020	Abaya	Hot Spring	37.891	6.646	0	0.0	0.0
GTS0086	North Abaya Spring	Thermal spring	37.919	6.646	1197	40.6	7.2
GTS0085	North Abaya	Bubbling pool	37.910	6.636	1200	62.6	6.6
GTS0102	Maze well	Well	37.869	6.626	1288	27.2	7.5
GTS0094	Boramitta	Bubbling pool	37.902	6.620	1195	56.4	6.6
GTS0092	North Abaya Fumarolic Field 7	Fumarole	37.901	6.615	1207	91.5	0.0
GTS0093	North Abaya Fumarolic Field 9	Fumarole	37.901	6.616	1207	94.0	0.0